

**PLANT EXTRACT MEDIATE SYNTHESIS OF MAGNETITE
(Fe₃O₄) NANOPARTICLES AND ITS ANTIBACTERIAL
APPLICATION**

*A dissertation submitted to the Department of Physics, Bangladesh University of Engineering
and Technology, Dhaka in partial fulfillment of the requirements
for the degree of Master of Science (M.Sc.) in Physics*

SUBMITTED

BY

Mohammad Moniruz Zaman

Roll No.: 0416142503

Session: April/ 2016



**DEPARTMENT OF PHYSICS
BANGLADESH UNIVERSITY OF ENGINEERING AND TECHNOLOGY
DHAKA – 1000, BANGLADESH**

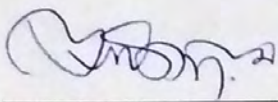
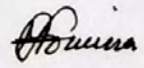
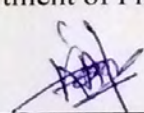
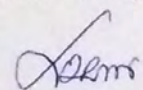
BANGLADESH UNIVERSITY OF ENGINEERING & TECHNOLOGY (BUET), DHAKA
DEPARTMENT OF PHYSICS



Certification of Thesis

The thesis titled “**PLANT EXTRACT MEDIATE SYNTHESIS OF MAGNETITE (Fe₃O₄) NANOPARTICLES AND ITS ANTIBACTERIAL APPLICATION**” submitted by Mohammad Moniruz Zaman, Roll No.0416142503F, Session: April/2016, has been accepted as satisfactory in partial fulfillment of the requirement for the degree of **Master of Science (M.Sc.)** in Physics on **04 September, 2018**

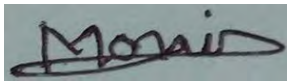
BOARD OF EXAMINERS

1. 
Dr. Mohammad Abu Sayem Karal (Supervisor) Chairman
Assistant Professor
Department of Physics, BUET, Dhaka
2. 
Dr. Md. Forhad Mina (Ex-Officio) Member
Professor & Head
Department of Physics, BUET, Dhaka
3. 
Dr. A. K. M. Akther Hossain Member
Professor
Department of Physics, BUET, Dhaka
4. 
Dr. Mohammad Khurshed Alam Member
Assistant Professor
Department of Physics, BUET, Dhaka
5. 
Dr. Mohammed Nazrul Islam Khan Member (External)
Principal Scientific Officer
Materials Science Division
Atomic Energy Center, Dhaka

CANDIDATE'S DECLARATION

It is hereby declared that this thesis or any part of it has not been submitted elsewhere for the award of any degree or diploma.

Signature of the candidate

A handwritten signature in dark ink, appearing to read 'Moniruz', is shown within a rectangular box. The signature is written in a cursive style with a prominent horizontal stroke at the bottom.

Mohammad Moniruz Zaman

Roll No.: 0416142503

Session: April, 2016

*Dedicated to
My Beloved Parents*

ACKNOWLEDGEMENTS

First of all, I humbly acknowledge my heartfelt gratitude to the almighty Allah, the most gracious, benevolent and merciful whose benediction has been guiding me to the light throughout the days and always.

I wish to express my deepest gratitude and sincere thanks to my honorable supervisor Dr. Mohammad Abu Sayem Karal, Assistant Professor, Department of Physics, Bangladesh University of Engineering and Technology (BUET), Dhaka-1000, Bangladesh for providing me an opportunity to work under his guidance. His kind attention, care and continuous encouragement have been a source of inspiration for me throughout the research.

I am thankful to Prof. Dr. Md. Forhad Mina, Head, Department of Physics, BUET for providing me necessary facilities to carry out this research work. I am also thankful to Prof. Dr. Md. Abu Hashan Bhuiyan, Prof. Dr. Md. Feroz Alam Khan, Prof. Dr. A. K. M. Akther Hossain, Prof. Dr. Md. Mostak Hossain, Prof. Dr. Afia Begum, Prof. Fahima Khanam, Prof. Dr. Md. Rafi Uddin, Prof. Dr. Nsreen Akter, Prof. Dr. Mohammed Abdul Basith, and other teachers in the Department of Physics, BUET for inspiration and constructive suggestions.

I am highly grateful to my respected teachers Dr. Md. Nazrul Islam Khan, Principal Scientific Officer, Materials Science Division, and Mr. A. K. M. Atique Ullah, Senior Scientific Officer, Chemistry Division, Atomic Energy Centre, Dhaka for their significant suggestions, intellectual help and continuous inspiration throughout my research work. I would like to extend my cordial thanks to Dr. Shamsad B. Quraishi, Chief Scientific Officer and Mr. Abu Rayhan Mohammad Tareq, Senior Scientific Officer, Chemistry Division, Atomic Energy Centre, Dhaka for their valuable help and continuous supports throughout my research period. I would like to give thanks to my friends Faysal, Tamanna, Tanjila, Tuli, Mahbub and lab staffs Mr. Zaidul, Mr. Md. Ayub Ali, Mrs. Ronia for their help and support.

I am also grateful to the authority of Department of Physics, BUET and Atomic Energy Centre, Dhaka for providing me the logistic supports for this thesis work. Sincere acknowledgement to the Bangladesh University Grants Commission and the

Committee for Advanced Studies & Research, BUET for granting the funds to carry out this research. Acknowledgements are due to the Shizuoka University and Hokkaido University, Japan for TEM image and antibacterial test, respectively.

At last, I would like to thank and acknowledge my parents whose unlimited love and blissful inspiration were always with me, to lead me to success in my life. I am also thankful to my siblings, family members and relatives for their constant inspiration, support, sacrifices and help to complete the thesis successfully.

Mohammad Moniruz Zaman

August, 2018

ABSTRACT

Magnetite (Fe_3O_4) nanoparticles (NPs) were prepared through green synthesis route using *Ipomoea aquatica* leaf extract that acted as an efficient stabilizer and capping agent of the NPs. These NPs has potential applications in various biomedical field such as bacterial killing, targeted drug delivery, magnetic hyperthermia, magnetic resonance imaging, etc. More than 75 components including carbohydrate, lipid and polysaccharides were present in the leaf extract which was confirmed by Gas Chromatography Mass Spectrometer (GC-MS) analysis. The X-ray Diffraction (XRD) analysis showed that the particles were crystalline with cubic inverse spinel structure and the crystallite size was found to be about 12.8 ± 0.8 nm. The surface morphology of the NPs was investigated by Field Emission Scanning Electron Microscopy (FESEM) which showed that NPs were spherical in shape with uniform size distribution. Elemental analysis of the NPs was carried out with Energy Dispersive X-ray (EDX) Spectroscopy and it indicated the elemental signature of the presence of iron, oxygen, carbon and nitrogen in the NPs. The particle size was determined from Transmission Electron Microscopy (TEM) image which was about 15 nm that supported the results of XRD and FESEM. The Fourier Transform Infrared Spectroscopy (FTIR) analysis showed that the capping agents of the NPs contained the functional groups alcohol, alkene, and alkyne. The thermal stability of Fe_3O_4 NPs were investigated using Differential Scanning Calorimetry (DSC) and Thermo Gravimetric Analysis (TGA). DSC showed two endothermic and one exothermic peaks. The percentage of weight loss was of about 10% as found from TGA. The NPs were superparamagnetic in nature with zero coercivity and zero remanance magnetization which was observed using a Vibrating Sample Magnetometer (VSM). The average particle size was determined by Dynamic Light Scattering (DLS) which showed that the particle size decreased with the decrease of precursor concentrations. This supported the results of XRD and VSM. The clear zone in the petri dish in agar diffusion test confirmed that the *Ipomoea aquatica* mediated Fe_3O_4 NPs had potential antibacterial activity for both gram negative and gram-positive bacteria. The pore formation in the bio-membrane of bacteria due to the interaction of NPs might be the possible mechanism to kill the bacteria.

CONTENTS	Page No.
ACKNOWLEDGEMENTS	iv
ABSTRACT	vi
LIST OF FIGURES	xii
LIST OF TABLES	xv
LIST OF ABBREVIATIONS	xvii

INDEX

CHAPTER 1

INTRODUCTION

1.1	Introduction	1
1.2	Rationale of the study	3
1.3	Objectives	5
	References	6

CHAPTER 2

LITERATURE REVIEW

2.1	Nanoscience and nanotechnology	10
2.2	Nanomaterials	11
2.2.1	Properties of nanomaterials	11
2.2.2	Classification of nanomaterials	12
2.3	Nanoparticles	13
2.4	Synthesis of NPs	14
2.4.1	Combustion method	15
2.4.2	Hydrothermal method	15
2.4.3	Gas phase method	15
2.4.4	Microwave synthesis	16
2.4.5	Sol-gel method	16
2.4.6	Co-precipitation method	16
2.4.7	Plant extract mediated bio-synthesis	17

2.5	Bio-medical applications of NPs	18
2.6	Metal oxide NPs	21
2.7	Magnetic NPs classifications	21
2.7.1	Iron oxides	22
2.7.1.1	Hematite	24
2.7.1.2	Maghemite	25
2.7.1.3	Magnetite	25
2.7.1.3.1	Crystal structure of magnetite	26
2.7.1.3.2	Physical properties of magnetite	26
2.7.1.3.3	Thermal properties of magnetite	27
2.7.1.3.4	Magnetic properties of magnetite	28
2.7.1.3.5	Surface chemistry of magnetite	31
2.8	Bacteria	31
2.8.1	Gram-positive bacteria	32
2.8.2	Gram-negative bacteria	33
2.9	Antibiotics resistance bacteria	34
2.10	Structure of lipid bilayer	35
2.10.1	Critical size of NPs for pore formation in lipid bilayer	37
	References	40

CHAPTER 3

EXPERIMENTAL TECHNIQUES

3.1	GC-MS analysis	47
3.1.1	Principle of GC-MS	48
3.2	XRD analysis	48
3.3	EDX analysis	52
3.4	FT-IR analysis	53

3.5	FESEM analysis	55
3.6	TEM analysis	58
3.7	DSC analysis	61
3.8	TGA analysis	64
3.9	VSM measurement	65
3.10	DLS measurement	66
3.11	Antibacterial application of NPs	67
3.11.1	Standardization of the method	68
3.11.1.1	Preparation	68
3.11.1.2	Incubation procedure	69
	References	71

CHAPTER 4

MATERIALS AND METHODS

4.1	Chemicals and reagents	74
4.2	Instruments	74
4.3	Synthesis of Fe ₃ O ₄ NPs	75
4.3.1	Leaf extracts preparation	76
4.3.2	GC-MS analysis of <i>Ipomoea aquatica</i> leaf extracts	79
4.3.3	Synthesis of Fe ₃ O ₄ NPs	80
4.3.4	Synthesis of Fe ₃ O ₄ NPs with the variation of NaOH concentration	83
4.3.5	Synthesis of Fe ₃ O ₄ NPs with the variation of FeCl ₃ and FeCl ₂ .4H ₂ O concentration	83
4.3.6	Disperse Fe ₃ O ₄ NPs in solvent	84
4.4	Characterizations of Fe ₃ O ₄ NPs	85
4.4.1	Elemental analysis of the leaf extracts	85
4.5.2	XRD analysis	85

4.4.3	EDX spectral analysis	85
4.4.4	FESEM analysis	85
4.4.5	FT-IR spectral analysis	86
4.4.6	TEM analysis	86
4.4.7	Thermal analysis	86
4.4.8	Magnetic property analysis	86
4.4.9	DLS analysis	86
4.5	Antibacterial application of Fe ₃ O ₄ NPs	86
	References	88

CHAPTER 5

RESULTS AND DISCUSSION

5.1	GC-MS spectra analysis of <i>Ipomoea aquatica</i> leaf extracts	90
5.2	XRD pattern analysis of Fe ₃ O ₄ NPs	93
5.2.1	XRD patterns analysis for the variation of NaOH concentration	95
5.2.2	XRD patterns analysis for the variation of FeCl ₃ and FeCl ₂ .4H ₂ O concentration	97
5.3	EDX spectrum analysis	98
5.4	FT-IR analysis of Fe ₃ O ₄ NPs	100
5.5	FESEM analysis	101
5.6	TEM analysis	102
5.7	DSC and TGA analysis of Fe ₃ O ₄ NPs	102
5.8	Magnetization analysis	103
5.8.1	Magnetization analysis for the variation of NaOH concentration	104
5.8.2	Magnetization analysis for the variation of FeCl ₃ and FeCl ₂ .4H ₂ O concentration	106
5.9	Particle size distribution measurement of Fe ₃ O ₄ NPs	108

5.10	Correlation among crystallite size, average particle size and saturation magnetization of the NPs synthesized for different concentrations of NaOH	111
5.11	Correlation among crystallite size, average particle size and saturation magnetization of the NPs synthesized for different concentrations of iron salt	113
5.12	Antibacterial application of Fe ₃ O ₄ NPs	114
	References	117

CHAPTER 6

CONCLUSIONS

6.1	Conclusions	119
6.2	Recommendations	121

LIST OF FIGURES

Fig. 2.1	Classification of nanomaterials according to their dimension	13
Fig. 2.2	Schematic of bottom up and top down approaches	14
Fig. 2.3	Plants used for Fe ₃ O ₄ NPs synthesis	18
Fig. 2.4	Fe ₃ O ₄ NPs powder	25
Fig. 2.5	Inverse spinel crystalline structure of magnetite	26
Fig. 2.6	Increasing effective surface area with decreasing particle size	27
Fig. 2.7	Generic ferrimagnetic hysteresis loop	28
Fig. 2.8	Absence of hysteresis loop implies superparamagnetism	29
Fig. 2.9	Spin arrangements in Fe ₃ O ₄ and the double exchange interaction with inter-ion electron transfer	30
Fig. 2.10	Gram positive bacteria	32
Fig. 2.11	Gram negative bacteria	33
Fig. 2.12	Schematic diagram of lipid bilayer	36
Fig. 2.13	Pore formation mechanism of NPs in lipid bilayer	39
Fig. 3.1	GC-MS setup	47
Fig. 3.2	Schematic diagram of GC-MS	48
Fig. 3.3	Electromagnetic spectrum	49
Fig. 3.4	A PHILIPS PW 3040 X'Pert Pro X-ray diffractometer	50
Fig. 3.5	Schematic diagram of X-ray	51
Fig. 3.6	Bragg's diffraction pattern	52
Fig. 3.7	Schematic illustration of an FT-IR system	54
Fig. 3.8	A Photo of Jasco FT-IR 6300 machine	55
Fig. 3.9	Schematic diagram of FESEM	56
Fig. 3.10	A Photo of FESEM JSM-7600F	58
Fig. 3.11	Schematic representation of TEM	59
Fig. 3.12	TEM image of Fe ₃ O ₄ NPs	60
Fig. 3.13	Schematic diagram of DSC	61
Fig. 3.14	DSC & TGA analyzer (TA instrument, SDT Q-600)	62
Fig. 3.15	Heat flow as a function of DSC curve	63
Fig. 3.16	Weight loss as a function of temperature	64
Fig. 3.17	VSM setup	65

Fig. 3.19	DLS setup	66
Fig. 3.20	Agar disk diffusion method	68
Fig. 3.21	A closed-up look at the result of agar diffusion test	69
Fig. 3.22	Kirby-Bauer testing: White wafers containing antibiotics shown on plate of bacteria. Circles of poor bacterial growth surround some wafers, indicating susceptibility to the antibiotic	70
Fig. 4.1	Basic equipments used for synthesis of Fe ₃ O ₄ NPs (a) Mortar (b) Centrifuge machine (c) Magnetic stirrer (d) Digital balance (e) Electric oven (f) Bath sonicator	75
Fig. 4.2	Schematic diagram demonstrating the interaction between Fe ₃ O ₄ NPs charged groups which are capped by <i>Ipomoea aquatica</i>	76
Fig. 4.3	<i>Ipomoea aquatica</i> (a) healthy green leaves and (b) finest leaves paste	76
Fig. 4.4	Preparation of <i>Ipomoea aquatica</i> leaf extracts	77
Fig. 4.5	<i>Ipomoea aquatica</i> leaf extracts	77
Fig. 4.6	<i>Ipomoea aquatica</i> leaf extracts preparation	78
Fig. 4.7	Instrumental setup of essential oil collection from <i>Ipomoea aquatica</i> leaf extracts	79
Fig. 4.8	Solution of (a) FeCl ₂ .H ₂ O and (b) FeCl ₃	80
Fig. 4.9	Solution after addition of <i>Ipomoea aquatica</i> leaf extracts	80
Fig. 4.10	Solution color turned black after addition of NaOH	81
Fig. 4.11	Magnetic separation of Fe ₃ O ₄ NPs (a) before applying magnetic field (b) after applying magnetic field	81
Fig. 4.12	Fe ₃ O ₄ NPs synthesis	82
Fig. 4.13	Disperse solution of Fe ₃ O ₄ NPs in DDW	84
Fig. 5.1	GC-MS spectra of <i>Ipomoea acuatica</i> leaf extracts	90
Fig. 5.2	XRD pattern of Fe ₃ O ₄ NPs	93
Fig. 5.3	XRD patterns of Fe ₃ O ₄ NPs synthesized with different concentration of NaOH	95
Fig. 5.4	Crystallite size vs concentration of NaOH	96
Fig. 5.5	XRD patterns of Fe ₃ O ₄ NPs synthesized with different concentration of FeCl ₃ and FeCl ₂ .4H ₂ O	97
Fig. 5.6	Crystallite size vs concentration of FeCl ₃	98
Fig. 5.7	EDX Spectrum of Fe ₃ O ₄ NPs with <i>Ipomoea acuatica</i> leaf extracts	99

Fig. 5.8	FT-IR spectrum of Fe ₃ O ₄ NPs	100
Fig. 5.9	FESEM image of surface morphology of Fe ₃ O ₄ NPs	101
Fig. 5.10	TEM image of Fe ₃ O ₄ NPs	102
Fig. 5.11	DSC/TGA as a function of temperature of Fe ₃ O ₄ NPs	103
Fig. 5.12	Magnetization curve of Fe ₃ O ₄ NPs as a function of applied field	104
Fig. 5.13	Magnetization curve of Fe ₃ O ₄ NPs synthesized using different concentrations of NaOH	105
Fig. 5.14	Saturation magnetization vs concentration of NaOH	106
Fig. 5.15	Magnetization curve of Fe ₃ O ₄ NPs as a function of applied field synthesized using different concentrations of FeCl ₃ and FeCl ₂ .4H ₂ O	106
Fig. 5.16	Saturation magnetization vs concentration of FeCl ₃	107
Fig. 5.17	Size distribution of NPs for different concentration of NaOH (a) 1.0 (b) 0.5 (c) 0.1 (d) 0.05 M	108
Fig. 5.18	Average particle size vs concentration of NaOH	109
Fig. 5.19	Size distribution of Fe ₃ O ₄ NPs synthesized with different concentrations of FeCl ₃ and FeCl ₂ .4H ₂ O. FeCl ₂ .4H ₂ O (a) 1.00 (b) 0.20 (c) 0.10 (d) 0.02 (e) 0.01 M	110
Fig. 5.20	Average particle size vs concentration of FeCl ₃	111
Fig. 5.21	NPs synthesized with different concentrations of NaOH (a) Crystallite size vs concentration (b) particle size vs concentration and (c) saturation magnetization vs concentrations	112
Fig. 5.22	NPs synthesized with different concentrations of FeCl ₃ (a) Crystallite size vs concentration (b) particles size vs concentration and (c) saturation magnetization vs concentration	113
Fig. 5.23	Antibacterial activity of (1) DI water, (2) ampicilin and (3) Fe ₃ O ₄ NPs against gram-negative E. coli (a) and gram-positive B. subtilis (b) pathogenic bacteria	114
Fig. 5.24	Bacterial membrane rupturing mechanism of Fe ₃ O ₄ NPs	115
Fig. 5.25:	Peptidoglycan (cell wall) of gram-positive and gram-negative bacteria	116

LIST OF TABLES

Table 2.1	Classification of nanomaterials based on dimensionality	12
Table 2.2	Biosynthesis of Fe ₃ O ₄ NPs from biological sources	17
Table 2.3	Saturation magnetization and curie temperature for several transition metals and metal oxides	22
Table 2.4	Iron oxyhydroxide and iron oxide species	23
Table 2.5	Physical properties of magnetite and maghemite	24
Table 2.6	Estimated maximum single-domain size for spherical particles	31
Table 2.7	List of antibiotics resistance bacteria	35
Table 5.1	Compositions of leaf extract according to their functional group	91
Table 5.2	Structural parameters of Fe ₃ O ₄ NPs obtained from XRD analysis	95
Table 5.3	Structural parameters of Fe ₃ O ₄ NPs synthesized with different concentrations of NaOH	96
Table 5.4	Structural parameters of Fe ₃ O ₄ NPs synthesized with different concentrations of FeCl ₃ and FeCl ₂ .4H ₂ O	98
Table 5.5	Elemental analysis of Fe ₃ O ₄ NPs from EDX	99
Table 5.6	Functional group, peak position and attribution in FT-IR of Fe ₃ O ₄ NPs	101
Table 5.7	Saturation magnetization of Fe ₃ O ₄ NPs synthesized with different concentrations of NaOH	105
Table 5.8	Saturation magnetization of Fe ₃ O ₄ NPs synthesized with different concentrations of FeCl ₃ and FeCl ₂ .4H ₂ O	107
Table 5.9	Average particle size of Fe ₃ O ₄ NPs synthesized with different concentrations of NaOH	109
Table 5.10	Average particle size of Fe ₃ O ₄ NPs synthesized with different concentrations of FeCl ₃ and FeCl ₂ .4H ₂ O	111

LIST OF ABBREVIATIONS

SYMBOL	ABBREVIATION
1D	One Dimensional
2D	Two Dimensional
3D	Three Dimensional
<i>B. subtilis</i>	<i>Bacillus subtilis</i>
D	Crystallite size
d	Average particle size
DW	Distill Water
DDW	Double Distill Water
DEG	Diethylene Glycol
DI	De-ionized
DLS	Dynamic Light Scattering
Ds	Single Domain Diameter
DSC	Differential Scanning Calorimeter
<i>E. coli</i>	<i>Escherichia coli</i>
EDX	Energy Dispersive X-ray
Fe ₃ O ₄	Magnetite
FESEM	Field Emission Scanning Electron Microscope
FT-IR	Fourier Transform Infrared Spectroscopy
GC-MS	Gas Chromatography Mass Spectroscopy
M _s	Saturation magnetization
NPs	Nanoparticles
ROS	Reactive Oxygen Species
T _c	Curie Temperature
TEM	Transmission Electron Microscopy
TGA	Thermo Gravimetric Analysis
XRD	X-ray Diffraction
δ	Dislocation density
ε	Microstrain

CHAPTER 1

INTRODUCTION

1.1 Introduction

At present, nanoscience and nanotechnology is considered as a new turning point in the field of science and technology. Nanoparticles (NPs) become the core material in this field due to their unique physical, chemical, mechanical, electrical, optical, catalytic and magnetic properties compared to their large counterparts [1]. In general, these properties depend upon the size and shape of the particles [2, 3]. NPs have wide range of applications in various fields like medicine, pharmaceuticals, biotechnology, information technology, energy, agriculture etc.

Being the most current transition metal in the Earth's crust, iron stands as the backbone of current infrastructure [4]. Magnetic iron oxide NPs have attracted much attention due to their low toxicity, bio-compatibility, superparamagnetic properties, large surface area and volume ratio as well as good reactive surface [5]. The extreme reactivity of iron makes it difficult to study and problematic for applications. However, strong magnetic and catalytic properties have diverted the attention toward iron's potential [6]. Synthesis methods, crystallization, size, shape, and quality of the iron oxide NPs greatly affect these behaviors. The shapes of nanomaterials also exert tremendous impact on their properties, more importantly in catalysis [7]. Shape change shows crystal facets, and the atomic arrangements in each facet have reflective effects on its properties [8]. The development of protocols for desired morphology, size, and shape is under consideration [9].

Among the 16 identified iron oxide compounds, iron (III) oxide is found in the form of rust in nature. Iron oxides are prevalent, inexpensive, and the most widely used bio-compatible material which play an imperative role in many biological and geological processes [10]. The three most common forms of iron oxides in nature are magnetite (Fe_3O_4), maghemite ($\gamma\text{-Fe}_2\text{O}_3$), and hematite ($\alpha\text{-Fe}_2\text{O}_3$) which are also very important in the field of scientific research [11]. Fe_3O_4 is a common magnetic iron

oxide that has a cubic inverse spinel structure with oxygen forming FCC closed packing and Fe cations occupying interstitial tetrahedral sites and octahedral sites. The electrons can hop between Fe^{2+} and Fe^{3+} ions in the octahedral sites at room temperature rendering magnetite an important class of half-metallic materials [12].

There are several methods for the synthesis of Fe_3O_4 NPs, which include sol-gel process [13], co-precipitation [14], sono-chemical method [15], hydrothermal techniques [16], non-aqueous synthesis [17], ultrasound irradiation [18], micro-emulsion method [19] etc. All these physical and chemical methods require high pressures and temperatures, even involving harmful chemicals. In contrast, biogenic synthesis involves the synthesis of NPs using plants and microbes or their extracts. Microbial synthesis is time consuming and somewhat risky method, since it involves the maintenance of microbial cultures under sophisticated, aseptic laboratory conditions. Green synthesis using plants and plant extracts is currently under exploitation. It is eco-friendly, safe, non-toxic and cost-effective approach having high rate of reaction [20]. Developing a facile and green method for synthesizing superparamagnetic Fe_3O_4 is of importance and still a challenge for materials scientists. Over the past two decades, there have been increased emphases on the topic of green chemistry and chemical processes. Utilization of nontoxic chemicals, environmentally benign solvents, and renewable materials are some of the key issues that merit important consideration in a green synthetic strategy. The *Ipomoea acuatica* leaves possesses biomolecules such as carbohydrates, proteins and lipids [21], which could be used as reducing agent to react with ferric and ferrous ions as scaffolds to direct the formation of Fe_3O_4 NPs in solution that have been extensively explored for possible medical applications. NPs provide a particularly useful platform and demonstrate unique properties with potentially wide-ranging therapeutic applications [22].

Antibiotic resistant bacterial strains with different mechanisms are found continually and thus new drugs are required [23]. Therefore, the finding of new antimicrobial agents with novel mechanisms of action is essential and extensively pursued in antibacterial drug discovery [24]. Microbial resistance to antibiotics is a world-wide problem in humans and animals. It is generally accepted that the main risk factor for the increase in the antibiotic resistance is an extensive use of antibiotics. This lead to the emergence and dissemination of resistant bacteria and resistance genes in animals

and humans [25]. The antibiotic resistance of pathogens can be a result of several different factors. Resistance among bacteria is continuously increasing. Nanotechnology is expected to open a new avenue to fight and prevent diseases using atomic scale tailoring of materials. Recently, it has been demonstrated that metal oxide NPs exhibit excellent biocidal and biostatic actions against gram-positive and gram-negative bacteria [26].

1.2 Motivation and Objective of the study

The unusual physicochemical properties of engineered nanomaterials are attributable to their small size (surface area and size distribution), chemical composition (purity, crystallinity, electronic properties etc.), surface structure (surface reactivity, surface groups, inorganic or organic coatings etc.), solubility, shape and aggregation. Studies have shown that the size, morphology, stability and properties (chemical and physical) of the metal NPs are strongly influenced by the conditions of experiment, the kinetics of interaction of metal ions with reducing agents and the adsorption processes of stabilizing agent with metal NPs [27]. Due to the exclusive properties like superparamagnetic, reactive surface, bio-degradability, bio-compatibility, non-toxicity, high saturation magnetization and low Curie temperature; Fe_3O_4 has wide variety of applications such as targeted drug delivery, magnetic resonance imaging (MRI), hyperthermia treatment, medical diagnosis and therapy and magnetic bio-detection. Therefore, exponential growth in research focuses on synthesis, properties and applications of Fe_3O_4 NPs that have been accomplished in recent years.

Synthesis of NPs with the required quality and desired properties is one of the important issues in present green nanotechnology. The development of green processes for the synthesis of NPs is evolving into an important branch of nanotechnology. The bio-synthesis of NPs involves three main steps, including: (a) selection of solvent medium, (b) selection of environmentally benign reducing agent, and (c) selection of nontoxic substances for the NPs synthesis [28]. As a consequence, in order to meet the exponentially growing technological demand, it is desirable to study the bio-synthesis route for the synthesis of various NPs and presently available literature reveals that the metal oxide NPs synthesis using plants, microorganisms and algae as a source has been unexplored and underexploited. Several scientists have already synthesized the green route of Fe_3O_4 NPs using *Tridax procumbens* [29],

Syzygium cumini seed extract [30], using microorganisms [31], *Datura inoxia* peel extract [32], *Ocimum sanctum* leaf aqueous extract [33] etc.

Hence developing of a bio-synthetic and environmental friendly approach has added much importance because of its eco-friendly products, biocompatibility and economic viability in the long run and also to avoid adverse effects during their applications especially in biomedical field. The microbial enzyme or the plant phytochemicals with antioxidant or reducing properties are usually responsible for the preparation of Fe₃O₄ NPs. The eco-friendly and green chemistry perspective for the nanoparticle synthesis are the choice of the solvent medium, reducing agent and non-toxic material respectively for the stabilization of NPs [34]. Among the various bio-synthetic approaches, the use of plant extracts has advantages such as easily available, safe to handle and possess a broad viability of metabolites.

In continuation of the efforts for synthesizing of stable and biocompatible Fe₃O₄ NPs here we report a facile, less labor and biodegradable synthesis using the leaf extract of *Ipomoea aquatica* which has been chosen due to the availability in our country and subcontinent.

1.3 Outline of the thesis

The overall goal of the thesis work is to synthesis of Fe₃O₄ NPs via green synthesis route using *Ipomoea aquatica* leaf extract as a capping agent to study the antibacterial activity for both gram-positive and gram-negative bacteria using agar diffusion method.

In chapter 1, the motivation and outline of the thesis are given why and how the *Ipomoea aquatica* leaf extract mediated Fe₃O₄ NPs have been selected for antibacterial study.

In chapter 2, Literature review of the present state of the art of Fe₃O₄ nanoparticles synthesis, green synthesis and different types of synthesis process have been explain and included in details.

In chapter 3, Experimental setup used for synthesis, characterizations and applications have been represented. Several tools such as Gas Chromatography Mass Spectrometer (GC-MS), X-ray Diffractometer (XRD), Field Emission Scanning Electron Microscopy (FESEM) coupled with an Energy Dispersive X-ray Spectroscopy (EDX), Transmission Electron Microscopy (TEM), Dynamic Light Scattering (DLS), Vibrating Sample Magnetometer (VSM), Fourier Transform Infrared Spectroscopy (FTIR), Differential Scanning Calorimetry (DSC) and Thermo Gravimetric Analysis (TGA), Agar diffusion process for bacterial activity with both gram-positive and gram-negative bacteria, etc have been explained briefly.

In chapter 4, *Ipomoea aquatica* leaf extract preparation, Green synthesis of Fe₃O₄ NPs mediated by *Ipomoea aquatica* leaf extract, etc have been described in details.

In chapter 5, Experimental results is presented here. The NPs shows antibacterial activity results in compared with the control results.

In chapter 6, *Ipomoea aquatica* leaf extract mediated Fe₃O₄ NPs of size about 15 nm synthesized successfully which has potential activity to kill bacteria.

References

- [1] Monaliben, S., Derek, F., Shashi, S., Suraj, K. T., G errard E. J. P., "Green synthesis of metallic nanoparticles via biological entities," *Mater. Sci.*, vol. 8, pp. 7278–7308, 2015.
- [2] Gregory, G., Sergio, M., Francis, L. D., "Nanomaterial properties: size and shape dependencies," *J. Nanomater.*, vol. 2012, pp. 2, 2012.
- [3] Francois, F., Ludovic, E., Gerard, B., "Optical properties of nanostructured materials: a review," *J. Nanophotonics*, vol. 5, pp. 1934-2608, 2011.
- [4] Attarad, A., Hira, Z., Muhammad, Z., Ihsan-ul H., Abdul R. P., Joham S. A., Altaf H., "Synthesis, characterization, applications, and challenges of iron oxide nanoparticles," *Nanotechnol. Sci. Appl.*, vol. 9, pp. 49-57, 2016.
- [5] Jiri, K., Yazan, H., Lukas, R., Zbynek, H., Mirko, C., Vojtech, A., Ondrej, Z., "Magnetic nanoparticles: From design and synthesis to real world applications," *J. Nanomater*, vol. 7, pp. 243-273, 2017.
- [6] Ahmed, M. A. D., Shimaa M. A. F., "Development and functionalization of magnetic nanoparticles as powerful and green catalysts for organic synthesis," *Beni-Seuf Univ. J. Appl. Sci.*, vol. 17, pp. 192-224, 2017.
- [7] Ibrahim, K., Khalid, S., Idrees, K., "Nanoparticles: Properties, applications and toxicities," *ARAB. J. CHEM.*, vol. 16, pp. 262-271, 2017.
- [8] Hyeong, C. J., Ellen, D. W., "Steps on surfaces: experiment and theory," *Surf. Sci. Rep.*, vol. 34, pp. 171-294, 1999.
- [9] Wei W., Zhaohui W., Taekyung, Y., Changzhong, J., Woo, S. K., "Recent progress on magnetic iron oxide nanoparticles: synthesis, surface functional strategies and biomedical applications," *Sci. Technol. Adv. Mater.*, vol. 16, pp. 43-87, 2015.
- [10] Pankhurst, Q. A., Connolly, J., Jones, S. K., Dobson, J., "Applications of magnetic nanoparticles in biomedicine," *J. Phys. D: Appl. Phys.*, vol. 36, pp. 167-181, 2003.
- [11] Lodhia, J., Mandarano, G., Ferris, N. J., Eu, P., Cowell, S. F., "Development and use of iron oxide nanoparticles (Part 1):," *Biomed. Imaging Interv. J.*, vol. 2, pp. 6-17, 2010.

- [12] Andrade, A. L., Souza, D. M., Pereira, M. C., Fabris, J. D., Domingues, R. Z., "Synthesis and characterization of magnetic nanoparticles coated with silica through a sol-gel approach," *Cerâmica*, vol. 55, pp. 420-424, 2009.
- [13] Ruohong, S., Paul, C., "Synthesis of metal oxide nanostructures by direct Sol-Gel chemistry in supercritical fluids," *Chem. Rev.*, vol. 112, pp. 3057-3082, 2012.
- [14] Khalil, M.I., "Co-precipitation in aqueous solution synthesis of magnetite nanoparticles using iron(III) salts as precursors," *ARAB. J. CHEM.*, vol. 8, pp. 279-284, 2015.
- [15] Amir, H. R., Mohammad, R. V., Ali S., Zohreh, R. , "Synthesis of iron oxide nanoparticles via sonochemical method and their characterization," *Particuology*, vol. 9, pp. 95-99, 2011.
- [16] Jianlin, L., Qingliu, W., Ji, W., "Synthesis of nanoparticles via solvothermal and hydrothermal methods," *Handbook of Nanoparticles*, vol. 17, pp. 295-328, 2015.
- [17] Markus, N., Georg, G., Jelena, B., Julien, P., Jianhua, B., Nicola, P., "Nonaqueous synthesis of metal oxide nanoparticles: Review and indium oxide as case study for the dependence of particle morphology on precursors and solvents," *J. Sol-Gel Sci. Techn.*, vol. 40, pp. 259-266, 2006.
- [18] Garciaa, M. I. D., Orezza, V. M., Jankulovska, M., Anandan, S., Bonetea, P., Gomez, R., Villarreal, T. L., "Effects of ultrasound irradiation on the synthesis of metal oxide nanostructures," *Phys. Procedia*, vol. 63, pp. 85 - 90, 2015.
- [19] Maqsood, A. M., Mohammad, Y. W., Mohd, A. H., "Microemulsion method: A novel route to synthesize organic and inorganic nanomaterials," *ARAB. J. CHEM.*, vol. 5, pp. 397-417, 2012.
- [20] Pratyusha, B., Debjani, N., "Plants and eco-friendly nanomaterials- A review," *Conference Paper*, pp. ISBN 978, 2015.
- [21] Igwenyi, I. O., Offor, C. E., Ajah, D. A., Nwankwo, O. C., Ukaomah, J. I., Aja, P. M., "Chemical composition of *Ipomea aquatica* (Green kangkong)," *Int. J. Pharma Bio Sci.*, vol. 2, pp. 593-598, 2011.
- [22] Arun, G. I., Chaudhari, A. N., "Biogenic synthesis of nanoparticles and potential applications: An eco- friendly approach," *J Nanomed Nanotechol*, vol. 4, pp.

- 165-172, 2013.
- [23] Julian, D., and Dorothy, D., "Origins and evolution of antibiotic resistance," *Microbiol Mol Biol Rev*, vol. 74, pp. 417–433, 2010.
- [24] Lynn L. S., "Challenges of antibacterial discovery," *Microbiol Mol Biol Rev*, vol. 24, pp. 71–109, 2011.
- [25] Mølbak, K., "Spread of resistant bacteria and resistance genes from animals to humans –the public health consequences," *J. Vet. Med.*, vol. 51, pp. 364–369, 2004.
- [26] Federica, P., Mauro, P., Alessandro, S., Luigi, A., "Metal-based antibacterial substrates for biomedical applications," *Biomacromolecules*, vol. 16, pp. 1873–1885, 2015.
- [27] Makarov, V. V., Love, A. J., Sinitsyna, O. V., Makarova, S. S., Yaminsky, I. V., Taliansky, M. E., Kalinina, N. O., "Green nanotechnologies: synthesis of metal nanoparticles using plants," *Acta Naturae*, vol. 6, pp. 35–44, 2014.
- [28] Sadia, S., Arifa, T., Yongsheng, C., "Green synthesis of iron nanoparticles and their environmental applications and implications," *Nanomaterials*, vol. 6, pp. 209-235, 2016.
- [29] Senthil, M., Ramesh, C., "Biogenic synthesis of Fe₃O₄ nanoparticles using tridax procumbens leaf extract and its antibacterial activity on pseudomonas aeruginosa," *Dig J Nanomater Biostruct.*, vol. 7, pp. 1655-1660, 2012.
- [30] Sada, V., Natesh, K., B., Prasad, C.H., Venkateswarlu, P., Jyothi, N.V.V., "Bio-inspired green synthesis of Fe₃O₄ spherical magnetic nanoparticles using Syzygium cumini seed extract," *PHYSICA B. Journal*, vol. 449, pp. 67-71, 2014.
- [31] Abhilash, Revati, K., Pandey B. D., "Microbial synthesis of iron-based nanomaterials—A review," *Bull. Mater. Sci.*, vol. 34, pp. 191–198, 2011.
- [32] Amlan, K. D., Avinash, M., Ruchi, V., "Datura inoxia leaf extract mediated one step green synthesis and characterization of magnetite (Fe₃O₄) nanoparticles," *Pharm Nanotechnol.*, vol. 43, pp. 247-250, 2014.
- [33] Kanagasubbulakshmi, S., Kadirvelu, K., "Green synthesis of iron oxide nanoparticles using Lagenaria siceraria and evaluation of its antimicrobial activity," *Def. Life SCI. J.*, vol. 2, pp. 422-427, 2017.

- [34] Monaliben, S., Derek, ., Shashi, S., Suraj, K. T., G errard, E. J. P., "Green synthesis of metallic nanoparticles via biological entities," *Mater. Sci.*, vol. 8, pp. 7278–7308, 2015.

CHAPTER 2

LITERATURE REVIEW

2.1 Nanoscience and nanotechnology

The word “Nano” is originated from a Greek word whose meaning is extremely small or dwarfs [1]. The basic concepts behind nanoscience and nanotechnology was reported with a talk entitled “There’s a Plenty of Room at the Bottom” by the Physicist Richard Feynman at the California Institute of Technology on December 29, 1959 [2]. The term “Nanotechnology” was later coined by Professor Norio Taniguchi using Feynman’s explorations of ultra-precision machining. A brief and general definition of nanotechnology by the US National Science and Technology Council [3] states: “The essence of nanotechnology has the capability to work at the molecular level such as atom by atom for the creation of large structures with essentially innovative molecular organization. The aim is to exploit these properties by gaining control of structures and devices at atomic, molecular, and supra molecular levels and to become skilled at well-organized manufacture and use these devices.” The United States National Science Foundation [4] defines nanoscience or nanotechnology is the study which deals with materials and systems deserving the following two key properties:

- The dimension must be at least one dimension from 1-100 nm.
- According to the building block property, larger structures form by the combination of smaller one. According to the microbiological study, the nanoscience leads to the sizes of different types of bioparticles which deals with bacteria, viruses, enzymes etc. fall within the nanometer range.
- The process can be designed with various methodologies which show elementary control over the physical and chemical properties of structures that can be measure by the molecular-scale.

Nanotechnology has the capability at atomic precision which is useful for making of materials, various instruments and systems [4, 5]. Nanotechnology can also be defined as the study and investigation about the synthesis, characterization, exploration and

application of nano sized materials which is of 1-100 nm in size and will be valuable and functional for the development of science. A recent advance in the emerging field of nanotechnology has the capability for the preparation of the highly ordered nanoparticulates of various different size and shape which led to the development of the modern technology [6]. The prefix nano means a factor of one billionth (10^{-9}) and can be applied, e.g., to time (nanosecond), volume (nanoliter) weight (nanogram) or length (nanometer or nm).

2.2 Nanomaterials

Nanomaterials made of metals, semiconductors, or oxides are of particular interest for their mechanical, electrical, magnetic, optical, chemical and other properties [7]. Nanomaterials are effectively a bridge between bulk materials and atomic or molecular structures. A bulk material should have constant physical properties regardless of its size, but at the nano-scale this is often not the case. For example, the bending of bulk copper (wire, ribbon etc.) occurs with movement of copper atoms/clusters at about the 50 nm scale. Copper NPs smaller than 50 nm are considered super hard materials that do not exhibit the same malleability and ductility as bulk copper [8]. A material such as gold, which is chemically inert at normal scales, can serve as a potent chemical catalyst at nanoscales. Much of the fascination with nanotechnology stems from these quantum and surface phenomena that matter exhibits at the nanoscale.

2.2.1 Properties of nanomaterials

The unique properties of various types of intentionally produced nanomaterials give them novel electrical, catalytic, magnetic, mechanical, thermal or imaging features that are highly desirable for applications in commercial, medical, military and environmental sectors [9]. The material properties of nanostructures are different from the bulk due to the high surface area over volume ratio and possible appearance of quantum effects at the nanoscale. As a particle decreases in size, a greater proportion of atoms are found at the surface compared to those inside [10].

For example, a particle of size 30 nm has 5% of its atoms on its surface, at 10 nm 15% of its atoms, and at 3 nm 50% of its atoms. Thus, NPs have a much greater surface area per unit mass compared with larger particles. As growth and catalytic

chemical reactions occur at surfaces, this means that a given mass of material in nanoparticulate form will be much more reactive than the same mass of material made up of larger particles. In tandem with surface-area effects, quantum effects can begin to dominate the properties of matter as size is reduced to the nanoscale. These can affect the optical, electrical and magnetic behavior of materials, particularly as the structure or particle size approaches the smaller end of the nanoscale. The large surface area to volume ratio results in a substantial proportion of atoms having different magnetic coupling with neighboring atoms leading to differing magnetic properties. For instance, bulk gold and platinum are non-magnetic but at the nano-size they act as magnetic particles. Gold NPs become ferromagnetic when they are capped with the appropriate molecules. Semiconductors and many metals show large changes in optical properties such as color, as a function of particle size [11]. Colloidal suspensions of gold NPs have a deep red color which becomes progressively more yellow as the particle size increases.

2.2.2 Classification of nanomaterials

Generally, nanomaterials are referred as the infrastructure or building blocks element for nanotechnology. The “Building blocks” for nanomaterials consist of carbon-based components and organics, semiconductors, metals and metal oxides [12]. Nanomaterials with structural features at the nanoscale can be found in the form of clusters, thin films, multilayer and nanocrystalline materials which are often expressed by the dimensionality of 0, 1, 2 and 3 as shown in Table 2.1. The materials include metals, amorphous and crystalline alloys, semiconductors, oxides, nitride and carbide ceramics in the form of clusters, thin films, multilayer and the bulk nanocrystalline materials. Classification of various nanomaterials is shown in Fig. 2.1.

Table 2.1: Classification of nanomaterials based on dimensionality

Dimension	Example of nanomaterials
0D	Nanoparticles, colloids, nanodots, nanoclusters
1D	Nanowires, nanotubes, nanobelts, nanorods
2D	Quantum wells, super lattice, membranes
3D	Nanocomposites, cellular materials, nanocrystal array, block polymers

The familiar nanomaterial ‘carbon black’ was used in industrial production over a century ago. The other early nanomaterials are fumed silica, a form of silicon dioxide (SiO_2), Fe_3O_4 and zinc oxide (ZnO). Nanomaterials can have different properties at nanoscale which is also established by the quantum effects. Among all nanomaterials, some are having better conductivity towards heat and electricity, different magnetic properties, light reflection and also change colors according to their size which is also changed. These properties are a little bit different from the bulk materials. Nanomaterials also have larger surface areas than similar volumes of larger-scale

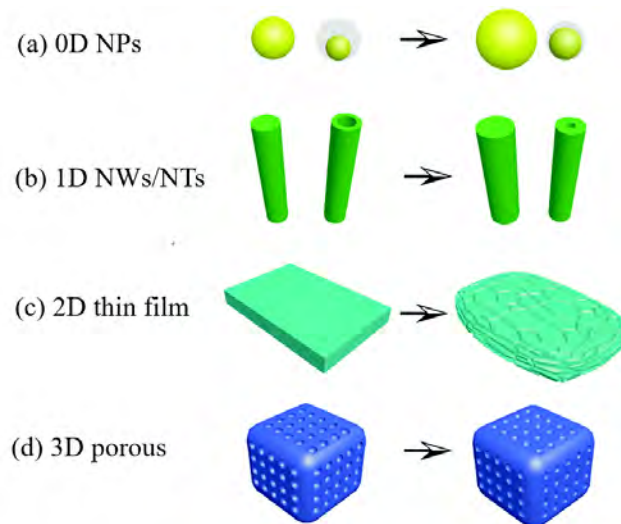


Fig. 2.1: Classification of nanomaterials according to their dimension

materials which signify the meaning of more surfaces is available for interactions with other materials around them. Nanomaterials are being controlled to nano crystalline size which is less than 100 nm which can show atom-like behaviors. This results from its higher surface energy due to their large surface area and wider band gap between valence and conduction band. It occurs when they are divided to near atomic size [8, 12]. Nanomaterials are also referred as “a wonder of modern medicine”. It signifies the importance of antibiotics which kill at least six different disease-causing organisms whether the nanomaterials can kill at least 650 cells [13]. Nanomaterials are being enthusiastically researched for specific function like microbial growth inhibition, carriers of antibiotics and also act as killing agents [14].

2.3 Nanoparticles

NPs are particles between 1 and 100 nm in size with a surrounding interfacial layer. The interfacial layer is an integral part of nanoscale matter, fundamentally affecting all of its properties. In nanotechnology, a particle is defined as a small object that behaves as a whole unit with respect to its transport and properties. There are two different types of NPs, inorganic NPs and organic NPs. The inorganic NPs include metal and metal oxides, which are potent antibacterial agents. Metal oxide NPs such as silver (Ag), iron oxide (Fe_3O_4), titanium oxide (TiO_2), copper oxide (CuO), and zinc oxide (ZnO) are certain examples of inorganic NPs. Organic NPs include poly- ϵ -lysine, quaternary ammonium compounds, cationic quaternary polyelectrolytes, N-halamine compounds, and chitosan. Organic NPs are generally less stable at high temperatures. Due this reason, inorganic NPs are more preferred as antimicrobial polymers [15].

2.4 Synthesis of NPs

Fabrication of nanomaterials with strict control over size, shape, and crystalline structure has become very important for the applications of nanotechnology in numerous fields including catalysis, medicine, and electronics. Synthesis methods for NPs are typically grouped into two categories: “top-down” and “bottom-up” approach. The first involves the division of a massive solid into smaller and smaller portions, successively reaching to nanometer size. This approach may involve milling or attrition. The second, “bottom-up”, method of nanoparticle fabrication involves the condensation of atoms or molecular entities in a gas phase or in solution to form the material in the nanometer range [30-35]. The latter approach is far more popular in the synthesis of NPs owing to several advantages associated with it. Fig. 2.2 shows the general overview of the two approaches.

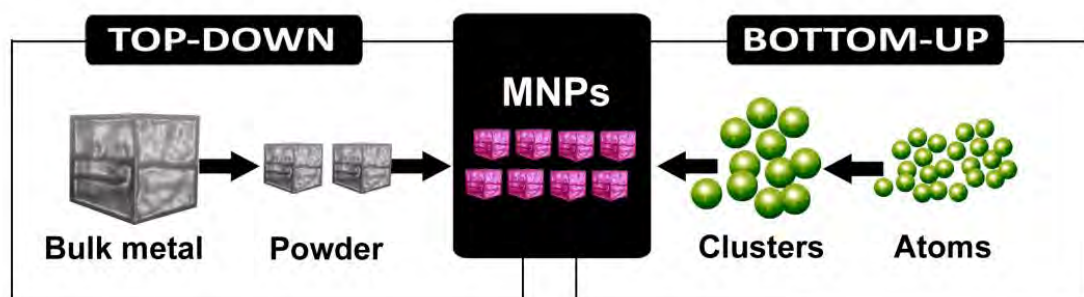


Fig. 2.2: Schematic of bottom up and top down approaches

There are many bottom up methods of synthesizing metal oxide nanomaterials, such as hydrothermal [16], combustion synthesis [17], gas-phase methods [18], microwave synthesis [19], sol-gel processing [20], co-precipitation [21]. Co-precipitation processing techniques will be discussed in detail here because the materials reported in this dissertation were synthesized using this method. However, an overview of other techniques usually employed for the synthesis of nanomaterials is also discussed hereunder.

2.4.1 Combustion method

Combustion synthesis leads to highly crystalline particles with large surface areas [22]. The process involves a rapid heating of a solution containing redox groups. During combustion, the temperature reaches approximately 650° C for one or two minutes making the material crystalline.

2.4.2 Hydrothermal method

Hydrothermal synthesis is typically carried out in a pressurized vessel called an autoclave with the reaction in aqueous solution [23]. The temperature in the autoclave can be raised above the boiling point of water, reaching the pressure of vapor saturation. Hydrothermal synthesis is widely used for the preparation of metal oxide NPs which can easily be obtained through hydrothermal treatment of peptized precipitates of a metal precursor with water [24]. The hydrothermal method can be useful to control grain size, particle morphology, crystalline phase and surface chemistry through regulation of the solution composition, reaction temperature, pressure, solvent properties, additives and aging time.

2.4.3 Gas phase method

Gas phase method is ideal for the production of thin films. Gas phase synthesis can be carried out chemically or physically. Chemical Vapor Deposition (CVD) is a widely used industrial technique that can coat large areas in a short space of time. During the procedure, metal oxide is formed from a chemical reaction or decomposition of a precursor in the gas phase [25]. Physical Vapor Deposition (PVD) is another thin film deposition technique. The process is similar to CVD except that the raw materials/precursors, i.e., the material that is going to be deposited starts out in solid

form, whereas in CVD, the precursors are introduced to the reaction chamber in the gaseous state. The process proceeds atomistically and mostly involves no chemical reactions.

2.4.4 Microwave synthesis

Microwave synthesis is relatively new and an interesting technique for the synthesis of oxide materials [26]. Various nanomaterials have been synthesized in remarkably short time under microwave irradiation [27]. Microwave techniques eliminate the use of high temperature calcination for extended periods of time and allow for fast, reproducible synthesis of crystalline metal oxide nanomaterials. Utilizing microwave energy for the thermal treatment generally leads to a very fine particle in the nanocrystalline regime because of the shorter synthesis time and a highly focused local heating.

2.4.5 Sol-gel method

The sol-gel process is a capable wet chemical process to make ceramic and glass materials. This synthesis technique involves the conversion of a system from a colloidal liquid, named sol, into a semi-solid gel phase [28]. The sol-gel technology can be used to prepare ceramic or glass materials in a wide variety of forms: ultra-fine or spherical shaped powders, thin film coatings, ceramic fibres, microporous inorganic membranes, monolithics, or extremely porous aerogels.

2.4.6 Co-precipitation method

Among the various techniques for magnetite synthesis, the coprecipitation method is a convenient way to synthesize magnetite NPs from an aqueous iron salt ($\text{Fe}^{2+} + \text{Fe}^{3+}$) solution; a base is simply added under an inert atmosphere at room temperature. The coprecipitation process does not produce or use any toxic intermediates or solvents, does not require precursor complexes, and proceeds at temperatures under 100 °C. This process has been recognized for its industrial importance because of its ability to be scaled up, its reproducibility, and its eco-friendly reaction conditions. However, it yields particles with a broad size distribution, probably because of the complicated set of pathways that lead to the formation of Fe_3O_4 .

2.4.7 Plant extract mediated bio-synthesis

The biological method provides a wide range of resources for the synthesis of NPs due to the use of biological agents like bacteria, fungi, actinomycetes, yeast and plants which is also called green chemistry approach. The rate of reduction of metal ions using biological agents is found to be much faster and also at ambient temperature and pressure conditions [29]. Plant extracted mediated Fe₃O₄ NPs synthesis has led to a remarkable progress in a green synthesis protocol for many NPs synthesis, Fig. 2.3 shows some images of plants that were used for Fe₃O₄ NPs synthesis.

Table 2.2: Biosynthesis of Fe₃O₄ NPs from biological sources

Plants extracts			
Extracts source	Particle size (nm)	Shapes	References
Green Tea	40–60	Amorphous	[30]
<i>Azadirachta indica</i>	100	Spherical	[31]
<i>Eucalyptus Tereticornis</i>	40-60	Cubic	[32]
Grape	50-100	Amorphous	[33]
<i>Eucalyptus globules</i>	50-100	Spherical	[34]
<i>Tridax procumbens</i>	80-100	Crystalline	[35]
<i>Punica granatum</i>	100-200	Spherical	[36]
Sorghum	40-50	Spherical	[37]
Bacterium			
<i>Actinobacter sp.</i>	50	Cubic	[38]
<i>Bacillux subtilis</i>	60-80	Spherical	[39]
Fungi			
<i>Aspergillus</i>	50-200	Irregular, spherical	[40]
<i>Fusarium oxysporum</i>	40-50	Spherical	[41]
Algae			
<i>Chlorococcum sp.</i>	30-50	Spherical	[42]

Due to the diversity of plants, NPs synthesis from plants has known an interesting subject across the world as different plant species are being rapidly investigated and used in NPs synthesis [43]. Table 2.2 reports some of typical examples of biological

sources of Fe₃O₄ NPs. Due to the biodiversity of plant, bacteria and fungi, Fe₃O₄ with different particle sizes can be extracted easily in a lot of amount.

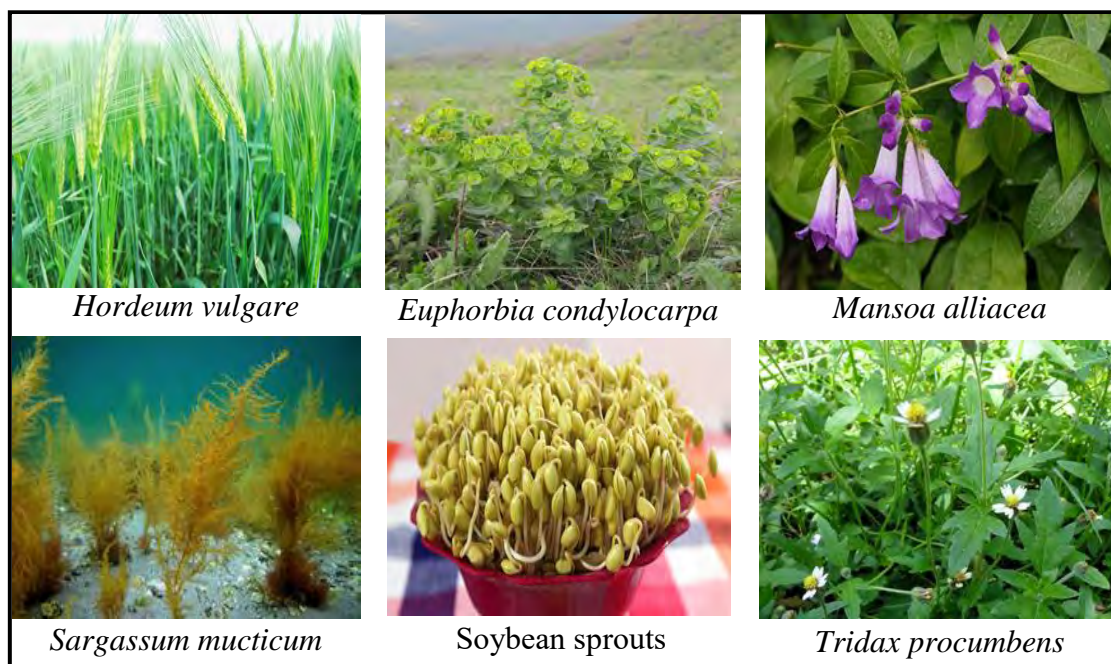


Fig. 2.3: Plants used for Fe₃O₄ NPs synthesis

2.5 Biomedical applications of NPs

Since nanomaterials possess unique, beneficial chemical, physical, and mechanical properties, they can be used for a wide variety of applications. Biomedical application of nanotechnology in medicine (sometimes referred to as nanomedicine) involves techniques already being used or currently under development, as well as longer range research into the use of manufactured nano-robots to make repairs at the cellular level. Nanomedicine could revolutionize the way we detect and treat damage to the human body and disease [44].

i. Earlier detection

We know that the earlier a disease can be detected, the easier it is to remedy. To achieve this, research is focusing on introducing into the body specially designed NPs. These NPs are composed of tiny fluorescent 'quantum dots' that are 'bound' to targeting antibodies. In turn, these antibodies bind to diseased cells. When this happens, the quantum dots fluoresce brightly. This fluorescence can be picked up by

new, specially developed, advanced imaging systems, enabling the accurate pinpointing of a disease even at a very early stage [45].

ii. Faster diagnosis

Nanotechnology is also leading to faster diagnosis. Diagnosis can be a lengthy and stressful business, usually with a test sample having to be sent away for analysis. The results can take several days or even weeks to arrive. Nanotechnology is enabling much faster and more precise diagnosis, as many tests can be built into a single, often palm-sized device that only requires tiny quantities of sample [46]. This device is sometimes called a 'lab-on-a-chip', and samples can be processed and analyzed so rapidly that the results can be read out almost instantaneously.

iii. Targeted drug delivery

People often complain that the cure for a disease can feel almost as bad as the disease itself, as prescription drugs may have unpleasant side effects. This is because the body needs to be flooded with very high doses of a drug in order to ensure that a sufficient volume reaches the site of the disease. Accurate targeting of the drug can now be achieved, using specially designed drug-carrying NPs [47]. This also means that much smaller quantities of a drug are necessary, reducing toxicity to the body. The drug is then activated only at the disease site (such as a tumour) by light or other means, and the progress of the cure can also be monitored using advanced imaging techniques.

iv. Magnetic hyperthermia

Magnetic hyperthermia is an experimental treatment for cancer. It is theoretically based on the fact that magnetic NPs can transform electromagnetic energy from an external high-frequency field to heat. As a result, if magnetic NPs are put inside a tumor and the whole patient is placed in an alternating magnetic field, the tumor temperature will rise. The elevation of temperature may enhance tumor oxygenation and radio- and chemosensitivity, hopefully shrinking tumors [48]. This experimental cancer treatment has also been investigated for the aid of other ailments, such as bacterial infections. Many magnetic materials display a magnetic hysteresis when subjected to a magnetic field that alternates direction. This hysteresis cycle represents work which is dissipated in the environment as thermal energy. This heat is

undesirable in many industrial applications, though it is the basis of magnetic hyperthermia. This power is often called the "Specific Absorption Rate" and it is usually expressed in watts per gram of NPs.

v. Anti-microbial techniques

Researchers are attempting to use nanotechnology-based techniques to develop new methods for fighting bacterial infections. NPs can help fight staph infections, burns, and other conditions eradicating or avoiding bacterial infection. It's possible that these nano-techniques could remove bacterial infection in minutes, rather than in weeks as is currently the case with antibiotics.

vi. Nanorobots

Many future applications of nanomedicine will be based on the ability to build and develop nanorobots. In the future these nanorobots could actually be programmed to repair specific diseased cells, functioning similarly to antibodies in our natural healing processes.

vii. Cytotoxicity

The special physicochemical properties of NPs cause potential risk to human health [49]. So, considerable effort has been made to identify the potential toxicity of NPs to cells and organism. Exposure of cells to certain type NPs can induces cytotoxicity and many effects like oxidative injury, inflammation, fibrosis, and release of pro-inflammatory mediators. The pathophysiological responses have also been found like generation of ROS (Reactive oxygen species) in cells when cells are exposed to NPs. This ROS generation is the initiating factor for toxicity of NPs exposed to cells. Another initiating factor was liposomal destabilization. Loss of mitochondrial membrane integrity causes cell death. NPs cause toxicity because: a) nanostructures have electronic, optical and magnetic properties that tell about the physical dimensions and breakage in the nanostructures can lead to a unique toxic effect that is unpredictable b) The surfaces of nanostructures are involved in many catalytic and oxidative reaction. These reactions may induce cytotoxicity. Cytotoxicity can be greater in the nanomaterial than a bulk material because surface to volume ratio for NPs is more c) Some nanostructures contain metals or compound with toxicity when breakdown can reduce toxic responses to the components themselves [50]. Common

assumption about the nanostructures is that smaller size of nanostructures can easily enter into tissues, cells, organelles and functional biomolecular structures, as the actual size of engineered nanostructures is similar to many biological molecules and structures. The entry of the nanostructures into biological systems can cause damage, which can cause harm to human health. Nanostructures can enter biological system via six principle routes: intra venous, dermal, subcutaneous, inhalation, intraperitoneal, and oral. After enter absorption takes place where nanostructures first interact with biological component like proteins, cells. Then they are distributed to various organs in body and may be structurally same, may be modified or metabolized.

2.6 Metal oxide NPs

In periodic table more than 75% of elements are metallic in nature such as gold, silver, platinum, mercury, uranium, aluminum, sodium, calcium etc. The metallic compounds which are formed with metal and oxygen in the form of oxide ion (O^{2-}) are called as metal oxide. Metal oxides represent an appealing and assorted class of materials whose properties cover the entire range from metals to semiconductors to insulators and almost all aspects of material science, chemistry, and physics in a very broad application.

The metal oxide NPs have various functions which are not observed in bulk phase [51]. All these are studied broadly due to their exclusive electronic, magnetic, optical, catalytical and antimicrobial properties of wound healing and also for anti-inflammatory properties. The metal oxide NPs have the surface plasmon resonance absorption in the UV-visible region [52]. Over the past few decades, the structure of inorganic NPs exhibits appreciable, drastic, novel and highly improved physical, chemical and biological properties with well recognized function due to their nanoscale size [53]. Recent studies reported that NPs of some materials including metal oxides can also induce the cell death in eukaryotic cells and the growth inhibition in prokaryotic cells due to cytotoxicity nature.

2.7 Magnetic NPs classifications

Magnetic particles capable of forming superparamagnetic dispersions in a carrier fluid are comprised of metals and metal oxides with length scales from 1 to 100 nm. These

metals and metal oxides include Ni, Co, Fe, Fe₃O₄ and γ -Fe₂O₃. The pure metals have the highest magnetic susceptibility (Table 2.3). However, these transition metals are highly toxic and extremely sensitive to oxidation. Under atmospheric conditions Ni, Co and Fe oxidize to NiO, CoO and FeO alloys, which are antiferromagnetic. Presently, there are no synthetic and/or physical methods to prevent the oxidation mechanism, which is a significant problem for NPs due to their large surface area.

Table 2.3: Saturation magnetization and curie temperature for several transition metals and metal oxides [22, 36]

Substances	Saturation magnetization (M _s) (emu/cm ⁻³) at 298K	Curie temperature T _C (K)
Ni	485	631
Co (cubic)	1400 – 1422	1404
Fe (cubic)	1700 -1714	1043
γ -Fe ₂ O ₃	394[26]	820 – 986
Fe ₃ O ₄	480 – 500	858
MnO.Fe ₂ O ₃	410	573
CoO.Fe ₂ O ₃	400	793
CuO.Fe ₂ O ₃	135	858
NiO.Fe ₂ O ₃	270	728

Currently researchers are investigating synthetic and physical methods to protect Co NPs. Therefore, iron oxides, despite their initial lower magnetization, offer great potential as oxidatively stable nanomagnetic particles with diverse application possibilities in oxygen rich environments.

2.7.1 Iron oxides

Iron oxide exists in a variety of chemical compositions and with different magnetic properties (Table 2.4). Materials of interest to magnetically guidable systems are iron oxides such as γ -Fe₂O₃, Fe₃O₄ and MO.Fe₂O₃ (where M is Mn, Co, Ni, or Cu) because they display ferrimagnetism. As mentioned above ferrimagnetic iron oxides inherently display a lower magnetic response than ferromagnetic materials, such as

the transition metals. However, the iron oxides are also less sensitive to oxidation and therefore maintain stable magnetic responses.

Table 2.4: Iron oxyhydroxide and iron oxide species

Mineral	Formula	Magnetic Response
Goethite	α -FeOOH	Antiferromagnetic
Akaganeite	β -FeOOH	Antiferromagnetic
Lepidocrocite	γ -FeOOH	Antiferromagnetic
Feroxyhyte	δ -FeOOH	Ferrimagnetic
Ferrihydrite	$\text{Fe}_3\text{HO}_8 \cdot 4\text{H}_2\text{O}$	Antiferromagnetic
Hematite	α - Fe_2O_3	Weakly ferrimagnetic
Maghemite	γ - Fe_2O_3	Ferrimagnetic
Magnetite	Fe_3O_4	Ferrimagnetic

Magnetite and maghemite are the most common and intensely researched iron oxides. The mixed metal $\text{MO} \cdot \text{Fe}_2\text{O}_3$ ferrites have varying physical and magnetic properties and are commonly developed for electronics applications due to particle shape and subsequent single domain nature. A significant amount of research has been reported regarding the mixed metal ($\text{MO} \cdot \text{Fe}_2\text{O}_3$) ferrites [54, 55, 56].

Magnetite and maghemite are similar in physical properties and crystalline structure (Table 2.5). Both display ferrimagnetism, however maghemite has lower saturation magnetization. The difference in their magnetic response is due to sub-lattice interactions. Maghemite is structurally γ - Fe_2O_3 which is comprised solely of Fe^{3+} ions. In the crystalline structure half of the Fe^{3+} ions are tetrahedrally coordinated and the other half are octahedrally coordinated. Magnetite is comprised of Fe^{2+} and Fe^{3+} ions in a 1:2 molar ratio, $\text{FeO} \cdot \text{Fe}_2\text{O}_3$, where half of the Fe^{3+} ions are tetrahedrally coordinated and the other half are octahedrally coordinated and all of the Fe^{2+} are octahedrally coordinated.

Their Curie temperatures (T_C) are sufficiently high so that both are applicable in a variety of magnetically responsive applications. However, maghemite T_C is difficult to measure because it converts to hematite above 713K.

Table 2.5: Physical properties of magnetite and maghemite [57, 58]

Mineral	Crystal System	Cell dimensions a_0 (nm)	Density (g/cm ³)	Color	Magnetic susceptibility (emu/g)	Curie Temperature T_C (K)
Magnetite	Cubic	0.839	5.26	Black	90 ^[58] – 98 ^[26]	850
Maghemite	Cubic or tetragonal	0.834	4.87	Reddish-brown	76 ^[58] – 81 ^[26]	820-986

Since both iron oxide forms are ferrimagnetic and stabilized in carrier fluids by similar mechanisms, equal focus has been shown in literature. Specific procedures for the formation of magnetite and maghemite are different; however, in practice mixtures of the two are easily obtained if a high level of care is not taken experimentally. The sensitivity of reagent stoichiometry and a large number of other reaction parameters often complicate the ability to obtain pure magnetite crystalline structures. The focus of this review will be on magnetite formation. However, because the mechanisms of stabilization are similar, maghemite procedures are included when the relevance of the research is justified.

2.7.1.1 Hematite

Hematite, α -Fe₂O₃, is the oldest known Fe oxide mineral and is widespread in rocks and soils. It is extremely stable and is often the final stage of transformations of other iron oxides. The blood-red-coloured hematite is an important pigment and a valuable ore. Other names for hematite include iron (III) oxide, ferric oxide, red ochre and kidney ore.

2.7.1.2 Maghemite

Maghemite, $\gamma\text{-Fe}_2\text{O}_3$, is a red-brown, ferromagnetic mineral isostructural with magnetite, but with cation deficient site. It occurs in soils as a weathering product of magnetite or as the product of heating of other Fe oxides, usually in the presence of organic matter.

2.7.1.3 Magnetite

Fe_3O_4 is a black, ferromagnetic mineral containing both Fe (II) and Fe (III). Together with titanomagnetite, it is responsible for the magnetic properties of rocks. It is formed in various organisms in which it serves as an orientation aid. Other names for magnetite include black iron oxide, magnetic iron ore, iron (II, III) oxide and ferrous ferrite.

The chemical composition of magnetite is $\text{Fe}^{2+}\text{Fe}_2^{3+}\text{O}_4^{2-}$. The main details of its structure were established in 1915. It was one of the first crystal structures to be obtained using XRD. The structure is inverse spinel, with O^{2-} ions forming a face centered cubic lattice and iron cations occupying interstitial sites. Half of the Fe^{3+} cations occupy tetrahedral sites while the other half, along with Fe^{2+} cations, occupy octahedral sites. Magnetite contains both ferrous and ferric iron, requiring environments containing intermediate levels of oxygen availability to form.



Fig. 2.4: Fe_3O_4 NPs powder

2.7.1.3.1 Crystal structure of magnetite

Fe_3O_4 has an inverse spinel crystal structure with face centered cubic unit cell where oxygen ions are placed regularly in cubic close packed positions along the $[111]$ axis [59]. Fe_3O_4 oxygen ion array contains holes partially filled with ferric and ferrous ions [27, 59]. The unit cell is comprised of 56 atoms: 32 O^{2-} anions, 16 Fe^{3+} cations and 8 Fe^{2+} cations. Magnetite chemical formula is Fe_3O_4 , however more appropriately Fe_3O_4 is defined as $\text{FeO}\cdot\text{Fe}_2\text{O}_3$. The inverse spinel structure is arranged such that half of the Fe^{3+} ions are tetrahedrally coordinated and the remaining half of Fe^{3+} and all of the Fe^{2+} are octahedrally coordinated, which is shown in Fig. 2.5.

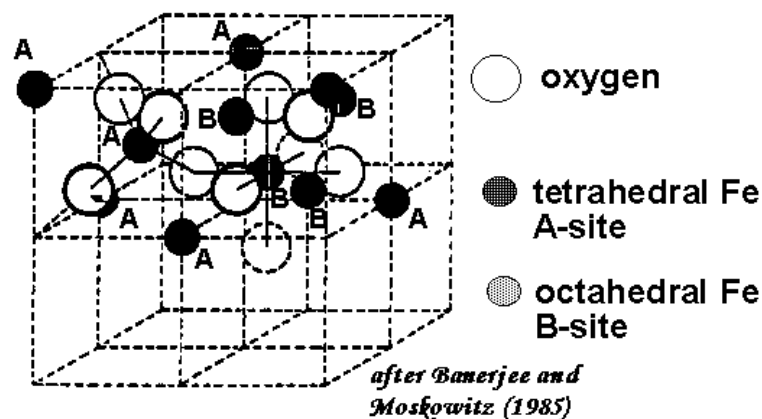


Fig. 2.5: Inverse spinel crystalline structure of magnetite [60]

2.7.1.3.2 Physical properties of magnetite

In accordance with many classroom discussions and examples, the effective surface area of nano-magnetite should increase with decreasing particle size. Fig. 2.6 demonstrates the theory of this supposition. Colloidal magnetite solutions are typically characterized by the jet-black color, hence no color change between bulk-scale and nano-scale magnetite is observed. Unit cell swelling should cause subsequent reduction in density; however, no experimental data confirming this assumption was located. Fe_3O_4 NPs are assumed nonporous. No information regarding hardness, free energy, or solubility of magnetite NPs could be gathered.

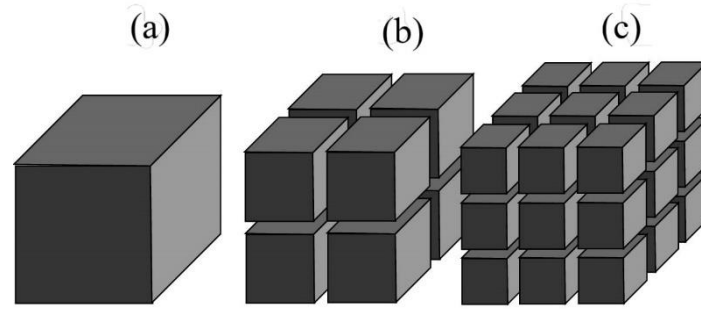


Fig. 2.6: Increasing effective surface area with decreasing particle size

- (a) Area of each face = $1 \times W = 3'' \times 3'' = 9 \text{ in}^2$
 total SA = 6 faces $\times 9 \text{ in}^2 = 54 \text{ in}^2$
- (b) Area of each face = $1 \times W = 1.5'' \times 1.5'' = 2.25 \text{ in}^2$
 total SA = 6 faces $\times 8 \text{ blocks} \times 2.25 \text{ in}^2 = 108 \text{ in}^2$
- (c) Area of each face = $1 \times W = 1'' \times 1'' = 1 \text{ in}^2$
 total SA = 6 faces $\times 27 \text{ blocks} \times 1 \text{ in}^2 = 162 \text{ in}^2$

2.7.1.3.3 Thermal properties of magnetite

In 1909, Iwan Petrowitsch Pawlow predicted that decreasing particle diameter should generate lower melting points, according to Equation 2.1.

$$\frac{T_m(r)}{T_m(\infty)} = 1 - \frac{4v_s^{2/3}}{L} \left(\gamma_s \cdot 2v_s^{2/3} - \gamma_l \cdot 2v_l^{2/3} \right) \cdot \frac{1}{d} \dots\dots\dots (2.1)$$

where T_m , v , L , γ , d , s , l , and ∞ are represent melting temperature, specific molar volume, molar heat of fusion, surface tension, particle diameter, solid phase, liquid phase, and bulk phase, respectively. No information regarding magnetite's surface tension could be found towards utilization of Pawlow's equation; however, a decline in melting/boiling temperatures of nano-scale magnetite can be assumed.

No information regarding heats of fusion, decomposition, or vaporization of magnetite NPs could be gathered; however, as reduction in melting point is established, subsequent reduction in heats of fusion, decomposition, or vaporization can be deduced through logic and comparison with other materials.

2.7.1.3.4 Magnetic properties of magnetite

The magnetization of bulk magnetite as ferrimagnetic, generated by parallel alignment of magnetic moments on tetrahedral sites and anti-parallel alignment of ferrous and ferric spins on octahedral sites. Typical ferrimagnetic behavior exerts coercivity and remanence (retentivity) [61] as displayed in Figure 2.7. As particle size is decreased, the amount of exchange-coupled spins resisting spontaneous magnetic reorientation is decreased, tending towards paramagnetic or superparamagnetic magnetization [62]. Consequentially, decreasing magnetite particle size should demonstrate reduced ferrimagnetic and enhanced superparamagnetic behavior. Similarly, increasing temperatures enhance thermal energy of particles and thus facilitate magnetic reorientation, or superparamagnetic magnetization [63]. In accordance with superparamagnetic behavior, Fe_3O_4 NPs exhibit zero coercivity and remanence in hysteresis loops as illustrated in Fig. 2.8. Coercivity slowly builds as magnetite

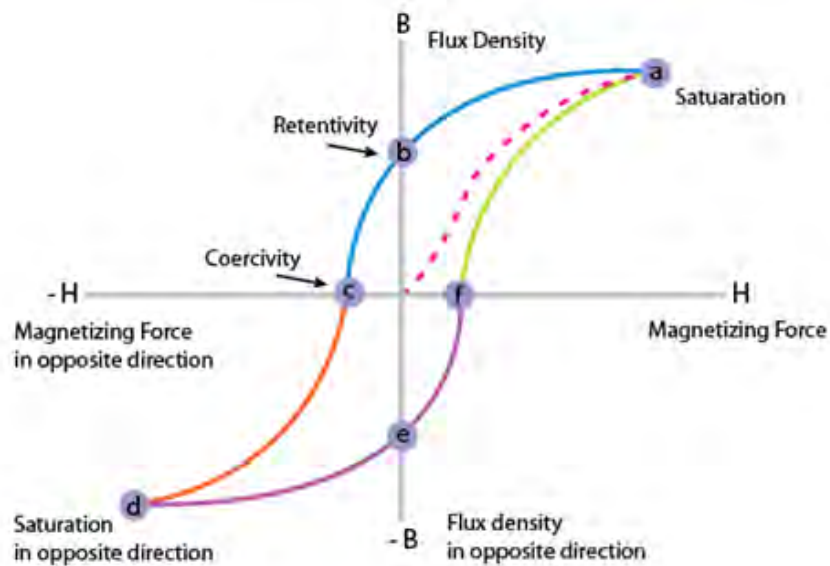


Fig. 2.7: Generic ferrimagnetic hysteresis loop

particle diameter increases. Reduction in particle size also affects the Curie temperature, which defines the critical temperature where magnetization changes from ferrimagnetic to superparamagnetic. Naturally, if superparamagnetic magnetism dominates at room temperature, the effective Curie temperature of magnetite NPs (738 K) must be lower. Indeed, the higher proportion of surface spins in nanoscale particles enhances the dipolar anisotropy, lowering the Curie temperature [64] (temperature at which single-ion and dipolar anisotropy terms are equivalent).

Saturation magnetization in nano-scale magnetite particles follows two distinct patterns as particle size decreases. EPMA analyses suggest that particle size reduction spurs relative oxygen concentration decline, causing slight reduction in iron valence states [65].

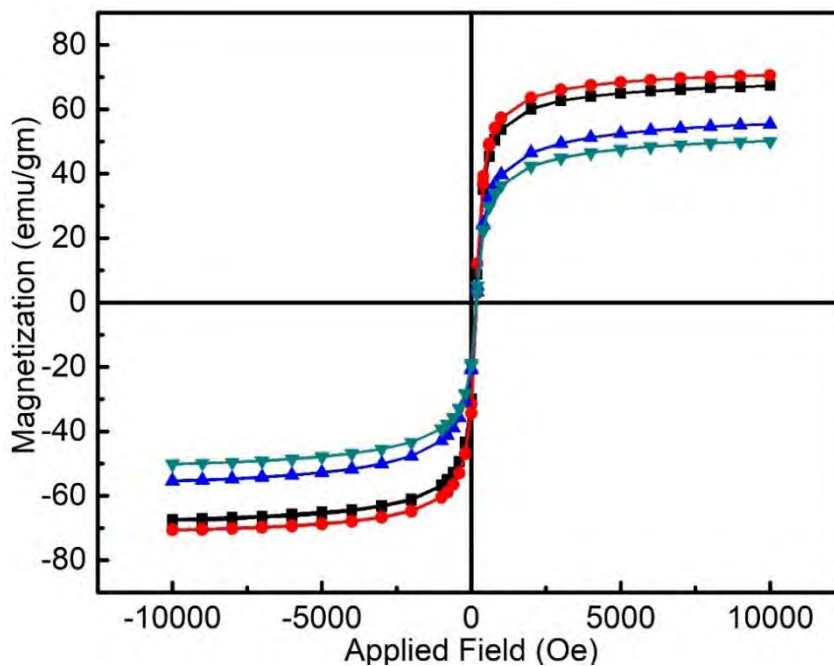


Fig. 2.8: Absence of hysteresis loop implies superparamagnetism [66].

This scenario generates greater ferrous ion content; since the ultimate magnetic moment depends upon ferrous species, subsequent increase in magnetization should be observed. Magnetization varies along particle diameter with greater magnitude within the particle and lower magnitude near the surface. Therefore, as particle diameter is decreased, surface effects will eventually affect saturation magnetization.

Researchers have discovered that below 10 nm, saturation magnetization suddenly reversed trend and began decreasing with particle size.

Basically, at extremely small nanoparticle dimensions (diameter < 10 nm), saturation magnetization decreases with decreasing particle size because surface effects. Magnetite is electronic configuration consists of unpaired 3d electrons, which impart net magnetic moments. The spins of the tetrahedrally (A) coordinated Fe^{3+} and the spins of the octahedrally (B) coordinated Fe^{3+} and Fe^{2+} are antiparallel and unequal in magnitude (Figure 2.9). Below the Curie temperature (850K) these interpenetrating sub lattices aligned antiparallel with unequal moments give rise to the observed ferrimagnetism. The spin arrangements of the two interpenetrating sub lattices of the octahedrally coordinated Fe^{2+} and Fe^{3+} are coupled ferromagnetically via a double-exchange mechanism associated with inter-ion electron transfer (Figure 2.9) [67]. The easy axis of magnetite is the cube edge. The crystalline magnetic anisotropy constant (K) for magnetite is $1.4 \times 10^5 \text{ erg/cm}^3$ and the superparamagnetic maximum critical particle size estimated from $kV \sim 25 \text{ KT}$ is $\sim 25 \text{ nm}$, which is lower than the single domain critical size in Table 2.6 [68].

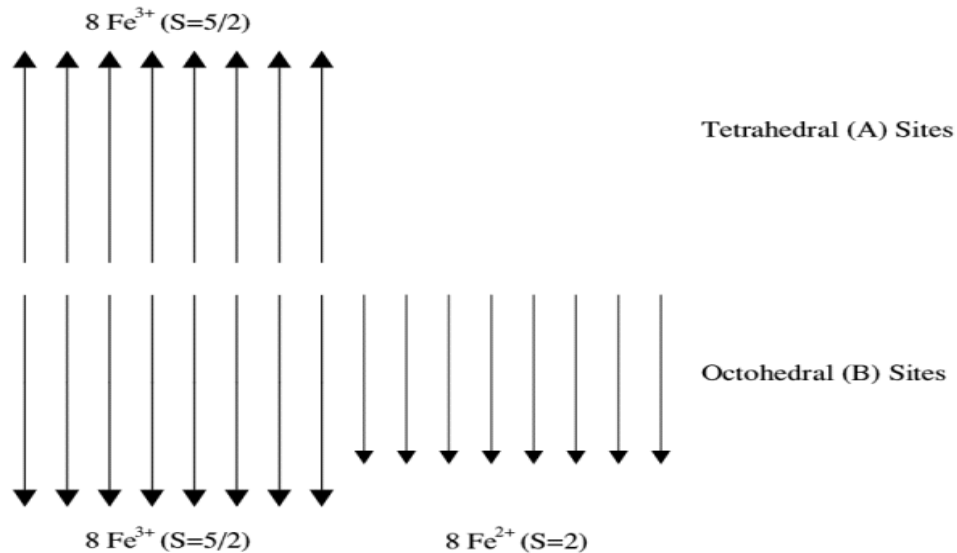


Fig. 2.9: Spin arrangements in Fe_3O_4 , and the double exchange interaction with inter-ion electron transfer [79]

Table 2.6: Estimated maximum single-domain size for spherical particles [69]

Material	Single domain diameter D_s (nm)
Fe	14
Co	70
Ni	55
Fe_3O_4	128
γ - Fe_2O_3	166

2.7.1.3.5 Surface chemistry of magnetite

When considering the properties and application of magnetic NPs, the surface properties and chemistry are of great significance. The surface Fe atoms, which were not bound to oxygen atoms at the surface act as Lewis acids and therefore coordinate with molecules that donate lone pair electrons, Lewis bases. Therefore, in aqueous systems the Fe atoms coordinate with water, which dissociates readily to leave the iron oxide surface hydroxyl functionalized. Surface hydroxyl groups are amphoteric and may therefore react with either acids or bases [70]. In aqueous dispersions the surface of magnetite will be either positive or negative, depending on the pH of the solution. The isoelectric point is the pH where the surface displays an equal number of negative and positive surface charges. The isoelectric point of magnetite is observed at a pH of 6.8 [71]. Stabilization of magnetite NPs can be achieved by electrostatic double layer, steric stabilization or by modifying the isoelectric point with a citrate or silica coating. The stabilization of the iron oxide NPs is crucial to obtain magnetic colloidal ferrofluids stable against aggregation in an applied magnetic field.

2.8 Bacteria

Bacteria is an organism that thrive in diverse environments. They can live within soil, in the ocean and inside the human gut. Humans' relationship with bacteria is complex.

Sometimes they lend a helping hand, by curdling milk into yogurt, or helping with our digestion. At other times they are destructive, causing diseases like pneumonia. There are two types of bacteria (a) gram-positive bacteria and (b) gram-negative bacteria.

2.8.1 Gram-positive bacteria

Gram-positive bacteria are bacteria that give a positive result in the Gram stain test, which is traditionally used to quickly classify bacteria into two broad categories according to their cell wall. Gram-positive bacteria take up the crystal violet stain used in the test, and then appear to be purple-colored when seen through a microscope

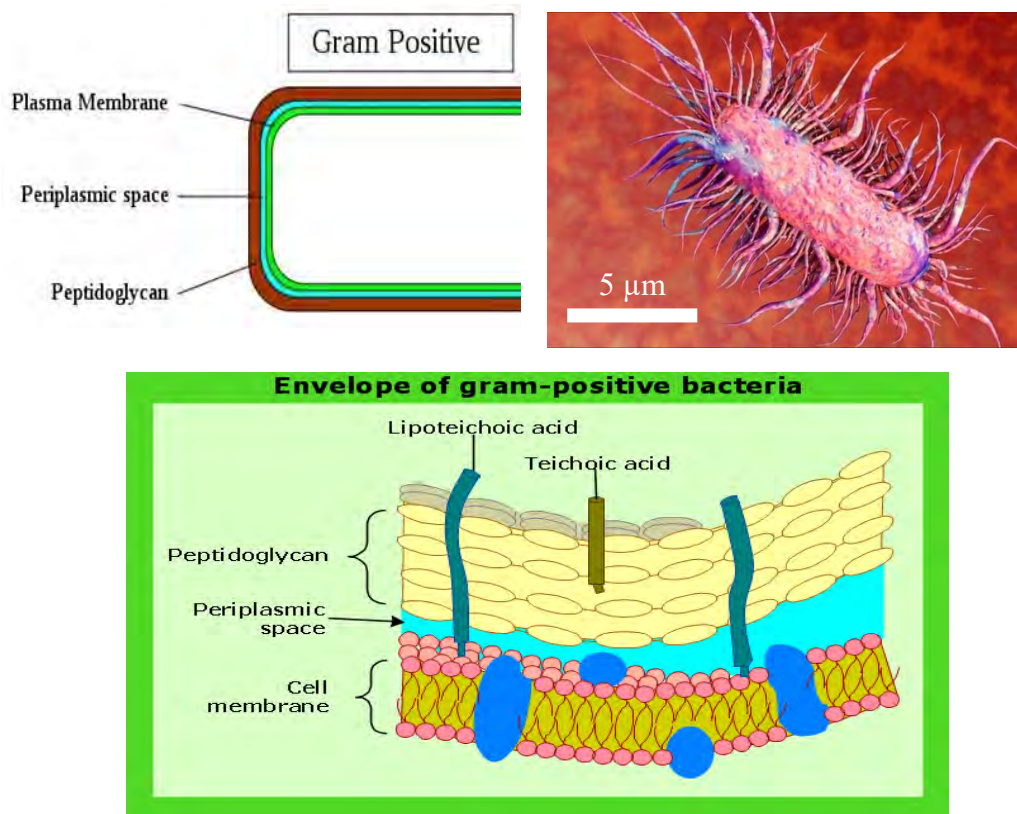


Fig. 2.10: Gram positive bacteria

(Fig. 2.10). This is because the thick peptidoglycan layer in the bacterial cell wall retains the stain after it is washed away from the rest of the sample, in the decolorization stage of the test.

In general, the following characteristics are present in Gram-positive bacteria:

1. Cytoplasmic lipid membrane.
2. Thick peptidoglycan layer.
3. Teichoic acids and lipids are present, forming lipoteichoic acids, which serve as chelating agents, and also for certain types of adherence.
4. Peptidoglycan chains are cross-linked to form rigid cell walls by a bacterial enzyme DD-transpeptidase.
5. A much smaller volume of periplasm than that in gram-negative bacteria.

2.8.2 Gram-negative bacteria

Gram-negative bacteria are bacteria that do not retain the crystal violet stain used in the gram-staining method of bacterial differentiation. They are characterized by their cell envelopes, which are composed of a thin peptidoglycan cell wall sandwiched between an inner cytoplasmic cell membrane and a bacterial outer membrane (Fig. 2.11).

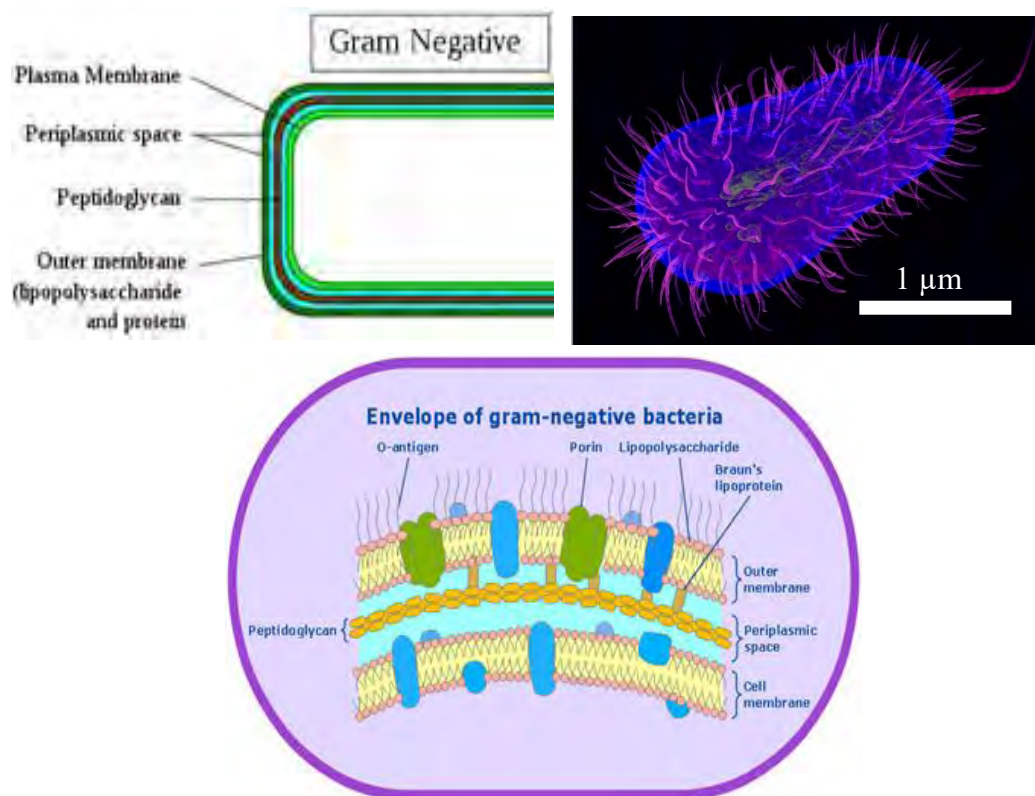


Fig. 2.11: Gram negative bacteria

Gram-negative bacteria display these characteristics:

1. An inner cell membrane is present (cytoplasmic).
2. A thin peptidoglycan layer is present (This is much thicker in gram-positive bacteria).
3. Has outer membrane containing lipopolysaccharides (LPS, which consists of lipid, core polysaccharide and antigen) in its outer leaflet and phospholipids in the inner leaflet.
4. Porins exist in the outer membrane, which act like pores for particular molecules.
5. Between the outer membrane and the cytoplasmic membrane there is a space filled with a concentrated gel-like substance called periplasm.
6. The S-layer is directly attached to the outer membrane rather than to the peptidoglycan.
7. If present, flagella have four supporting rings instead of two.
8. Teichoic acids or lipoteichoic acids are absent.
9. Lipoproteins are attached to the polysaccharide backbone.
10. Some contain Braun's lipoprotein, which serves as a link between the outer membrane and the peptidoglycan chain by a covalent bond.
11. Most, with very few exceptions, do not form spores.

2.9 Antibiotics resistance bacteria

Antimicrobial resistance is the ability of a microbe to resist the effects of medication that once could successfully treat the microbe. The term antibiotic resistance is a subset of antimicrobial resistance, as it applies only to bacteria becoming resistant to antibiotics [72]. Resistant microbes are more difficult to treat, requiring alternative medications or higher doses of antimicrobials. These approaches may be more expensive, more toxic or both. Microbes resistant to multiple antimicrobials are called multidrug resistant. Those considered extensively drug resistant or totally drug resistant are sometimes called "superbugs".

Resistance arises through one of three mechanisms: natural resistance in certain types of bacteria, genetic mutation, or by one species acquiring resistance from another. All

classes of microbes can develop resistance. Fungi develop antifungal resistance. Viruses develop antiviral resistance. Protozoa develop antiprotozoal resistance, and bacteria develop antibiotic resistance. Resistance can appear spontaneously because of random mutations. However, extended use of antimicrobials appears to encourage mutations which can render antimicrobials ineffective.

Antibiotic medications are used to kill bacteria, which can cause illness and disease. They have made a major contribution to human health. Many diseases that once killed people can now be treated effectively with antibiotics. However, some bacteria have become resistant to commonly used antibiotics. Antibiotic resistant bacteria are bacteria that are not controlled or killed by antibiotics [73]. They are able to survive and even multiply in the presence of an antibiotic. Most infection-causing bacteria can become resistant to at least some antibiotics. Bacteria that are resistant to many antibiotics are known as multi-resistant organisms. A list of antibiotic resistant bacteria is provided in table 2.7

Table 2.7: List of antibiotics resistance bacteria [74]

Priority	Bacteria	Resistance antibiotics
Critical	<i>Acinetobacter baumannii</i>	carbapenem-resistant
	<i>Pseudomonas aeruginosa</i>	carbapenem-resistant
	<i>Enterobacteriaceae</i>	carbapenem-resistant
High	<i>Enterococcus faecium</i>	vancomycin-resistant
	<i>Staphylococcus aureus</i>	methicillin-resistant
	<i>Helicobacter pylori</i>	clarithromycin-resistant
	<i>Campylobacter spp.</i>	fluoroquinolone-resistant
	<i>Salmonellae</i>	cephalosporin-resistant
Medium	<i>Streptococcus pneumoniae</i>	penicillin-non-susceptible
	<i>Haemophilus influenzae</i>	ampicillin-resistant
	<i>Shigella spp.</i>	fluoroquinolone-resistant

2.10 Structure of lipid bilayer

The lipid bilayer (or phospholipid bilayer) is a thin polar membrane made of two layers of lipid molecules. These membranes are flat sheets that form a continuous

barrier around all cells. The cell membranes of almost all living organisms and many viruses are made of a lipid bilayer, as are the membranes surrounding the cell nucleus and other sub-cellular structures.

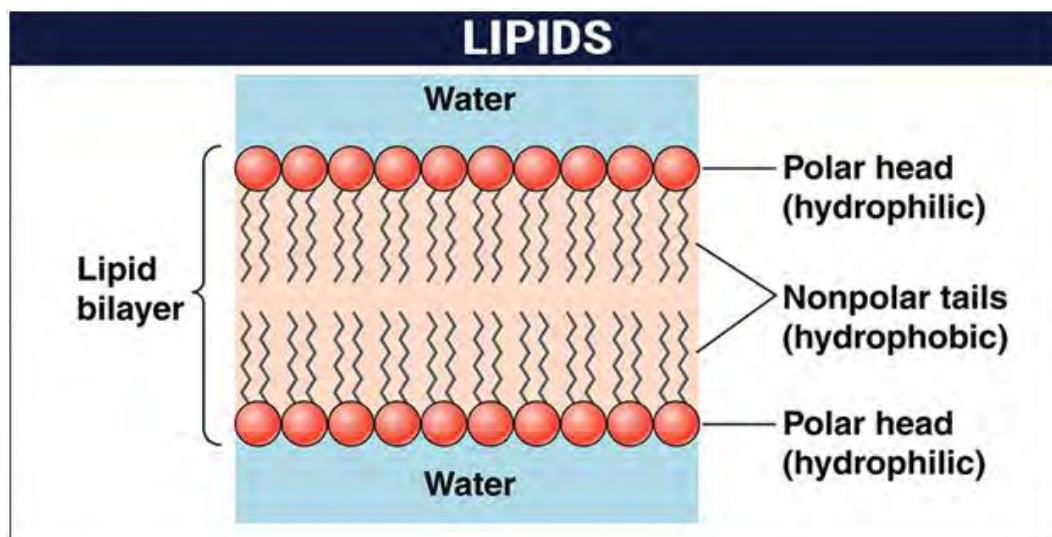


Fig. 2.12: Schematic diagram of lipid bilayer

The lipid bilayer is the barrier that keeps ions, proteins and other molecules where they are needed and prevents them from diffusing into areas where they should not be. Lipid bilayers are ideally suited to this role, even though they are only a few nanometers in width, they are impermeable to most water-soluble (hydrophilic) molecules. Bilayers are particularly impermeable to ions, which allows cells to regulate salt concentrations and pH by transporting ions across their membranes using proteins called ion pumps. Biological bilayers are usually composed of amphiphilic phospholipids that have a hydrophilic phosphate head and a hydrophobic tail consisting of two fatty acid chains. Phospholipids with certain head groups can alter the surface chemistry of a bilayer and can, for example, serve as signals as well as "anchors" for other molecules in the membranes of cells [75]. Just like the heads, the tails of lipids can also affect membrane properties, for instance by determining the phase of the bilayer. The bilayer can adopt a solid gel phase state at lower temperatures but undergo phase transition to a fluid state at higher temperatures, and the chemical properties of the lipids' tails influence at which temperature this happens. The packing of lipids within the bilayer also affects its mechanical properties, including its resistance to stretching and bending. Many of these properties have been

studied with the use of artificial "model" bilayers produced in a lab. Vesicles made by model bilayers have also been used clinically to deliver drugs.

Biological membranes typically include several types of molecules other than phospholipids [76]. A particularly important example in animal cells is cholesterol, which helps strengthen the bilayer and decrease its permeability. Cholesterol also helps regulate the activity of certain integral membrane proteins. Integral membrane proteins function when incorporated into a lipid bilayer, and they are held tightly to lipid bilayer with the help of an annular lipid shell. Because bilayers define the boundaries of the cell and its compartments, these membrane proteins are involved in many intra- and inter-cellular signaling processes. Certain kinds of membrane proteins are involved in the process of fusing two bilayers together. This fusion allows the joining of two distinct structures as in the fertilization of an egg by sperm or the entry of a virus into a cell. Because lipid bilayers are quite fragile and invisible in a traditional microscope, they are a challenge to study. Experiments on bilayers often require advanced techniques like electron microscopy and atomic force microscopy.

2.10.1 Critical size of NPs for pore formation in lipid bilayer

Biological function is the result of a series of complex and diverse events mutually connected over several length scales. Peculiar examples are the hierarchical features of silk formation cell motility or gecko foot grip. Although ubiquitous in Nature, this paradigm has never been exploited to describe the membrane-NPs interface. NPs size is akin to biological macromolecules, including proteins, lipids and other components of cell membranes. In biological environments, this size matching combines with the NPs high surface energy to drive a vigorous and intricate trade between the NPs and these biological entities. It follows that the "biological identity" of NPs is ultimately determined by the size, composition, structure and time evolution of the solid-liquid interface that separates them from the biological environment, the NP-protein corona being probably the most prominent example of such an interface. This subject remains to date one of the primary factors that should be addressed to take medical applications of nanomaterials to the next level and to rationally address some key aspects of nanotoxicology. Cellular internalization and trafficking of NPs are among the most controversial subjects in the area. Some of the underpinning mechanisms are connected to receptor-mediated pathways, while others are lipid-mediated and

determined by membrane composition, NPs size, shape and surface chemistry. On top, unambiguous interpretation of the data obtained in vitro is complicated by the large variability of cellular lines and culture media. Over the last years, coarse-grained and multi-scale simulations have provided useful clues, but the complexity of the cellular membrane-NP system and the mesoscale size of the system pose difficult hurdles to theoretical routes [77].

In recent years, liposomes encapsulated with NPs have found enormous scopes in various biomedical fields such as drug design, transport, imaging, targeted delivery and therapy. These applications require a clear understanding about the interaction of NPs with cell membranes. Because of versatile organization, well-defined physicochemical properties and ability to mimic membrane scaffolding, they are widely studied as model membranes. The encapsulation of NPs in liposomes provides a biologically inspired route in designing therapeutic agents and as a means of reducing NPs toxicity. The hybrid lipid/ NPs conjugates have diverse biomedical applications including imaging of cancer cells, drug/gene delivery, targeted therapy, immunoassay, cell/protein separation, biosensing etc. Currently, little is known about the influence of NPs on physicochemical properties of lipid vesicles such as stability, elasticity, membrane fluidity and bilayer phase behavior. NPs are highly effective to penetrate the plasma membrane and to alter the natural processes within the cell. They serve as excellent carriers of therapeutic cargos through the membrane, likely due to internalization mechanisms like physical rupturing, membrane mediated transport, pore formation, etc. Recent studies on the effects of different metal NPs on membrane stability and/or deformation have revealed that the incorporation of metal NPs within membrane have altered the phase behavior of the lipids by decreasing the phase transition temperature and increasing fluidity of the bilayer. Since the polymorphic phase behavior of lipids influence different membrane related processes, it has become very important to study the effect of NPs interaction with different lipid membranes. In lipid vesicles, NPs encapsulation can be achieved by trapping the particles within the aqueous core or in the hydrophobic bilayer. To be embedded in the lipid bilayers, the NPs must possess two important features. They should be smaller in size to fit within a lipid bilayer and should have a hydrophobic surface (by coating with appropriate agents such as sterylamine). When the NPs are entrapped within bilayers, it can lead to changes in lipid packing and may disrupt lipid-lipid

interactions amongst the head groups and/or acyl tails. Disruption of such inter lipid interactions can result in changes in lipid bilayer phase behavior, which is related to the degree of lipid ordering and bilayer viscosity [78]. When some charged proteins or NPs are adsorbed onto cell surface, the membrane undergoes deformation and lipids in the constituent bilayers will be reorganized due to electrostatic interaction between the lipids and NPs /proteins. Since the membrane is negatively charged, positively charged NPs are attracted more towards the surface of cell-membrane and show higher levels of internalization when compared to uncharged and negatively charged particles. Hence, depending on their size and surface chemistry, embedded NPs may influence the stability and function of hybrid vesicles, domain formation, phase separation etc. Depending upon the size, electrostatic charge and hydrophobicity, the NPs interaction with lipid bilayer have three different possibilities. Three different possibilities of NPs interaction are shown in the Fig. 2.13.

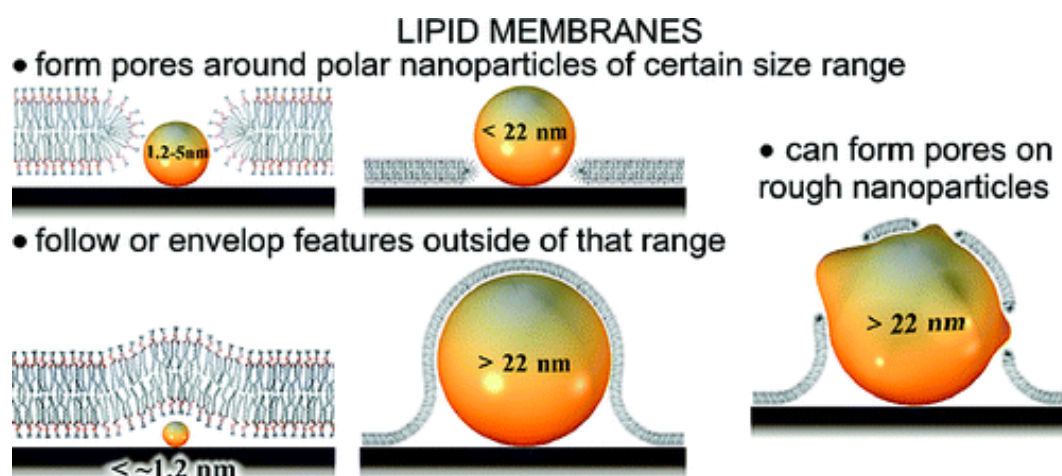


Fig. 2.13: Pore formation mechanism of NPs in lipid bilayer [77]

The first possibility indicates a structure in which a NPs is unable to ruptured the lipid bilayer as the size of the NPs is below the minimum critical size. The second possibility shows that the NPs are able to ruptured the lipid bilayer, if the size of NPs is belonging between 1.2 nm to 22 nm. The third mode depicts that the NPs get trapped at lipid bilayer as the size of NPs are greater than the maximum critical size, but if it contained rough surface than it may be rupture the lipid bilayer.

References

- [1] Max, B., "The use and meaning of nano in American English: Towards a systematic description," *Ampersand*, vol. 3, pp. 163-173, 2016.
- [2] Richard, P. F., "There's plenty of room at the bottom," *Appl. Magn. Reson.*, vol. 24, pp. 890-905, 1959.
- [3] Mansoori, G. A., Soelaiman, T. A. F., "Nanotechnology – an introduction for the standards community," *J. ASTM Int.*, vol. 2, pp. 428-448, 2005.
- [4] Roco, M.C., "The vision and action plan of the national nanotechnology initiative," *Nanotech.*, vol. 2, pp. 1-5, 2002.
- [5] Ruth, L., "Information resources in toxicology," *Adv. Mater.*, vol. 4, pp. 321-328, 2009.
- [6] Jaison, J., Ahmed, B., Yen, S. C., Alain, D., Michael, K. D., "Review on nanoparticles and nanostructured materials: history, sources, toxicity and regulations," *Beilstein J. Nanotechnol.*, vol. 9, pp. 1050–1074, 2018.
- [7] Khalid, M. A., Salman, A. A., Muhammad, N. K., Anees, A. A., "Nanomaterials as analytical tools for genosensors," *J. Sens. Sci. Technol.*, vol. 10, pp. 963-993, 2010.
- [8] Megan, E. M. Melissa, J. P., "Are nanoparticles potential male reproductive toxicants? A literature review," *Nanotoxicology*, vol. 1, pp. 204210, 2007.
- [9] Tarafdar, J. C., Shikha, S. Ramesh, R., "Nanotechnology: Interdisciplinary science of applications," *Afr. J. Biotechnol.*, vol. 12, pp. 219-226, 2013.
- [10] Emil, R., "Size matters: why nanomaterials are different," *Chem. Soc. Rev.*, vol. 35, pp. 583–592, 2006.
- [11] Andrew, M. S., Shuming, N., "Semiconductor nanocrystals: structure, properties, and band gap engineering," *J. Am. Chem. Soc.*, vol. 43, pp. 190-200, 2010.
- [12] Sagadevan, S., "Semiconductor nanomaterials, methods and applications: A review," *J. Nanosci. Nanotechnol.*, vol. 3, pp. 62-74, 2013.
- [13] Robert. P., Martina, T., "Designing drugs that overcome antibacterial resistance: where do we stand and what should we do?," *Expert Opin. Drug Discov.*, vol. 10, pp. 631-650, 2015.

- [14] Xi, Z., Aleksandar, F. R., Jun, W., Robert, L., Jinjun, S., "Nanomedicine in the management of microbial infection — Overview and perspectives," *Nano Today*, vol. 9, pp. 478–498, 2014.
- [15] Linlin, W., Chen, H., Longquan, S., "The antimicrobial activity of nanoparticles: present situation and prospects for the future," *Int. J. Nanomedicine*, vol. 12, pp. 1227–1249, 2017.
- [16] Jianlin, L. Qingliu, W., Ji, W., "Synthesis of nanoparticles via solvothermal and hydrothermal methods," *Nanomed. Nanotechnol.*, vol. 18, pp. 295-328, 2015.
- [17] Xuanli, W., Mingli, Q., Fei, F., Baorui, J., Haoyang, W., Xuanhui, Q., Alex, A. V., "Effect of glycine on one-step solution combustion synthesis of magnetite nanoparticles," *J. Alloys Compd.*, vol. 719, pp. 288-295, 2017.
- [18] Panagiotis, G., Stephan, S., Jerome, V., Vidyadhar, S., Mukhles, S., "Nanoparticle design by gas-phase synthesis," *Adv. Phys.*, vol. 1, pp. 81-100, 2015.
- [19] Hongab, R. Y., Pana, T. T., Li, H. Z., "Microwave synthesis of magnetic Fe₃O₄ nanoparticles used as a precursor of nanocomposites and ferrofluids," *J. Magn. Magn. Mater*, vol. 303, pp. 60-68, 2006.
- [20] Sara, S., Shirzad, Z., Shilpa, C. C., Venkateswara, K. R., "Preparation and characterization of magnetite nanoparticles by sol-gel method for water treatment," *Int. j. innov. res. sci. eng. technol.*, vol. 2, pp. 2969-2973, 2013.
- [21] Taebin, A., Jong, H. K., Hee, M. Y., Jeong, W. L., Jong, D. K., "Formation pathways of magnetite nanoparticles by coprecipitation method," *J. Phys. Chem. C*, vol. 116, pp. 6069–6076, 2012.
- [22] Alexander, S. M., Alexander, S. R., Aruna, S. T. R., "Combustion synthesis in nanostructured reactive systems," *Adv. Powder Technol.*, vol. 26, pp. 954-976, 2015.
- [23] Bolla, G. R., Deboshree, M., Benjaram, M .R., "Novel approaches for preparation of nanoparticles," *J. Nanostruct.*, vol. 19, pp. 1-36, 2017.
- [24] Ying, J. Z., Feng, C., "Microwave-assisted preparation of inorganic nanostructures in liquid phase," *Nano Lett.*, vol. 14, pp. 6462–6555, 2014.
- [25] Yujun, S., "Hot wire chemical vapor deposition chemistry in the gas phase and

- on the catalyst surface with organosilicon compounds," *Acc. Chem. Res.*, vol. 48, pp. 163–173, 2015.
- [26] Cristina, L., Sridhar, K., "Inorganic syntheses assisted by microwave heating," *Inorganics*, vol. 3, pp. 388-391, 2015.
- [27] Sarah, C. M., Sreejarani, K. P., Suprakas, S. R., Kalala, J., Rui, W. M. K., "Recent trends in the microwave-assisted synthesis of metal oxide nanoparticles supported on carbon nanotubes and their applications," *J. Nanomater.*, vol. 69, pp. 1-15, 2012.
- [28] Rafael, M., Yitzhak, M., Silvia, G., Katharina, L., "Colloidal systems for crystallization processes from liquid phase," *RSC Adv.*, vol. 15, pp. 2175–2191, 2013.
- [29] Jayanta, K. P., Kwang, H. B., "Green nanobiotechnology: Factors affecting synthesis and characterization techniques," *J. Nanomater.*, vol. 2014, pp. 1-12, 2014.
- [30] Shahwan, T.; Abu, S. S., Nairat, M., Boyacı, E., Eroglu, A. E., Scott, T.B., Hallam, K. R., "Green synthesis of iron nanoparticles and their application as a fenton-like catalyst for the degradation of aqueous cationic and anionic dyes," *Chem. Eng. J.*, vol. 172, pp. 258–266, 2011.
- [31] Pattanayak, M., Nayak, P.L., "Green synthesis and characterization of zero valent iron nanoparticles from the leaf extract of *Azadirachta indica* (neem)," *World J. Nano Sci. Technol.*, vol. 2, pp. 6–9, 2013.
- [32] Wang, Z., "Iron complex nanoparticles synthesized by eucalyptus leaves," *ACS Sustain. Chem. Eng.*, vol. 1, pp. 1551–1554, 2013.
- [33] Luo, F., Chen, Z., Megharaj, M., Naidu, R., "Biomolecules in grape leaf extract involved in one-step synthesis of iron-based nanoparticles," *RSC Adv.*, vol. 4, pp. 53467–53474, 2014.
- [34] Madhavi, V., Prasad, T. N., Reddy, A.V., Ravindra R. B., Madhavi, G., "Application of phyto-genic zerovalent iron nanoparticles in the adsorption of hexavalent chromium," *Spectrochim. Acta A*, vol. 16, pp. 17–25, 2013.
- [35] Senthil, M., Ramesh, C., "Biogenic synthesis of Fe₃O₄ nanoparticles using *Tridax procumbens* leaf extract and its antibacterial activity on *Pseudomonas aeruginosa*," *Dig. J. Nanomater. Biostruct*, vol. 7, pp. 1655–1660, 2012.

- [36] Rao, A., Bankar, A., Kumar, A. R., Gosavi, S., Zinjarde, S., "Removal of hexavalent chromium ions by *Yarrowia lipolytica* cells modified with phyto-inspired Fe//Fe₃O₄ nanoparticles," *J. Contam. Hydrol.* , vol. 146, pp. 63–73, 2013.
- [37] Njagi, E.C.; Huang, H.; Stafford, L., Genuino, H., Galindo, H. M., Collins, J. B., Hoag, G. E., Suib, S. L., "Biosynthesis of iron and silver nanoparticles at room temperature using aqueous Sorghum bran extracts," *Langmuir* , vol. 27, pp. 264–271, 2011.
- [38] Bharde, A. A., Parikh, R. Y., Baidakova, M., Jouen, S., Hannoyer, B., Enoki, T., Prasad, B., Shouche, Y.S., Ogale, S., Sastry, M., "Bacteria-mediated precursor-dependent biosynthesis of superparamagnetic iron oxide and iron sulfide nanoparticles," *Langmuir*, vol. 24, pp. 5787–5794, 2008.
- [39] Sundaram, P. A., Augustine, R., Kannan, M., "Extracellular biosynthesis of iron oxide nanoparticles by *Bacillus subtilis* strains isolated from rhizosphere soil," *Biotechnol. Bioprocess Eng.* , vol. 17, pp. 835–840, 2012.
- [40] Bharde, A., Rautaray, D., Bansal, V., Ahmad, A., Sarkar, I., Yusuf, S. M., Sanyal, M., Sastry, M., "Extracellular biosynthesis of magnetite using fungi," *Small* , vol. 2, pp. 135–141, 2006.
- [41] Pavani, K. V., Kumar, N. S. , "Adsorption of iron and synthesis of iron nanoparticles by *Aspergillus* species kvp 12," *Am. J. Nanomater.* , vol. 1, pp. 24–26, 2013.
- [42] Subramaniam, V., Subashchandrabose, S. R., Thavamani, P., Megharaj, M., Chen, Z., Naidu, R., "Chlorococcum sp. MM11—A novel phyco-nanofactory for the synthesis of iron nanoparticles," *J. Appl. Phycol.*, vol. 27, pp. 1861–1869, 2015.
- [43] Jitendra, M., Amla, B. Abhijeet, S., Madan, M. S., "Phytofabrication of nanoparticles through plant as nanofactories," *Adv. Nat. Sci.: Nanosci. Nanotechnol.*, vol. 5, pp. 1-11, 2014.
- [44] Lee, V. C., "The nanomedicine revolution," *Pharm. Ther.*, vol. 37, pp. 512-517, 2012.
- [45] Jun, H., Leping, Y., Wenjun, Y., Wentao, F., Yu, W., Xiongying, M., Li, X., "Combination of fluorescence-guided surgery with photodynamic therapy for the

- treatment of cancer," *Mol. Imaging.*, vol. 16, pp. 1-15, 2017.
- [46] Buermans, H.P.J., Dunnen, J. T., "Next generation sequencing technology: Advances and applications," *Biochim. Biophys. Acta.*, vol. 1842, pp. 1932–1941, 2014.
- [47] Rajesh, S., James, W. L., "Nanoparticle-based targeted drug delivery," *Exp. Mol. Pathol.* , vol. 86, pp. 215–223, 209.
- [48] Sheetal, J., Pramod, K. S., Rishabha, M., "Hyperthermia: role and risk factor for cancer treatment," *Achiev. Life Sci.*, vol. 10, pp. 161–167, 2016.
- [49] Anthony, S., Lang, T., Robert, A., Kenneth, D., "Nanoparticles, human health hazard and regulation," *J. R. Soc. Interface*, vol. 7, pp. 119-129, 210.
- [50] Sadik, O. A., Zhou, A. L., Kikandi, S., Du, N., Wanga, Q., Varnerb, K., "Sensors as tools for quantitation, nanotoxicity and nanomonitoring assessment of engineered nanomaterials," *J. Environ. Monit.*, vol. 11, pp. 1782–1800, 2009.
- [51] Slavica, S., Sneha, S., Francia, H., Jasmina, V., "Pure and multi metal oxide nanoparticles: synthesis, antibacterial and cytotoxic properties," *J. Nanobiotechnology*, vol. 14, pp. 1-20, 2016.
- [52] George, H. C., Jing, Z., George, C. S., Richard, P. V. D., "Localized surface plasmon resonance spectroscopy of triangular aluminum nanoparticles," *J. Phys. Chem.* , vol. 112, pp. 13958–13963, 2008.
- [53] Wei, W., Zhaohui, W., Taekyung, Y., Changzhong, J., Woo, S. K., "Recent progress on magnetic iron oxide nanoparticles: synthesis, surface functional strategies and biomedical applications," *Sci. Technol. Adv. Mater.*, vol. 16, pp. 1-43, 2016.
- [54] Apostolov, A. T., Apostolova, I. N., Wesselinowa, J. M., "MO.Fe₂O₃ nanoparticles for self-controlled magnetic hyperthermia," *J. Appl. Phys.*, vol. 109, pp. 1-8, 2011.
- [55] Nguyen, V. L., Yong, Y., Toshiharu, T., Cao, M. T., Yanqin, C., Masayuki, N., "Related magnetic properties of CoFe₂O₄ cobalt ferrite particles synthesised by the polyol method with NaBH₄ and heat treatment: new micro and nanoscale structures," *R. Soc. Chem.*, vol. 5, pp. 56560–56569, 2015.
- [56] Tong, G., Zhi, C., Qiaoli, H., Feng, N., Xiani, H., Laishun, Q., Yuexiang, H., "A

- review: Preparation of bismuth ferrite nanoparticles and its applications in visible-light induced photocatalyses," *Rev. Adv. Mater. Sci.*, vol. 40, pp. 97-109, 2015.
- [57] Vladimir, S. Z., Dmitry, S. F., Igor, A. P., Richard, J. G., Benjamin, C., "Physical and chemical properties of magnetite and magnetite-polymer nanoparticles and their colloidal dispersions," *J. Colloid Interface Sci.*, vol. 212, pp. 49–57, 1999.
- [58] Alejandro, G. R., Jose, F. M., Maria, P. M., Carlos, J. S., "Effect of nature and particle size on properties of uniform magnetite and maghemite nanoparticles," *J. Phys. Chem. C*, vol. 111, pp. 18577-18584, 2007.
- [59] Junghyun, N., Osman, I. O., Saadullah, G. A., Paul, W., Jean, L. B., "Magnetite Fe₃O₄ (111) surfaces: impact of defects on 2 structure, stability, and electronic properties," *Chem. Mater.*, vol. 27, pp. 5856-5867, 2015.
- [60] Larry, W. F., Robert, M. H., Anne, M. H., "High-Pressure crystal chemistry of spinel (MgAl₂O₄) and magnetite (Fe₃O₄): Comparisons with silicate spinels," *Phys. Chem. Miner.*, vol. 13, pp. 215–220, 1986.
- [61] Rolf, E. H., "Magnetic phenomena and their interpretation—classical approach," *J. Magn. Magn. Mater.*, vol. 15, pp. 312-337, 2001.
- [62] Allenspach, R., "Ultrathin films: magnetism on the microscopic scale," *J. Magn. Magn. Mater.*, vol. 129, pp. 160-185, 1994.
- [63] Roger, S. M. R., Roeland, J. M. N., Jan, C. M., Jan, C. M. H., Daniela, A. W., Peter, C. M. C., "Manipulation of micro- and nanostructure motion with magnetic fields," *R. Soc. Chem.*, vol. 10, pp. 1295–1308, 2014.
- [64] Arati, G. K., Andrew, C. J., Dmitri, L., Richard, C. W., and Randall, L. T., "Tuning the magnetic properties of nanoparticles," *Int. J. Mol. Sci.*, vol. 14, pp. 15977-16009, 2013.
- [65] Waiz, K., Armin, K., Urs, H., Ana, B., Jens, G., Jeroen, A. B., Yasin, E., "Size-dependent redox behavior of iron observed by in-situ single nanoparticle spectro-microscopy on well-defined model systems," *Sci. Rep.*, vol. 6, pp. 1-8, 2016.
- [66] Gudoshnikov, S. A., Liubimov, B. Y., Usov, N. A., "Hysteresis losses in a dense superparamagnetic nanoparticle assembly," *J. Appl. Phys.*, vol. 2, pp. 1-7, 2012.
- [67] Stuart, R. B., Keith, S. M., "Structure and magnetism of coordination polymers

- containing dicyanamide and tricyanomethanide," *Coord. Chem. Rev.*, vol. 246, pp. 103-130, 2003.
- [68] Kneller, E. F., Luborsky, F. E., "Particle size dependence of coercivity and remanence of single domain particles," *J. Appl. Phys.*, vol. 34, pp. 656-658, 1963.
- [69] Robert, F. B., Subir, K. B., "Theoretical single-domain grain size range in magnetite and titanomagnetit," *J. Geophys. Res.*, vol. 80, pp. 4049 - 4058, 1975.
- [70] Yong, Z., Nathan, K., Miqin, Z., "Surface modification of superparamagnetic magnetite nanoparticles and their intracellular uptake," *Biomater. Sci.*, vol. 23, pp. 1553–1561, 2002.
- [71] Suh, C. P., Suk, F. C., Marc, A. A., "Redox equilibria of iron oxides in aqueous-based magnetite dispersions: Effect of pH and redox potential," *J. Colloid Interface Sci.*, vol. 311, pp. 94–101, 2007.
- [72] Fred C. T., "Mechanisms of antimicrobial resistance in bacteria," *Am. J. Infect. Control*, vol. 34, pp. 3-10, 2006.
- [73] Thomas, F. O., "Resistance of bacteria to antibacterial agents: report of task force 2," *Rev. Infect. Dis.*, vol. 9, pp. 244-260, 1987.
- [74] Andrew, G. M., Nicholas, W., Fazmin, N., Austin, Y., "The Comprehensive Antibiotic Resistance Database," *Antimicrob. Agents Chemother.*, vol. 57, pp. 3348 –3357, 2013.
- [75] Kagan, B. L., Selsted, M. E., Ganz, T., Lehrer, R. I., "Antimicrobial defensin peptides form voltage-dependent ion-permeable channels in planar lipid bilayer membranes," *Proc. Natl. Acad. Sci.*, vol. 87, pp. 210-214, 1990.
- [76] Mark, S. B., "Membrane structure: some general principles," *Science*, vol. 181, pp. 622-629, 1973.
- [77] Costanza, M., Daniele, M., Ivano, A., Paolo, B., Debora, B., "Interaction of nanoparticles with lipid membranes: a multiscale perspective," *Nanoscale*, vol. 6, pp. 6452–6457, 2014.
- [78] Geoffrey, D. B., "Hydrophobic silver nanoparticles trapped in lipid bilayers: Size distribution, bilayer phase behavior, and optical properties," *J. Nanobiotechnology*, vol. 6, pp. 1-10, 2008.

CHAPTER 3

EXPERIMENTAL TECHNIQUES

3.1 GC-MS analysis

GC-MS instrument separates chemical mixtures (the GC component) and identifies the components at a molecular level (the MS component). It is one of the most accurate tools for analyzing leaf extract samples. The GC works on the principle that a mixture will separate into individual substances when heated. The heated gases are carried through a column with an inert gas (such as helium). As the separated substances emerge from the column opening, they flow into the MS. MS identifies compounds by the mass of the analytic molecule. A library of known mass spectra, covering several thousand compounds, is stored on a computer. MS is considered the only definitive analytical detector [1]. Fig 3.1 shows a pictorial view of GC-MS instrument setup.



Fig. 3.1: GC-MS setup

3.1.1 Principle of GC-MS

GC-MS is used to analyze complex organic and biochemical mixtures [2]. The GC-MS instrument consists of two main components. The gas chromatography portion separates different compounds in the sample into pulses of pure chemicals based on their volatility [3] by flowing an inert gas (mobile phase), which carries the sample, through a stationary phase fixed in the column [2]. Spectra of compounds are collected as they exit a chromatographic column by the mass spectrometer, which identifies and quantifies the chemicals according to their mass-to-charge ratio (m/z). These spectra can then be stored on the computer and analyzed (Oregon State University, 2012). The schematic diagram of GC-MS is shown in fig. 3.2.

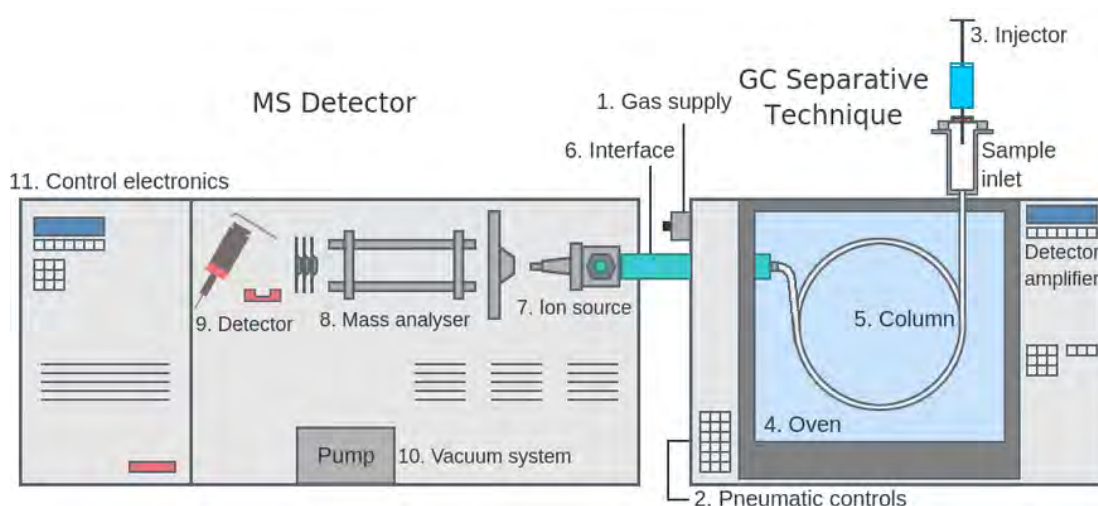


Fig. 3.2: Schematic diagram of GC-MS

3.2 XRD analysis

X-rays are electromagnetic radiation of exactly the same nature as light but of very much shorter wavelength. X-ray used in diffraction have wavelengths lying approximately in the range 0.5 to 2.5 Å, whereas the wavelength of visible light is of the order of 6000 Å ($1 \text{ Å} = 10^{-10} \text{ m}$). X-ray therefore occupies the region between gamma and ultraviolet rays in the complete electromagnetic spectrum as shown in Fig. 3.3. All X-ray tubes contain two electrodes, an anode (the metal target) maintained, few exceptions, at ground potential, and a cathode maintained at a high negative potential, normally of the order of 30 to 50 kV for diffraction work.

X-ray tubes may be divided into two basic types, according to the way in which sections are produced by the ionization of small quantity of gas (residual) air in a partly evacuated tube and filament tubes, in which the source of the electrons is a hot filament [4].

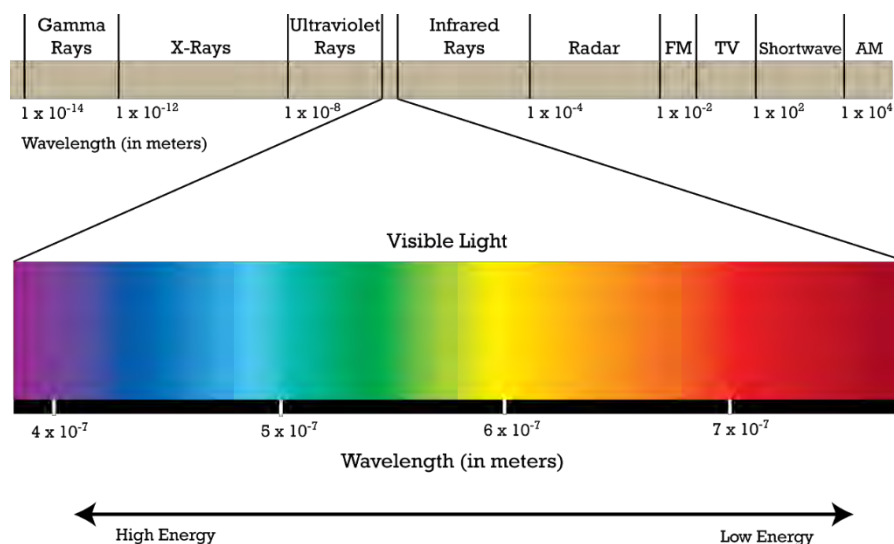


Fig. 3.3: Electromagnetic spectrum

In the present case, sample was kept fixed and X-ray tube and detector were moved to the θ and 2θ ranges, respectively. Instead of the film, digital data was recovered for the whole 2θ range. After the pattern is obtained the value of 2θ is calculated for each diffraction line; set of 2θ values is the raw data for the determination of the lattice parameters of the unit cell.

A PHILIPS PW 3040 X'Pert PRO X-ray diffractometer was used for the lattice parameter determination shown in Fig. 3.4.

The X'Pert PRO XRD system contains the following parts:

- i. "Cu-Tube" with maximum input power of 60 kV and 55 mA.
- ii. "Ni-Filter" to remove the $\text{CuK}\alpha$ component.
- iii. "Programmable Divergent Slit" to reduce divergence of beam and control irradiated beam area.
- iv. "Mask" to get desired beam area.
- v. "Sample holder" for powder sample.
- vi. "Anti-Scatter Slit" to reduce air scattering background.
- vii. "Programmable Receiving slit" to control the diffracted beam intensity.

- viii. “Solar Slit” to stop scattered beam and pass parallel diffracted beam.



Fig. 3.4: A PHILIPS PW 3040 X'Pert Pro X-ray diffractometer

X-ray Diffractometer was used to study the crystalline phases of the prepared samples. The powder diffraction technique was used with a primary beam power of 40 kV and 30 mA for Cu radiation. A nickel filter was used to reduce CuK_β radiation and finally Cu-K_α radiation was only used as the primary beam. A 2θ scan was taken from 10 to 70° to get possible fundamental peaks with the sampling pitch of 0.02° and time for each step data collection was 1.0 s. After that data of the samples were analyzed by computer software. A schematic diagram of X-ray is shown in Fig. 3.5.

The aim of the present study was to determine the crystallite size of Fe_3O_4 NPs. The crystallite size of the prepared samples was determined from the strongest peak of each XRD patterns using Debye-Scherrer's formula [5, 6].

$$D = \frac{0.9 \lambda}{\beta \cos \theta} \dots\dots\dots (3.1)$$

where D is the average crystallite size, λ is the wavelength of the radiation used as the primary beam of Cu-K α ($\lambda = 1.54178 \text{ \AA}$), θ is the angle of incident in degree and β is the full width at half maximum (FWHM) of the strongest reflection in radian which was determined experimentally after correction of instrumental broadening.

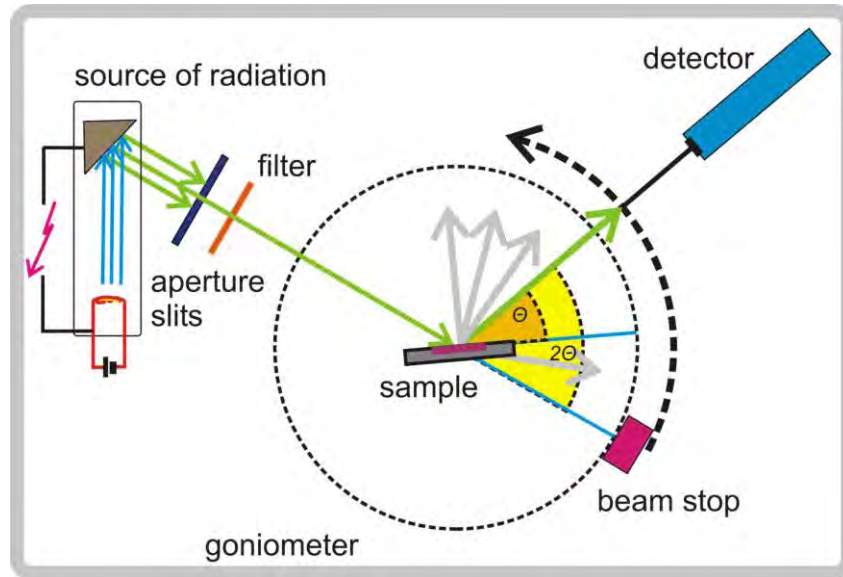


Fig. 3.5: Schematic diagram of X-ray

The dislocation density and microstrain of the prepared samples were determined using the following formula.

$$\delta = \frac{1}{D^2} \dots\dots\dots (3.2)$$

$$\varepsilon = \frac{\beta \cos \theta}{4} \dots\dots\dots (3.3)$$

The peaks in an XRD pattern are directly related to the atomic distance [7]. The atoms represented as block spheres in the figure, can be viewed as forming different sets of planes in the crystal. Fig. 3.6 shows the Bragg's diffraction patterned of X-ray.

For a given set of lattice plane with an inter planner distance of d , the condition for a diffraction to occur can simply written as

$$2d_{nlk} = n\lambda \dots\dots\dots (3.2)$$

This is known as Bragg's law, where, λ is the wavelength of the X-ray, θ is the scattering angle and n is an integer representing the order of the diffraction.

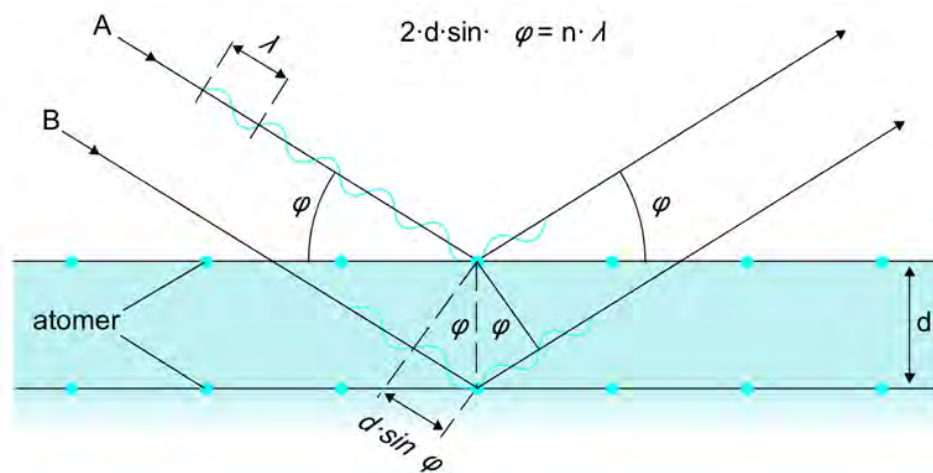


Fig. 3.6: Bragg's diffraction pattern

3.3 EDX analysis

EDX spectroscopy is an analytical tool predominantly used for chemical characterization. Being a type of spectroscopy, it relies on the investigation of a sample through interactions between light and matter, analyzing X-rays in this particular case. High energy electron beams (in an SEM or TEM) strike the material to be analyzed, and X-rays are emitted. These X-rays can be detected by a Si Li detector, calibrated with respect to cobalt metal emission (6.925 keV), and then used to identify and analyze the elemental composition of the specimen surface. Its characterization capabilities are due in large part to the fundamental principle that each element of the Periodic Table has a unique electronic structure and, thus, a unique response to electromagnetic waves [8].

Essentially, an X-ray photon hits a diode in the detector producing a charge that is converted into a positive voltage pulse via a field effect transistor. The pulse is subsequently converted by an analogue to digital converter, into a numerical value relative to the X-ray's incoming energy. The signal is then assigned to a particular energy channel and registered as a single count. Counts are compiled to produce an energy dispersive spectrum. The various emission lines associated with X-rays emitted from an atom are named after the shell of the initial vacancy, i.e. K, L, M, etc. A Greek letter subscript is used to indicate the shell of the electron that fills the gap.

For example, K_{α} radiation refers to radiation resulting from a vacancy in the K shell being filled by an electron from the next highest shell. K_{β} denotes a K-shell vacancy filled by an electron from two shells above. There are some basic rules that apply for the order and energy of the X-rays:

- i. For a given element, the lower line series has a higher energy, i.e., the energies of the K lines are greater than those of the L lines.
- ii. Within a line series, the higher atomic number elements emit higher energy X-rays. i.e., the oxygen K lines are higher in energy than carbon K lines.
- iii. The lower line series have simpler structures than the high line series, i.e., the K lines are simple, whilst the L and M lines get more complex and overlapping starts to occur.

Spectra can be acquired over short time-periods and be displayed almost simultaneously, providing a near instant visual representation of the chemical analysis. Qualitative analysis determines what elements are present in a sample by identification of the peaks in the spectrum, whilst quantitative analysis is used to derive the relative abundance of the elements from their corresponding peak intensities, either compared to other elements present in the spectrum or to standards.

For EDX, as a general rule of thumb, elements of $Z > 11$ can be analyzed if they are in a concentration of greater than 5 weights% with an accuracy of around $\pm 3\%$ if there are no significant peak overlaps. The analyst needs to think carefully about the sample (i.e., topography, porosity, etc), the lateral and depth resolution of the X-ray emission in relation to the sample microstructure, and the quoted accuracy of any computer-generated results, before regarding EDX as a completely reliable black-box technique [9]. In this study, EDX analysis was used mainly to determine the bulk composition of the sample materials. In an SEM, a fixed accelerating voltage of 20 kV was used in order to obtain high signal intensity.

3.4 FT-IR analysis

FT-IR spectroscopy is a technique based on the vibrations of the atoms within a molecule. An infrared spectrum is obtained by passing IR radiation through a sample and determining what fraction of the incident radiation is absorbed at a particular energy. The energy at which any peak in an absorption spectrum appears corresponds to the frequency of a vibration of a part of a sample molecule [10]. Moreover,

chemical bonds in different environments will absorb varying intensities and at varying frequencies. Thus, IR spectroscopy involves collecting absorption information and analyzing it in the form of a spectrum: The frequencies at which there are absorptions of IR radiation ('peaks' or 'signals') can be correlated directly to bonds within the compound in question. Each inter-atomic bond may vibrate in several different motions (stretching or bending), individual bonds may absorb at more than one IR frequency. Stretching absorptions usually produce stronger peaks than bending; however, the weaker bending absorptions can be useful in differentiating similar types of bonds (e.g., aromatic substitution).

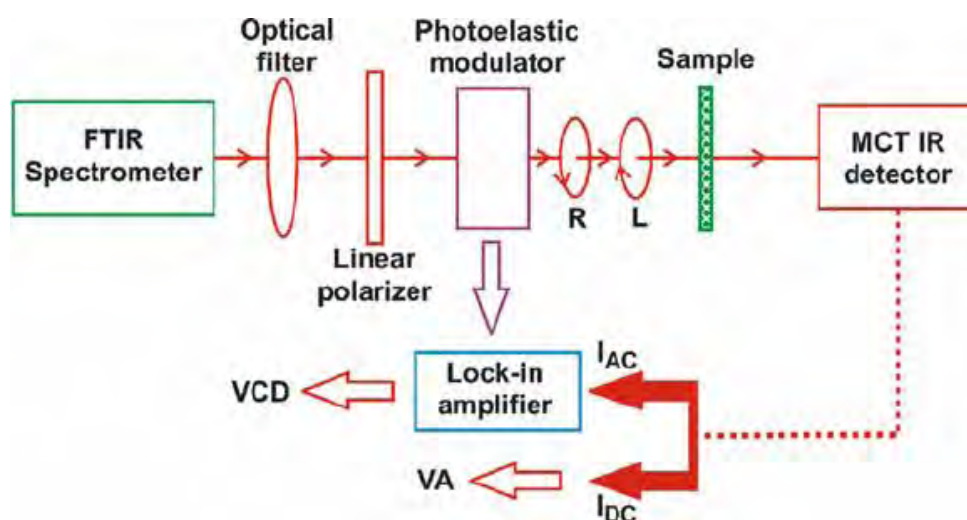


Fig. 3.7: Schematic illustration of an FT-IR system

The basic components of an FT-IR spectrometer are shown schematically in Fig. 3.7. The radiation emerging from the source is passed to the sample through a techniques interferometer before reaching a detector. Upon amplification of the signal, in which high-frequency contributions have been eliminated by a filter, the data are converted to a digital form by an analogue-to-digital converter and then transferred to the computer for Fourier transformation to be carried out [2].

One of the great advantages of infrared spectroscopy is that virtually any sample in nearly any state can be studied. Liquids, solutions, pastes, powders, films, fibers, gases and surfaces can all be examined by a judicious choice of sampling technique [11]. The photo image of the instrument is shown in Fig. 3.8. The FT-IR sample handling is to grind finely a quantity of the sample with a specially purified salt (usually potassium bromide) to remove scattering effects from large crystals. This

powder mixture is then crushed in a mechanical die press to form a translucent pellet through which the beam of the spectrometer can pass.



Fig. 3.8: A Photo of Jasco FT-IR 6300 machine

3.5 FESEM analysis

Electron microscopes were developed in the 1930s to overcome the limitations of optical microscopy and provide increased magnification and resolution, far superior to optical systems. The first commercialized FESEM was built by Cambridge Instruments [12]. SEM is a powerful tool for examining and interpreting microstructures of materials and is widely used in the field of material science. The principle of SEM is based on the interaction of an incident electron beam and the solid specimen [13]. Electron bombardment can produce a wide variety of emissions from the specimen, including backscattered electrons, secondary electrons, Auger electrons, X-rays, visible photons and so on.

- i. Secondary Electrons: If an incident electron collides with an electron in a sample atom, it will knock the electron out of its orbital shell and the atom will become ionized. Because the incident electron loses little energy during each collision, multiple collisions are possible, continuing until the incident electron no longer has the energy to dislodge secondary electrons. Each freed secondary electron has a very small kinetic energy (<50 eV), which is independent of the incident electron energy. If generated close enough to the

sample surface (<10 nm), these secondary electrons can escape to be collected by the detector. As a direct result, secondary electron imaging is closely related to sample topography.

- ii. **Backscattered Electrons:** If an incident electron collides with the nucleus of surface atom, the electron will bounce or scatter ‘backward’ out of the sample as a backscattered electron (BSE). These electrons have high energies, typically between 50eV and that of the original incident electron. The production of backscattered electrons varies directly with atomic number, and thus backscattered electron images can be used to discern differences in sample atomic number.
- iii. **Auger Electrons:** As a result of secondary electron generation, a vacancy is left in an ionized atom’s electron shell. To fill this vacancy, an electron from a higher energy outer shell (from the same atom) can drop down to fill the vacancy. This creates an energy surplus in the atom that can be corrected by emitting an outer electron, an Auger electron. Auger electrons have a characteristic energy unique to the element from which they are emitted and can be used to give compositional information about the target sample. Auger electrons have a relatively low kinetic energy and are only emitted from shallow sample depths (<3 nm).

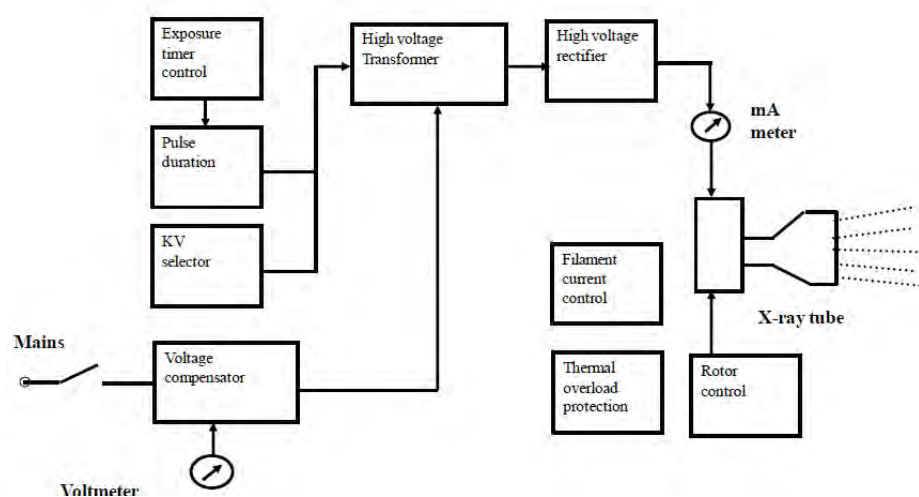


Fig. 3.9: Schematic diagram of FESEM

- iv. **Characteristic X- rays:** X-rays are also produced by interactions of the incident electron beam with a sample surface. Similar to the Auger electron generating process, the excess energy produced by reshuffling electrons to fill shell

vacancies can also be emitted in the form of an X-ray rather than an Auger electron. X-rays have a characteristic energy unique to the element from which they originate and so provide compositional information about a sample. Secondary electron imaging and X-ray analysis were the primary functions used for SEM sample characterization in this study.

A FESEM consists of three distinct parts: an electron column; a detection system; and a viewing system. Fig. 3.9 shows a schematic of a simple scanning electron microscope. Two electron beams are controlled simultaneously by the same scan generator: one is the incident electron beam; the other is for the cathode ray tube (CRT) screen. The incident beam is scanned across the sample, line by line, and the signal from the resulting secondary electrons is collected, detected, amplified and used to control the intensity of the second electron beam. Thus, a map of intensity of secondary electron emission from the scanned area of the sample will be shown on the CRT screen as variations in brightness, reflecting the surface morphologies of the specimen. Given this mechanism, the magnification of the SEM image can be adjusted simply by changing the dimensions of the area scanned on the sample surface [3].

The spatial resolution of the SEM is strongly dependent on diameter (spot size) of the electron probe beam at the specimen surface. In a SEM system, the diameter of the incident electron beam is demagnetized using two or more electron lenses before it reaches the sample surface. At the same time, the effective diameter of the electron source is a key factor in determining the resolution of the SEM. There are two basic types of electron guns in current use: thermionic electron gun and field emission electron gun. The diameters of the electron beam originating from these gun types are about 20-50 μm and 10 nm, respectively. Thus, field emission SEM (FESEM) is the electron source of choice for high -resolution SEM images [14].

The FESEM systems employed in this work is field emission scanning electron microscopy. Fig.3.10 shows a photo of the JSM-7600F (FE-SEM, Tokyo, Japan) system.



Fig. 3.10: A Photo of FESEM JSM-7600F

3.6 TEM analysis

The maximum resolution achievable on an imaging device (e.g. a microscope) is limited by the wavelength of the electromagnetic radiation employed. In microscopes, the Abbe equation ($d = \lambda/2n \sin\theta$) links the minimum distance observable to the wavelength through the numerical aperture of a lens, which is often close to 1, causing the resolution to be around half of the wavelength [15]. For typical light microscopes this diffraction limit to the achievable resolution is at best 200 nm. For the analysis of nanoscale structures, Knoll and Ruska were the first to utilize the wave-like properties of electrons to construct what is now known as a TEM.

With the wavelength of electrons typically being around 1-10 pm, depending on the operating power of the microscope, theoretically the resolution of TEM is on a sub atomic scale. However, in reality the best resolution obtained to date is around 0.1 nm, mostly due to physical defects and aberrations within the lenses [16]. Briefly, in a TEM a beam of electrons is created at the emission source, which may be composed of tungsten or lanthanum hexaboride (LaB₆). The beam then passes through an anode in order to accelerate the electrons which then continue on through the condenser lens in order to focus the beam through an ultrathin sample (< 100 nm thick).

The beam then passes through the objective and intermediate lenses which refocus the beam once it has interacted with the sample. Finally, the beam passes through the projector lens which expands the beam onto either a photographic plate or, more

commonly nowadays, on to a charge coupled device (CCD) camera allowing real time observation of the sample as shown in Fig. 3.11. The image is created by the scattering of the electron beam as it passes through a sample, therefore denser areas would provide lower electron transmittance.

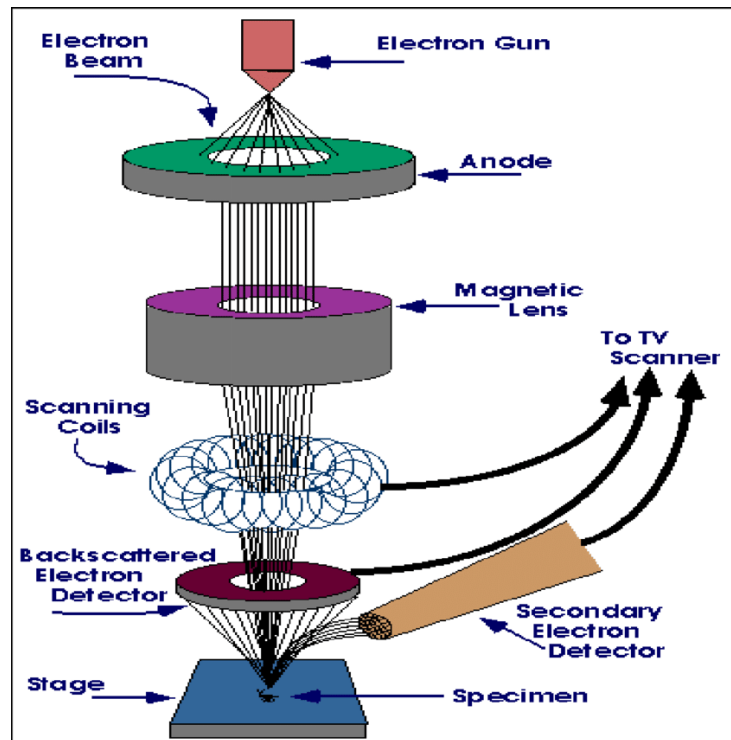


Fig. 3.11: Schematic representation of TEM

This technique has been traditionally used to image materials with significant scattering also in thin samples, i.e. materials such as metals or ceramics characterized by a high density of ‘opaque’ atoms (= with a high number of electrons). However, now also biological samples can be imaged through the use of appropriate contrast agents and the fixation of the material; even more advanced is the use of the low temperature cryo-TEM where the sample is frozen (avoiding artifacts due to the evaporation of water) and vitreous ice acts as a contrast agent in the sample [17]. As well as determining the morphology of nanoconstructs TEM can also be used as an analytical tool for determining the composition and morphology of the materials being studied. The scattering of the electrons in TEM can also allow the identification of the crystalline phase of specific materials in the sample, since as seen for X-rays also electrons scatter elastically creating secondary waves which can interfere either constructively or destructively. In a crystalline sample the scattering can therefore

produce a diffraction pattern which can be mapped to calculate the crystal planes shows a high resolution TEM image of NPs. For example, a TEM image of Fe_3O_4 NPs is shown in Fig. 3.12. When electrons scatter off a material they can do so either elastically or in elastically, depending on whether they preserve or degrade their initial energy. The energy loss is generally caused by the ionization of the atoms the electrons come into contact with and, as the ionization energy of each element is unique, it is possible to map the atomic composition of a sample through what is commonly referred to as electron energy loss spectroscopy.

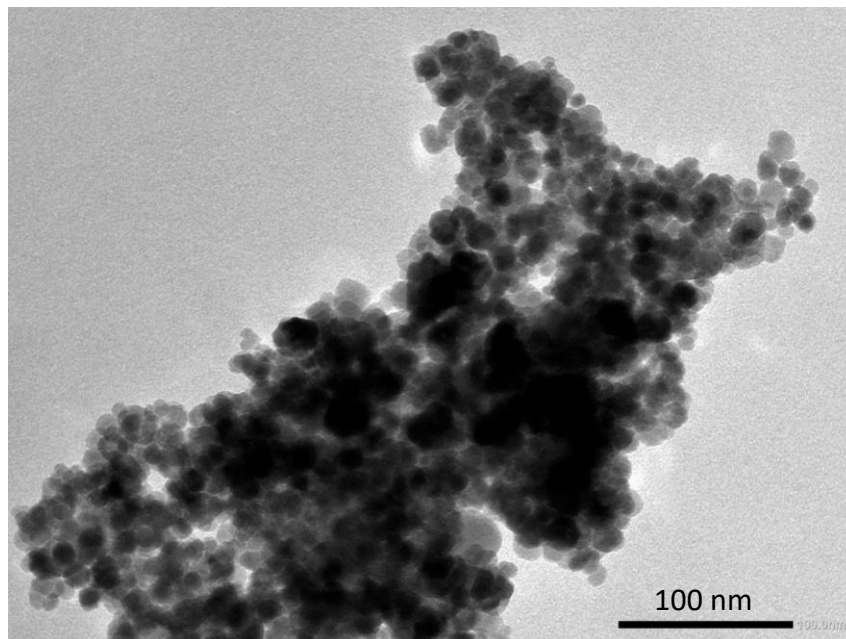


Fig. 3.12: TEM image of Fe_3O_4 NPs

When TEM is used for organic or biological samples there is one main drawback. Due to the use of electrons as the source of electromagnetic radiation, the TEM chamber must be under a very high vacuum; this is due to the fact that any gas molecules in the chamber will interact and scatter the electrons before reaching the sample thus knocking them out of alignment which will result in a major decrease in focusing and resolution capabilities. For inorganic materials the need to be under high vacuum is not a great problem as structure changes during preparation will be kept to a minimum [18].

3.7 DSC analysis

DSC is a technique in which the difference in the amount of heat required to increase the temperature of a sample and reference are measured as a function of temperature. In the present study, the instrument had a temperature scanning range from room temperature to $\sim 800^{\circ}\text{C}$. The sample was put in a Pt pan and placed on a Pt holder. An empty pan was placed in the other Pt holder for a reference. The sample pans were designed to have very high thermal conductivity. In the present investigation the amount of each sample was 10 mg. Fig. 3.13 shows a schematic diagram of a DSC system. The instrument cells are often airtight to shield the sample and reference from external thermal perturbations. This also allows experiments to be performed under variable pressures and atmospheres [19].

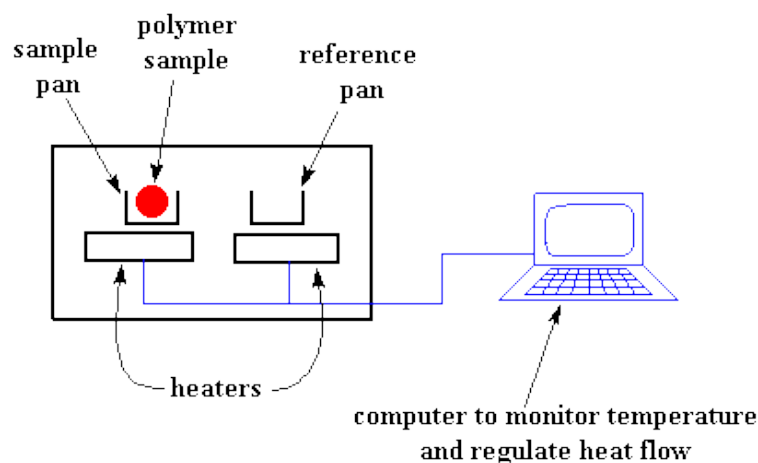


Fig. 3.13: Schematic diagram of DSC

The whole system was purged with high purity Ar gas to minimize sample oxidation. The heating rate for non-isothermal scans was 10 K/min. The temperature and enthalpy were calibrated using pure In and Zn standards. In isothermal mode, the temperature of the reference and the sample was raised to the pre-setting temperature and kept isothermally. In our experiment non-isothermal DSC were used to study the phase transformation kinetics. Whether more or less heat must flow to the sample depends on whether the process is exothermic or endothermic. For example, as a solid sample melts to a liquid it will require more heat flowing to the sample to increase its temperature at the same rate as the reference. This is due to the absorption of heat by the sample as it undergoes the endothermic phase transition from solid to liquid. By observing the difference in heat flow between the sample and reference, differential

scanning calorimeters are able to measure the amount of heat absorbed or released during such transitions. DSC may also be used to observe more subtle phase changes. DSC is widely used in industrial settings as a quality control instrument due to its applicability in evaluating sample purity and for studying polymer curing.

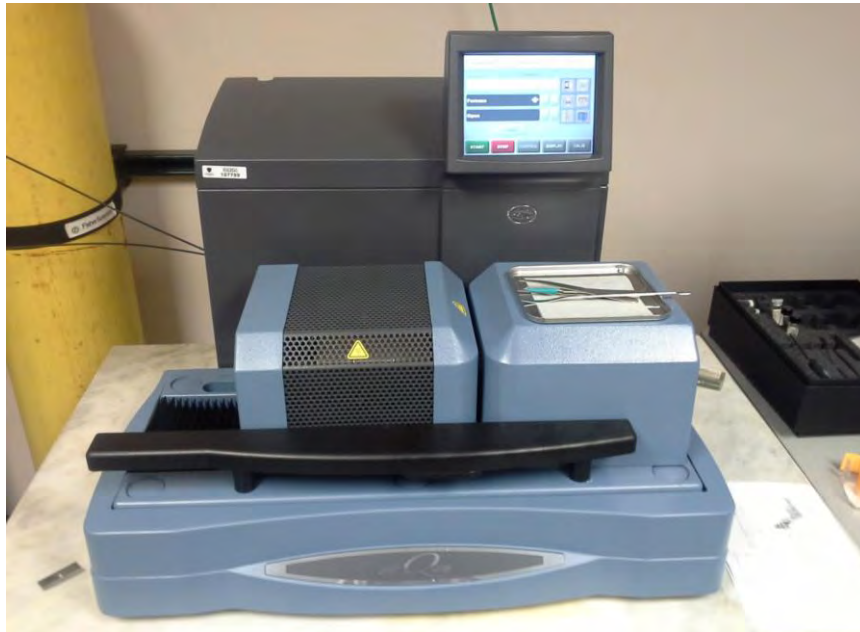


Fig. 3.14: DSC & TGA analyzer (TA instrument, SDT Q-600)

A typical differential scanning calorimeter consists of two sealed pans: a sample pan and a reference pan which is generally an empty sample pan. These pans are often covered by or composed of aluminum, which acts as a radiation shield. The two pans are heated, or cooled, uniformly while the heat flow difference between the two is monitored. This can be done at a constant temperature but is more commonly done by changing the temperature at a constant rate, a mode of operation also called temperature scanning. Fig.3.14 shows a pictorial view of a DSC setup of thermal analysis, SDT Q-600. During the determination, the instrument detects differences in the heat flow between the sample and reference. This information is sent to an output device, most often a computer, resulting in a plot of the differential heat flow between the reference and sample cell as a function of temperature. When there are no thermodynamic physical or chemical processes occurring, the heat flow difference between the sample and reference varies only slightly with temperature and shows up as a flat or very shallow base line on the plot. However, an exothermic or endothermic process within the sample results in a significant deviation in the

difference between the two heat flows. The result is a peak in the DSC curve. Generally, the differential heat flow is calculated by subtracting the sample heat flow from the reference heat flow. When following this convention, exothermic processes will show up as positive peaks above the baseline while peaks resulting from endothermic processes are negative below the baseline. The result of a DSC experiment is a heating or cooling curve. This curve can be used to calculate enthalpies of transitions. This is done by integrating the peak corresponding to a given transition. It can be shown that the enthalpy of transition can be expressed $\Delta H = KA$, where, ΔH is the enthalpy of transition, K is the calorimetric constant, and A is the area under the curve. The calorimetric constant vary instrument to instrument and can be determined by analyzing a well-characterized sample with known enthalpies of transition [20]. An arbitrary DSC thermo gram is displayed in Fig.3.15 showing various transformations. As the temperature increases, an amorphous solid will become less viscous. At some point the molecules may obtain enough freedom of motion to spontaneously arrange themselves into a crystalline form. This is known as the crystallization temperature.

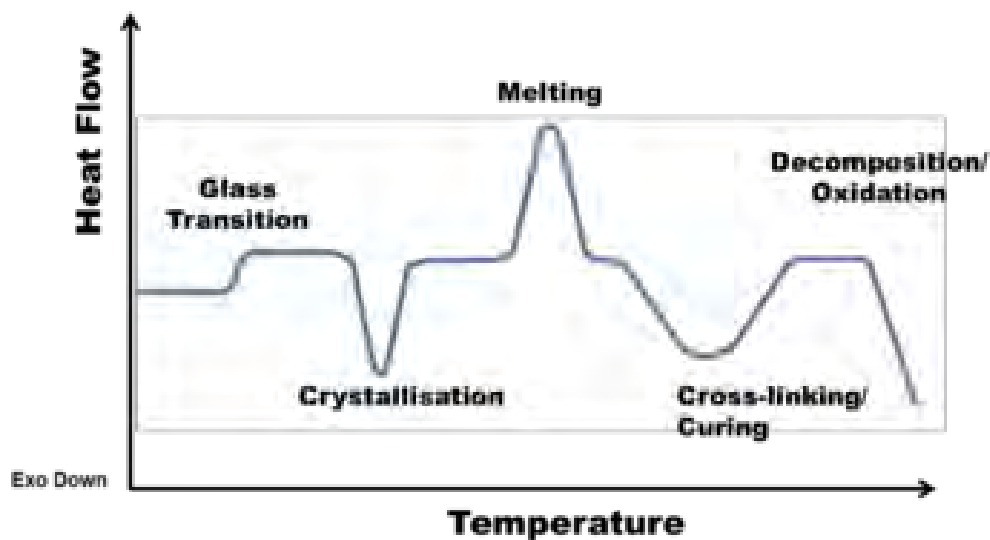


Fig. 3.15: Heat flow as a function of DSC curve

This transition from amorphous solid to crystalline solid is an exothermic process, and results in a peak in the DSC signal. As the temperature increases the sample eventually reaches its melting temperature (T_m). The melting process results in an endothermic peak in the DSC curve. The ability to determine transition temperatures

and enthalpies makes DSC an invaluable tool in producing phase diagrams for various chemical systems [16].

3.8 TGA analysis

TGA is a technique in which the mass of the sample is measured against time or temperature while the temperature is changed under a certain atmosphere. This method is used for the determination of sample purity, water content, carbonate or organic content present in it and also for studying decomposition reactions. The graph of the resultant change in mass with respect to temperature is called a thermo gravimetric curve [21]. An arbitrary TGA thermo gram is displayed in Fig.3.16 showing the change in sample mass with the increase in temperature. In the figure each slope corresponds to a weight loss produced by the evaporation of one or more compounds of the analyzed mixture.

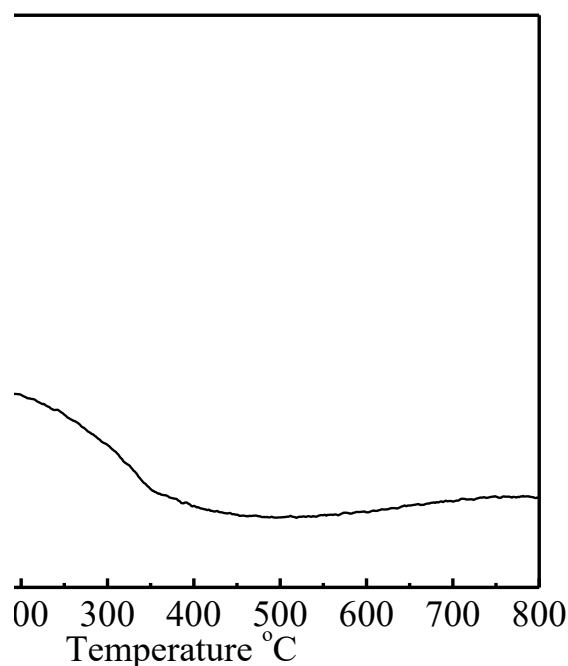


Fig. 3.16: Weight loss as a function of temperature

In fact, the kinetics i.e., the rate at which the property changes with temperature can also be measured. The instrument or the detector for TGA is a balance, called a thermo balance or thermo gravimetric analyzer. The TGA apparatus detects small mass changes of a specimen, kept in thermo balance, which caused with change in temperature of the furnace. The flow of temperature in furnace is under a controlled temperature program. Any change in sample weight can be detected by thermo

balance. Sensitivities of the order of $0.1 \mu\text{g}$ or less are determined. It can be carried out in both inert or air atmosphere. Continuously, mass change with time and temperature is recorded. Some of the major factors affecting TGA measurements include sample size, heating rate, buoyancy, electrostatic effects, gas flow and sample holder. By analyzing the TGA curve, relative mass change with respect to the initial quantity (%) is obtained.

3.9 VSM measurements

The VSM is the instrument used to measure the magnetic moment, the most fundamental quantity in magnetism, of solid samples. When a sample material is placed in uniform magnetic field, a dipole moment proportional to the product of sample susceptibility and applied field is induced in the sample. If the sample is made to undergo sinusoidal motion as well, an electrical signal will be induced in suitable located stationary pick-coils. This signal, which is at the vibration frequency, is proportional to the magnetic moment, vibration amplitude and vibration frequency. The instrument displays the magnetic moment in e. m. u. units [22]. Fig 3.17 shows a pictorial view of a VSM setup.

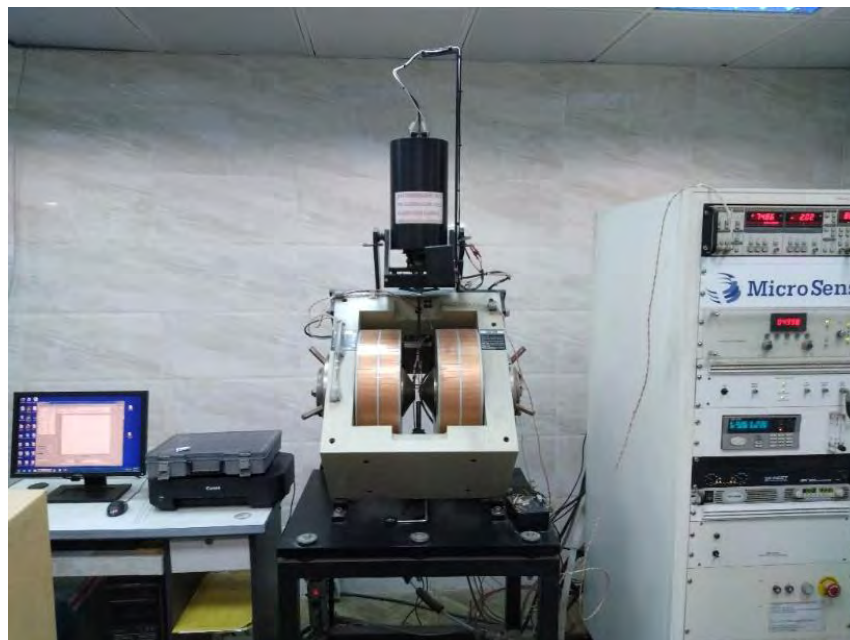


Fig. 3.17: VSM setup

3.10 DLS measurements

DLS is generally utilized to determine the particle size distribution. This analytical technique has not only become a primary technology within the spheres of screening and development of nanotechnology but is also utilized to predict and monitor the colloidal stability of such formulations.

Brownian motion is the result of thermally-driven collisions of dispersant or solvent molecules with the relevant particles. When a solution of particles diffuses under the effect of Brownian motion, the light scattered from this phenomenon will vary with time. Across long time scales, the scattering trace seems to be representative of haphazard variations regarding a mean. However, when observed on smaller time scales it is apparent that the intensity trace is not arbitrary but contains a sequence of continuous data points [23]. This continuity is the outcome of particle confinement in positions proximal to those the particles occupied a short time ago. This means, over short time intervals, the particles lack adequate time to shift far from their first positions, and hence the intensity signals are correlated. Figure 3.19 shows a typical setup of DLS.



Fig. 3.19: DLS setup

3.11 Antibacterial application of NPs

The agar diffusion test (Kirby–Bauer antibiotic testing, KB testing, or disc diffusion antibiotic sensitivity testing) is a test of the antibiotic sensitivity of bacteria. It uses antibiotic discs to test the extent to which bacteria are affected by those antibiotics. In this test, wafers containing antibiotics are placed on an agar plate where bacteria have been placed, and the plate is left to incubate. If an antibiotic stops the bacteria from growing or kills the bacteria, there will be an area around the wafer where the bacteria have not grown enough to be visible. This is called a zone of inhibition.

The size of this zone depends on many factors, one being how effective the antibiotic is at stopping the growth of the bacterium. Another factor that will influence the size of a zone is the diffusion of the antibiotic within the agar medium and varies based on the molecular configuration of the antibiotic. Once the zone diameter is measured it must be compared to a database of zone standards to determine if the bacterium being studied is Susceptible, Moderately Susceptible or Resistant to the antibiotic in question.

A pure bacterial culture is suspended in buffer, standardized to turbidity and swabbed uniformly across a culture plate. A filter-paper disk, impregnated with the compound to be tested, is then placed on the surface of the agar. The compound diffuses from the filter paper into the agar. The concentration of the compound will be highest next to the disk and will decrease as distance from the disk increases. If the compound is effective against bacteria at a certain concentration, no colonies will grow where the concentration in the agar is greater than or equal to the effective concentration. This is the zone of inhibition. This along with the rate of antibiotic diffusion is used to estimate the bacteria's susceptibility to that particular antibiotic. In general, larger zones correlate with smaller minimum inhibitory concentration (MIC) of antibiotic for those bacteria. Inhibition produced by the test is compared with that produced by known concentration of a reference compound. This information can be used to choose appropriate antibiotics to combat a particular infection [18]. Fig. 3.20 shows the agar disk diffusion method of antibacterial test.

The disk diffusion agar method tests the effectiveness of antibiotics on a specific microorganism. An agar plate is first spread with bacteria, and then paper disks of antibiotics are added. The bacteria are allowed to grow on the agar media, and then observed. The amount of space around every antibiotic plate indicates the lethality of

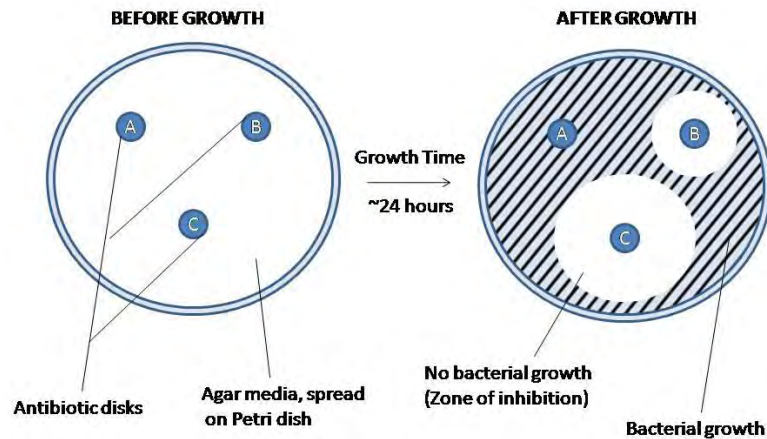


Fig. 3.20: Agar disk diffusion method

that antibiotic on the bacteria in question [24]. Highly effective antibiotics (disk C) will produce a wide ring of no bacterial growth; while an ineffective antibiotic (disk A) will show no change in the surrounding bacterial concentration at all. The effectiveness of intermediate antibiotics (disk B) can be measured using their zone of inhibition. This method is used to determine the best antibiotic to use against a new or drug-resistant pathogen.

3.11.1 Standardization of the method

Inoculation is made with a broth culture diluted to match a 0.5 McFarland turbidity standard, which is roughly equivalent to 150 million cells per mL.

3.11.1.1 Preparation

All aspects of the Kirby-Bauer procedure are standardized to ensure consistent and accurate results. Because of this, a laboratory must adhere to these standards. The media used in Kirby-Bauer testing must be Mueller-Hinton agar at only 4 mm deep, poured into either 100 mm or 150 mm Petri dishes. The pH level of the agar must be between 7.2 and 7.4. Fig. 3.21 shows the closed-up look at the result of agar diffusion test.

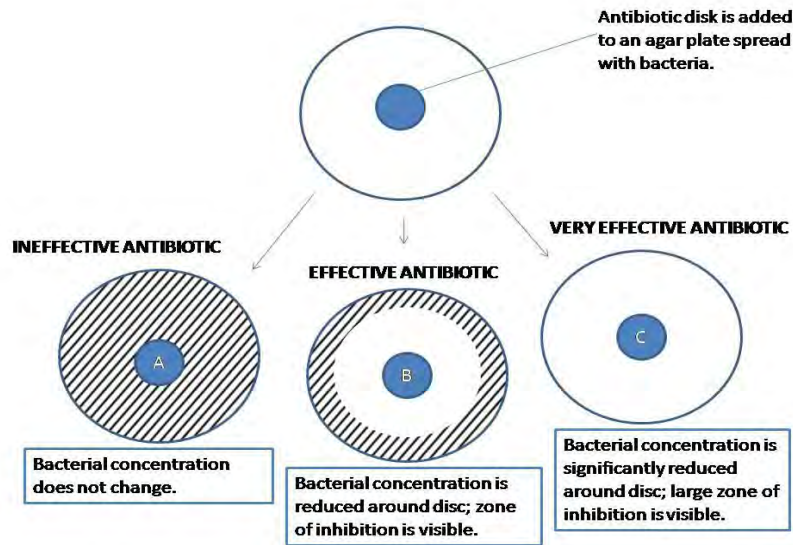


Fig. 3.21: A closed-up look at the result of agar diffusion test

3.11.1.2 Incubation procedure

- i. Using an aseptic technique, place a sterile swab into the broth culture of a specific organism and then gently remove the excess liquid by gently pressing or rotating the swab against the inside of the tube.
- ii. Using the swab, streak the Mueller-Hinton agar plate to form a bacterial lawn.
 - a. To obtain uniform growth, streak the plate with the swab in one direction, rotate the plate 90° and streak the plate again in that direction.
 - b. Repeat this rotation 3 times.
- iii. Allow the plate to dry for approximately 5 minutes.
- iv. Use an Antibiotic Disc Dispenser to dispense discs containing specific antibiotics onto the plate.
- v. Using some flame-sterilized forceps, gently press each disc to the agar to ensure that the disc is attached to the agar.
- vi. Plates should be incubated overnight at an incubation temperature of 37°

Fig. 3.22 shows the Kirby-Bauer testing.

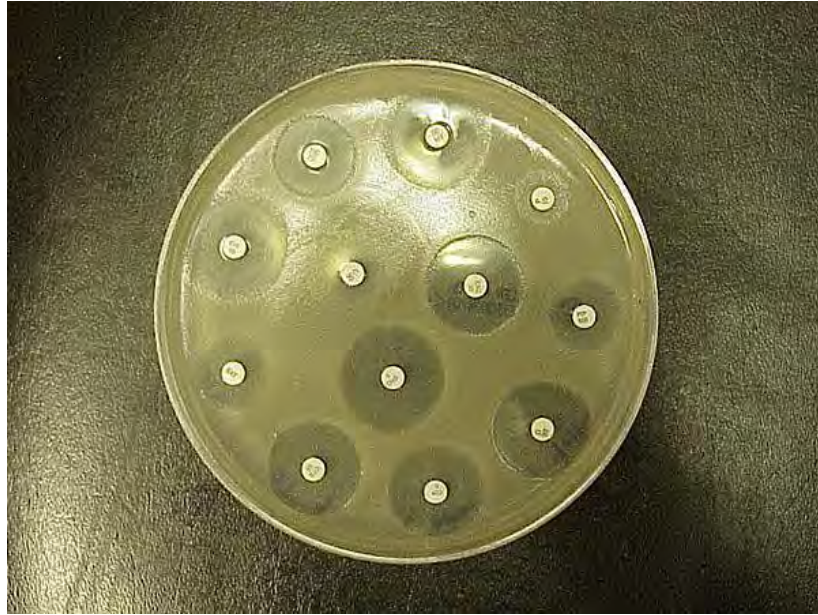


Fig. 3.22: Kirby-Bauer testing: White wafers containing antibiotics shown on plate of bacteria. Circles of poor bacterial growth surround some wafers, indicating susceptibility to the antibiotic.

References

- [1] Niamh, N. D., Kathleen, A. S., Donna, R., Ciara, H. Oliver, B. S., "Development of gas chromatography–mass spectrometry (GC–MS) and other rapid screening methods for the analysis of 16 ‘legal high’ cathinone derivatives," *Sci. Justice.*, vol. 54, pp. 22–31, 2014.
- [2] Syed, Z. H., Khushnuma, M., "GC-MS: Principle, technique and its application in Food Science," *Int. J. Curr. Sci.*, vol. 13, pp. 116-126, 2014.
- [3] Peyton, J., Gary, D. B., "Use of gas chromatographic and mass spectrometric techniques for the determination of nicotine and its metabolites," *Anal. Chem.*, vol. 34, pp. 191-224, 1999.
- [4] Jeffrey, A. G., Yaron, D., "High-energy X-ray production with pyroelectric crystals," *J. Appl. Phys.*, vol. 97, pp. 1-6, 2005.
- [5] Khan, H. U., Akram, M. K., Muhammad, H., Fazal, M., Muhammad, W. R., "Experimental study of the lattice constant and lattice spacing of potassium bromide by laue and debye scherer methods," *Int. j. sci. eng. technol.*, vol. 9, pp. 181-195, 2018.
- [6] David, H., "Crystal Structure Determination," *J. Pure Appl. Phys.*, vol. 6, pp. 187-282, 1959.
- [7] Andrei, A. B., Elena, g. U., Hassan, Y. A., "X-ray diffraction: Instrumentation and applications," *Crit. Rev. Anal. Chem.*, vol. 45, pp. 289-299, 2015.
- [8] Frankel, R. S., Aitken, D. W., "Energy-dispersive X-ray emission spectroscopy," *Appl. Spectrosc.*, vol. 24, pp. 557-566, 1970.
- [9] Min, Y., Dongyue, W., Min, Z., "Element analysis based on energy-dispersive x-ray fluorescence," *Adv. Mater. Sci.*, vol. 2015, pp. 1-8, 2015.
- [10] Michael, B., Peter, L., Dieter, N., "Analytical applications of Fourier transform-infrared (FT-IR) spectroscopy in microbiology and prion research," *Vet. Microbiol.*, vol. 123, pp. 305–319, 2007.
- [11] Helene, O., Herbert, S., Siegfried, S., "Identification of coryneform bacteria and related taxa by Fourier-transform infrared (FT-IR) spectroscopy," *Int. J. Syst. Evol. Microbiol.*, vol. 52, pp. 91–100, 2002.

- [12] JAMES, P., "The development of field-emission scanning electron microscopy for imaging biological surfaces," *Scanning*, vol. 19, pp. 324-336, 1997.
- [13] McMullan, D., "Scanning electron microscopy 1928–1965," *Scanning*, vol. 17, pp. 175–185, 1995.
- [14] David, C. J., "Beam interactions, contrast and resolution in the SEM," *J. Microsc.*, vol. 136, pp. 241-258., 1984.
- [15] Wang, Z. L., "Transmission electron microscopy of shape-controlled nanocrystals and their assemblies," *J. Phys. Chem. B*, vol. 104, pp. 1153-1175, 2000.
- [16] Varela, M., Lupini, A. R., Benthem, K., Borisevich, A. Y., Chisholm, M. F., Shibata, N., Abe, E., Pennycook, S. J., "Materials characterization in the aberration-corrected scanning transmission electron microscope," *Annu. Rev. Mater. Res.*, vol. 35, pp. 539-569, 2005.
- [17] Spence, J.C.H., "The future of atomic resolution electron microscopy for materials science," *Mater. Sci. Eng.*, vol. 26, pp. 1-49, 1999.
- [18] Wilfried, S., "Analytical transmission electron microscopy," *Annu. Rev. Mater. Res.*, vol. 35, pp. 239–314, 2005.
- [19] Hesketh, T. R., Bogart, J. W. C, Cooper, S. L., "Differential scanning calorimetry analysis of morphological changes in segmented elastomers," *Polym. Eng. Sci.*, vol. 20, pp. 190-197, 1980.
- [20] Jose, M. S. R., "Theoretical analysis of Lumry-Eyring models in differential scanning calorimetry," *Biophys. J.*, vol. 61, pp. 921-935, 1992.
- [21] Dong, K. S., Sang, S. P., Jungho, H., Tae, Y., "Study of the pyrolysis of biomass using thermo-gravimetric analysis (TGA) and concentration measurements of the evolved species," *J. Anal. Appl. Pyrolysis.*, vol. 89, pp. 66–73, 2010.
- [22] Guertin, R. P., Foner, S., "Application of a vibrating sample magnetometer to magnetic measurements under hydrostatic pressure," *Rev. Sci. Instrum.*, vol. 45, pp. 863-864, 1974.
- [23] Yasuo, K., Kikuo, O., Motoaki, A., Tadaaki, M., "Effect of brownian diffusion on electrical classification of ultrafine aerosol particles in differential mobility analyzer," *Chem. Eng. J.*, vol. 19, pp. 401-407, 1986.

- [24] Josi, P., Esteban, B., Teresa, J. A., "Antimicrobial activity of seven root canal sealers results of agar diffusion and agar dilution tests," *Endodontics* , vol. 74, pp. 216-220, 1992.

CHAPTER 4

MATERIALS AND METHODS

4.1 Chemicals and reagents

The chemicals and reagents used in this work are of analytical grade and are used without further purification. De-ionized (DI) water with resistivity 18 M Ω -cm is used as solvent in order to prepare the solutions required in this work. The chemicals and reagents used in this work are listed below:

- Ferric chloride anhydrous (FeCl₃) (Merck, India)
- Ferrous chloride tetra hydrates (FeCl₂.4H₂O) (Merck, India)
- Sodium hydroxide (NaOH) (Merck, India)
- Acetone (CH₃COCH₃) (Merck, India)
- Ethanol (CH₃OH) (Merck, India)
- Dichloromethane (CH₂Cl₂) (Merck, India)
- Sodium sulfate (Na₂SO₄) Merck, India)
- *Ipomoea aquatica* leaf extracts
- Bacto trypton, bacto agar and yeast extract (Difco Laboratories, Detroit, MI, USA)
- Escherichia coli (gram-negative bacteria) and Bacillus subtilis (gram-positive bacteria)
- DI water, etc.

4.2 Instruments

The following equipment's and instruments were used for the synthesis, characterization and antibacterial application of the Fe₃O₄ NPs:

- Ceramic mortar
- Digital balance (AB 265/S/SACT METTLER, Toletto, Switzerland)
- Centrifuge machine (ABT-028C, USA)
- Magnetic stirrer with thermostat hotplate (GALLTMKAMP, England)
- Incubator (115V) RI 115
- Muffle furnace (BINDER, Germany)

- Bath sonicator (Decon FS minor)
- X-ray Diffractometer (Philips, Expert Pro, Holland)
- Fourier Transform Infrared Spectrophotometer (Jasco-FTIR-6300)
- Field Emission Scanning Electron Microscopy (JSM-7600F, Tokyo, Japan)
- DSC and TGA machine (TA instrument, SDT Q-600)
- Transmission Electron Microscopy (JEOL, JEM 2010, Japan)
- Vibrating Sample Magnetometer (EV-9 Micro Sense, Germany)
- Dynamic Light Scattering machine (DLS 7000, Otsuka, Electronics Co., Ltd, Japan)
- Gas Chromatography Mass Spectrometer (SHIMADZU QP2010)
- Biological Bio Safety Cabinet (Model: NU-400E, Nuaire, USA), etc

Fig. 4.1 shows some of the basic equipment used for synthesis of Fe₃O₄ NPs.



Fig. 4.1: Basic equipments used for synthesis of Fe₃O₄ NPs (a) Mortar (b) Centrifuge machine (c) Magnetic stirrer (d) Digital balance (e) Electric oven (f) Bath sonicator

4.3 Synthesis of Fe₃O₄ NPs

Fe₃O₄ NPs were synthesized via a facile green synthesis route where FeCl₃ and FeCl₂·4H₂O were used as precursor and *Ipomoea aquatica* leaf extract was used as a source of reducing and capping agents. To synthesis Fe₃O₄ the *Ipomoea aquatica* leaf extract added to an aqueous mixture of Fe³⁺ and Fe²⁺ chloride at a 2:1M ratio [1]. The

chemical reaction of Fe_3O_4 precipitation is given below. Fig. 4.2 shows the schematic diagram of the interaction between Fe_3O_4 NPs charged groups which were capped by *Ipomoea aquatica* leaf extract. The overall reaction may be written as follows:

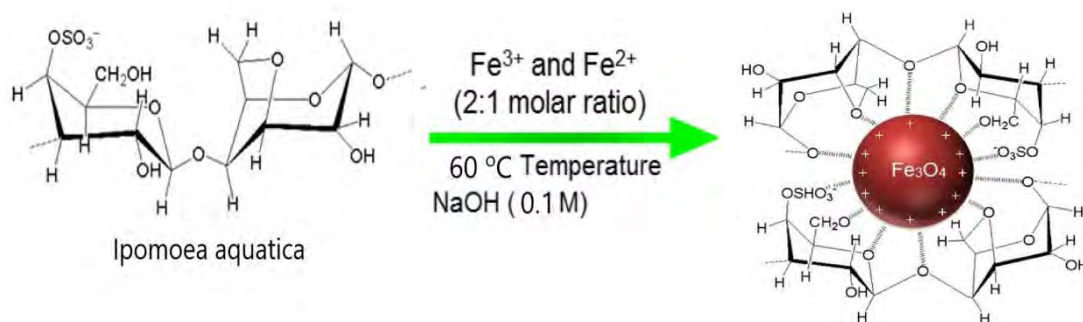
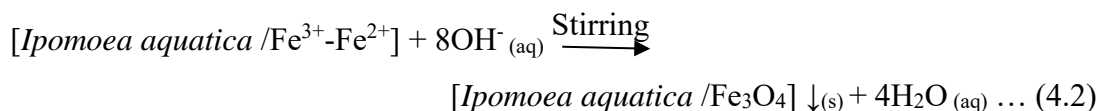
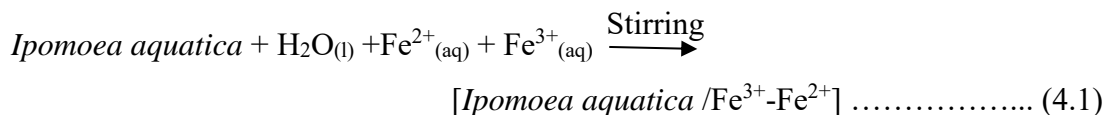


Fig. 4.2: Schematic diagram demonstrating the interaction between Fe_3O_4 NPs charged groups which are capped by *Ipomoea aquatica* leaf extract

4.3.1 Leaf extracts preparation

The preparation of *Ipomoea aquatica* leaf extract is given below:

- i. The healthy leaves of *Ipomoea aquatica* were collected from the local places. The collected leaves were gently washed to remove dust. Leaves were air dried for 10

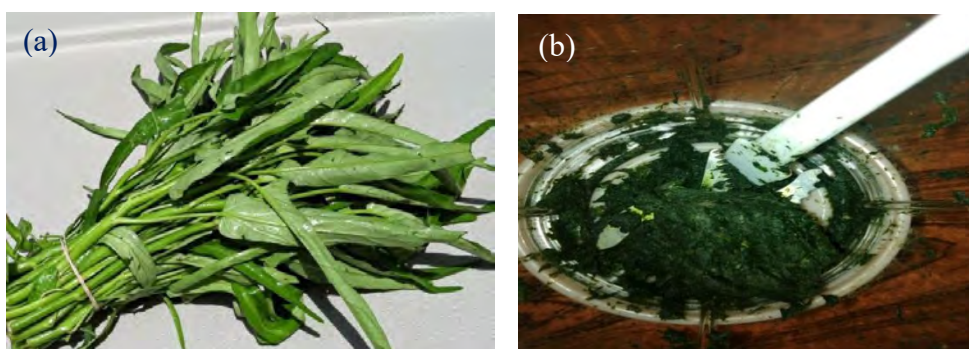


Fig. 4.3: *Ipomoea aquatica* (a) healthy green leaves and (b) finest leaves paste

hours under dust free condition. Dried leaves were cut into fine pieces, grinded and sieved to get the finest paste. The green leaves, and finest paste are shown in Fig. 4.3.

- ii. 60 g of the leaves paste was mixed with 400 mL De-ionized water and heated at 80 °C for 4 h 30 min. Preparation of leaf extracts shown in Fig 4.4.



Fig. 4.4: Preparation of *Ipomoea aquatica* leaf extracts

- iii. After 2 h, the leaf extracts was obtained by filtering the mixture through Whatman No.1 filter paper shown in Fig. 4.5 and stored at 4 °C for further experiments.



Fig. 4.5: *Ipomoea aquatica* leaf extracts

The graphical representation of *Ipomoea aquatica* leaf extract preparation is shown in Fig. 4.6.

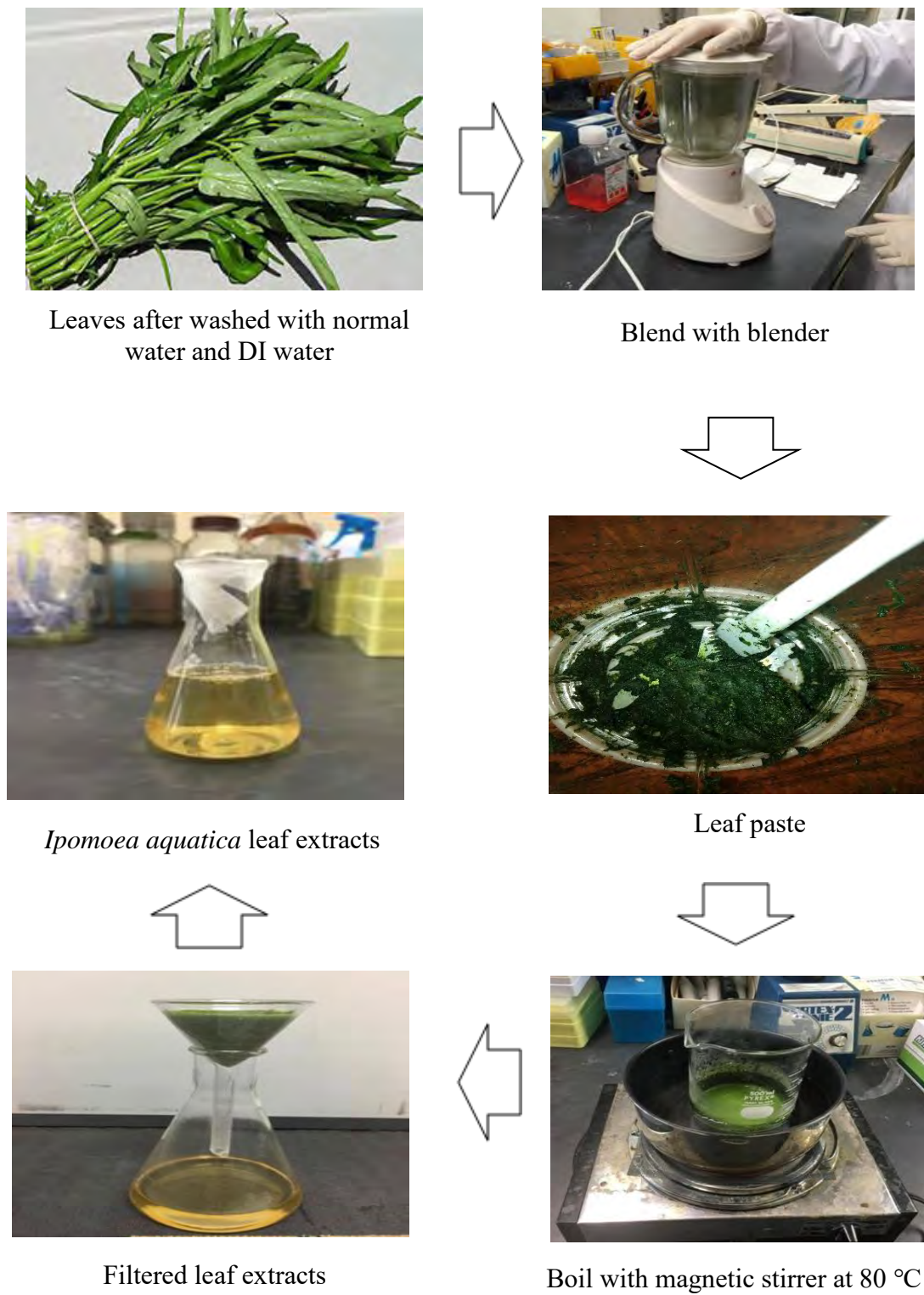


Fig. 4.6: *Ipomoea aquatica* leaf extracts preparation

4.3.2 GC-MS analysis of *Ipomoea aquatica* leaf extracts

The details procedure of GC-MS analysis of *Ipomoea aquatica* leaf extracts are given below. Fig. 4.7 shows the instrumental setup of essential oil collection from *Ipomoea aquatica* leaf extracts.

- i. For GC-MS analysis the leaf extracts solution of *Ipomoea aquatica* was made by mixing 40 gm leaf paste with 400 ml DDW.
- ii. The healthy leaves of *Ipomoea aquatica* were collected from the local places. The collected leaves were gently washed to remove dust particles. Then the leaves were air dried for 10 h under dust free condition. After that dried leaves were cut into fine pieces, grinded and sieved to get the finest paste. The green leaves, and finest paste are shown in Fig. 4.2
- iii. 40 gm of leaf paste mixed with 400 ml DDW and stirring with magnetic stirrer at 800 rpm with 80 °C temperatures till 2 h.
- iv. The essential oil for GC-MS analysis was collected from this leaf extracts solution by heating it at 100 °C till 2.30 h.
- v. By heating leaf extracts 100 mL essential oil was collected which was mixed with water.



Fig. 4.7: Instrumental setup of essential oil collection from *Ipomoea aquatica* leaf extracts

- vi. CH_2Cl_2 was mixed with the essential oil to remove water.
- vii. Na_2SO_4 was mixed with the essential oil to remove reaming water.
- viii. The nitrogen gas was followed over the essential oil to condense it.

4.3.3 Synthesis of Fe₃O₄ NPs

The details procedure of Fe₃O₄ NPs synthesis are given below:

- i. 0.99 g FeCl₂.4H₂O added with 100 mL DI water to make 0.05 M solution and 1.622 g FeCl₃ added with 100 ml DI water to make 0.1 M solution. The prepared solutions are shown in Fig. 4.8 (a)
- ii. 10 mL 0.05 M FeCl₂.4H₂O and 10 mL 0.1M FeCl₃ mixed together in a separate beaker with magnetic stirrer. The prepared solutions are shown in Fig. 4.8 (b)

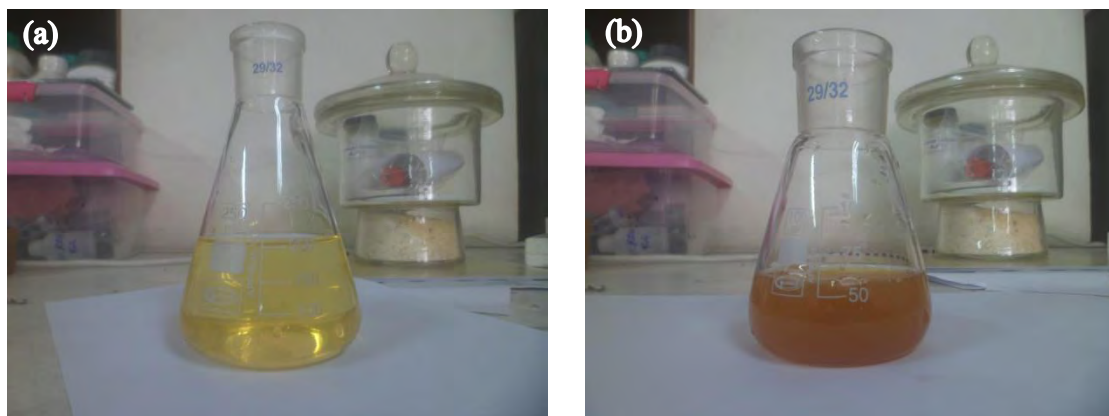


Fig. 4.8: Solution of (a) FeCl₂.H₂O and (b) FeCl₃

- iii. After 10 min 2 mL *Ipomoea aquatica* leaf extract added with the mixture and continued stirring with magnetic stirrer, which is shown in Fig. 4.9.



Fig. 4.9: Solution after addition of *Ipomoea aquatica* leaf extracts

- iv. Again, after 10 minutes 50 mL 0.1 M NaOH solution added and during NaOH addition, the solution color turned into black which denoted the formation of Fe_3O_4 NPs. The color change of the solution is shown in Fig. 4.10.



Fig. 4.10: Solution color turned black after addition of NaOH

- v. The NPs separated with a magnetic separator and dried in an oven at 60 °C. The NPs then stored at 4 °C for further characterization. The separation process of NPs from the solution with a magnet is shown in Fig. 4.11 and the of Fe_3O_4 NPs synthesis is shown in Fig. 4.12.



Fig. 4.11: Magnetic separation of Fe_3O_4 NPs (a) before applying magnetic field (b) after applying magnetic field



Fig. 4.12: Fe_3O_4 NPs synthesis

4.3.4 Synthesis of Fe₃O₄ NPs with the variation of NaOH concentration

The details procedure of Fe₃O₄ NPs synthesized with different concentrations of NaOH are given below:

- i. 0.99 g FeCl₂.4H₂O added with 100 mL DI water to make 0.05 M solution and 1.622 g FeCl₃ added with 100 ml DI water to make 0.1 M solution.
- ii. A mother solution of NaOH was made with 1.0 M concentration. Which was further used to synthesis Fe₃O₄ NPs with different concentrations of NaOH.
- iii. 10 mL 0.05 M FeCl₂.4H₂O and 10 mL 0.1 M FeCl₃ mixed together in a separate beaker with magnetic stirrer.
- iv. After 10 min 2 mL *Ipomoea aquatica* leaf extract added with the mixture and continued the stirring with magnetic stirrer.
- v. To synthesis Fe₃O₄ NPs with different concentrations of NaOH, at this stage different concentrations of NaOH added to the solution such as 1.0, 0.5, 0.1 and 0.05 M, respectively and observed the change of solution color.
- vi. The NPs separated with a magnetic separator and dried in an oven at 60 °C temperature. The NPs then stored at 4 °C for further characterization.

4.3.5 Synthesis of Fe₃O₄ NPs with the variation of FeCl₃ and FeCl₂.4H₂O concentration

The details procedure of Fe₃O₄ NPs synthesized with different concentrations of FeCl₃ and FeCl₂.4H₂O are given below:

- i. Mother solution of FeCl₃ and FeCl₂.4H₂O was made with 1 M and 0.5 M concentration, respectively. It was further used to synthesis Fe₃O₄ NPs with different concentrations of FeCl₃ and FeCl₂.4H₂O.
- ii. To synthesis Fe₃O₄ NPs with different concentrations of FeCl₃ and FeCl₂.4H₂O, the solution of FeCl₃ and FeCl₂.4H₂O at different concentrations mixed together in a separate beaker with magnetic stirrer. In this case the concentrations of FeCl₃ was 1.0, 0.2, 0.1, 0.02 and 0.01 M, respectively and the concentration of FeCl₂.4H₂O was 0.5, 0.1, 0.05, 0.01 and 0.005 M respectively.
- iii. After 10 minutes' different volume of *Ipomoea aquatica* leaf extracts added with the mixture according to the concertation of FeCl₃ and FeCl₂.4H₂O solution. In this case the volume of *Ipomoea aquatica* leaf extract was 5, 10, 15, 20 and 25 mL, respectively.

- iv. Again, after 10 min 50 mL 0.1 M NaOH solution added and during NaOH addition, the solution color turned into black which denoted the formation of Fe_3O_4 NPs.
- v. The NPs separated with a magnetic separator and dried in an oven at 60 °C. The NPs then stored at 4 °C for further characterization.

4.3.6 Disperse Fe_3O_4 NPs in solvent

Fe_3O_4 NPs possess distinct “solubilities” in aqueous and non-aqueous solvents, depending on their size and the type of functionalizing molecules. The capacity to be solubilized or dispersed for short or long periods and the stability of Fe_3O_4 NPs in liquid phases is very important for the abovementioned applications, and hence, considerable efforts have been made to achieve a higher solubility of Fe_3O_4 NPs, first of all in aqueous media [2]. Highly soluble Fe_3O_4 NPs have much greater applications in biomedicine; soluble Fe_3O_4 NPs have stronger remediation effects compared to the insoluble ones. The procedure of disperse Fe_3O_4 NPs in solvent are given below,

- i. 5 mL Diethylene glycol (DEG) and 5 mL DI water mixed together to make 50% DEG solution.
- ii. 60 mg Fe_3O_4 NPs added in 50% DEG solution
- iii. After addition of NPs the solution sonicated 30 min to disperse the NPs in the solution. The disperse solution of Fe_3O_4 is shown in Fig. 4.13.



Fig. 4.13: Disperse solution of Fe_3O_4 NPs in DDW

4.4 Characterizations of Fe₃O₄ NPs

4.4.1 Elemental analysis of the leaf extracts

GC-MS analysis was performed to determine the element of the leaf extracts [3]. For this essential oil of the leaf extract collected from the leaves solution. This essential oil then injected in the GC column to separate the particles and detected with the Mass Spectrometer.

4.4.2 XRD analysis

Fe₃O₄ NPs were analyzed for their XRD patterns in the powder state [4]. The powder samples were pressed in a square aluminum sample holder (40 mm × 40 mm) with a 1 mm deep rectangular hole (20 mm × 15 mm) and pressed against an optical smooth glass plate. The upper surface of the sample was labeled in the plane with its sample holder. The sample holder was then placed in the diffractometer in order to get the diffraction patterns of Fe₃O₄ NPs.

4.4.3 EDX spectral analysis

Elemental characterization of the synthesized Fe₃O₄ NPs was carried out using EDX analysis [5]. The dried powders of Fe₃O₄ NPs were placed on a 1cm×1cm conducting steel plate. The steel plate was then placed on a conducting carbon glued strip. The sample was then placed in the main FESEM chamber integrated with the EDX instrument.

4.4.4 FESEM analysis

The surface morphology of the Fe₃O₄ NPs was adopted using FESEM technique. The dried powders of the synthesized Fe₃O₄ NPs were dispersed on a conducting carbon glued strip [6]. The sample loaded strip was then mounted to a chamber that evacuated to $\sim 10^{-3}$ to 10^{-4} torr and then a very thin carbon layer (~few nanometers thick) were sputtered on the sample to ensure the conductivity of the sample surface. The sample was then placed in the main FESEM chamber to view its surface. The system was computer interfaced and thus provided recording of the surface images in the computer file for its use as hard copy.

4.4.5 FT-IR spectral analysis

The FT-IR spectra of the dried samples of Fe₃O₄ NPs were recorded on an FTIR spectrometer in the region of 4000 – 400 cm⁻¹ [7]. FT-IR spectra of the solid samples

were obtained by mixing and grinding a small amount of materials with dry and pure KBr crystals. The mixing and grinding were done in a mortar by a pestle. The powder mixture was then compressed in a metal holder under a pressure of 8–10 tons to make a pellet. The pellet was then placed in the path of IR beam for measurements.

4.4.6 TEM analysis

The sizes along with surface morphology of Fe₃O₄ NPs were measured by TEM. A suspension of Fe₃O₄ NPs with ethanol was prepared, and 1 μL of the suspension was placed on formvar coated grid, allowed to dry at room temperature (25 °C) and then kept on a specimen holder in order to perform TEM analysis [8]. The image was viewed at an accelerating voltage of 120 kV.

4.4.7 Thermal analyses

Thermal behavior of the synthesized Fe₃O₄ NPs was analyzed through DSC and TGA. The DSC and TGA analyses of the sample were performed from ambient temperature to 800 °C respectively using a DSC/TGA analyzer [9].

4.4.8 Magnetic property analysis

Pure powders were tested in order to ensure magnetic behavior of Fe₃O₄ NPs. For this scheme, the first step was construction of a vibrating mechanism which can be vibrated the sample with measurable and controllable amplitude [10]. Finally, detection coils detect the magnetic field perturbations produced by vibrating the Fe₃O₄ NPs sample in the applied magnetic field.

4.4.9 DLS analysis

DLS analysis was performed to determine the particles size distribution. For this a disperse solution of NPs was prepared first with 0.25 mgL⁻¹ concentration, then the solution was sonicated in a bath sonicator to disperse the particles homogenously at the solution [11]. A cube was filled with 3 ml solution and put the cube at sample holder to determine the particles size distribution.

4.5 Antibacterial application of Fe₃O₄ NPs

The antibacterial activity of Fe₃O₄ NPs was measured by disc diffusion method as described in section 3.10. Gram negative bacteria (*E. coli*) and gram-positive bacteria (*B. subtilis*) were taken in order to investigate their applications against pathogens. Bacteria were cultured in Luria Broth (LB) medium (tryptone 1.5%, yeast extract

0.75%, sodium chloride 1.2%) at 37 °C with 60 rpm shaking in water bath. Fresh culture containing 6.6×10^6 bacteria measured by the optical density at 600 nm was used for the experiments [12]. To measure the inhibition zone, 50 μ L of medium containing bacteria were poured into LB plate with 1% agar. For disc preparation, medium containing bacteria were poured into LB plate with 1% agar. For disc preparation, filter paper is punched, autoclaved and dried at 60 °C for overnight. Subsequently, the discs (5 mm sized) are soaked with 15 μ L of Fe₃O₄ NPs suspensions and placed on culture plate at 37 °C for 24 h.

References

- [1] Hironori, I., Kosuke, T., Takuya, N., Tetsuya, O., "Synthesis of Fe₃O₄ nanoparticles with various sizes and magnetic properties by controlled hydrolysis," *J. Colloid Interface Sci.*, vol. 314, pp. 274–280, 2007.
- [2] Hui, Lu., Salabas, E. L., Ferdi, S., "Magnetic nanoparticles: synthesis, protection, functionalization, and application," *Angew. Chem. Int. Ed.*, vol. 46, pp. 1222 – 1244, 2007.
- [3] Syed, Z. H., Khushnuma, M., "GC-MS: Principle, technique and its application in food science," *Int. J. Curr. Sci.*, vol. 13, pp. 116-126, 2014.
- [4] Andrew, M. S., Shuming, N., "Semiconductor nanocrystals: structure, properties, and band gap engineering," *Acc. Chem. Res.*, vol. 43, pp. 190-200, 2010.
- [5] Wang, Z., "Iron complex nanoparticles synthesized by eucalyptus leaves," *ACS Sustain. Chem. Eng.*, vol. 1, pp. 1551–1554, 2013.
- [6] Njagi, E.C.; Huang, H.; Stafford, L., Genuino, H., Galindo, H. M., Collins, J. B., Hoag, G. E., Suib, S. L., "Biosynthesis of iron and silver nanoparticles at room temperature using aqueous Sorghum bran extracts," *Langmuir*, vol. 27, pp. 264–271, 2011.
- [7] Bharde, A., Rautaray, D., Bansal, V., Ahmad, A., Sarkar, I., Yusuf, S. M., Sanyal, M., Sastry, M., "Extracellular biosynthesis of magnetite using fungi," *Small*, vol. 2, pp. 135–141, 2006.
- [8] Luo, F., Chen, Z., Megharaj, M., Naidu, R., "Biomolecules in grape leaf extract involved in one-step synthesis of iron-based nanoparticles," *RSC Adv.*, vol. 4, pp. 53467–53474, 2014.
- [9] Rao, A., Bankar, A., Kumar, A. R., Gosavi, S., Zinjarde, S., "Removal of hexavalent chromium ions by *Yarrowia lipolytica* cells modified with phyto-inspired Fe//Fe₃O₄ nanoparticles," *J. Contam. Hydrol.*, vol. 146, pp. 63–73, 2013.
- [10] Shahwan, T.; Abu, S. S., Nairat, M., Boyacı, E., Eroglu, A. E., Scott, T. B., Hallam, K. R., "Green synthesis of iron nanoparticles and their application as a fenton-like catalyst for the degradation of aqueous cationic and anionic dyes," *Chem. Eng. J.*, vol. 172, pp. 258–266, 2011.

- [11] Bharde, A. A., Parikh, R. Y., Baidakova, M., Jouen, S., Hannoyer, B., Enoki, T., Prasad, B., Shouche, Y.S., Ogale, S., Sastry, M., "Bacteria-mediated precursor-dependent biosynthesis of superparamagnetic iron oxide and iron sulfide nanoparticles," *Langmuir*, vol. 24, pp. 5787–5794, 2008.
- [12] Xi, Z., Aleksandar, F. R., Jun, W., Robert, L., Jinjun, S., "Nanomedicine in the management of microbial infection — Overview and perspectives," *Nano Today*, vol. 9, pp. 478–498, 2014.

CHAPTER 5

RESULTS AND DISCUSSION

5.1 GC-MS spectra analysis of *Ipomoea aquatica* leaf extracts

GC-MS is a widely used method for the identification of organic compounds in complex mixtures. Identification is typically carried out by matching measured spectra with the spectra in a reference library [1]. The extract of *Ipomoea aquatica* was subjected to GC-MS analysis with Elite – DB-5M column and the GC-MS solution version 2.53 software. Initially oven temperature was maintained at 70 °C for 2.0 minutes and the temperature was gradually increased up to 300 °C at 10.0/30.0 min and 4.0 µl of sample was injected for analysis. Helium gas 99.99% of purity was used as a carrier gas as well as an eluent. The flow rate of helium gas was set to 1.5 mL/min. The sample injector temperature was maintained at 260°C and the split ratio is 20 throughout the experiment periods. The ionization mass spectroscopic analysis was done with 70 eV. The mass spectra were recorded for the mass range 40-500 m/z for about 57 minutes. Fig. 5.1 shows the GC-MS spectra of *Ipomoea aquatica* leaf extracts.

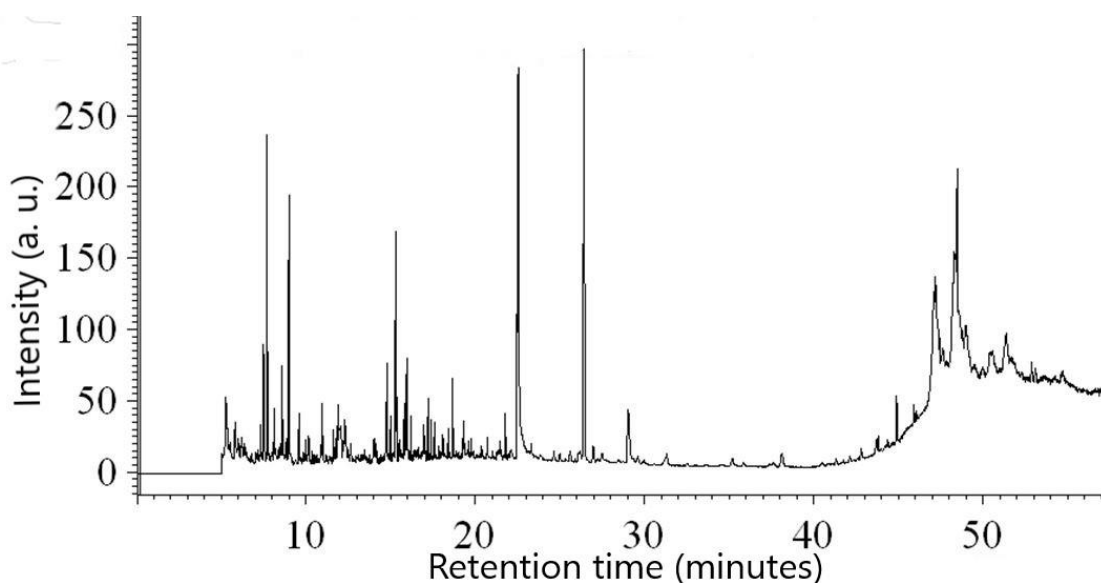


Fig. 5.1: GC-MS spectra of *Ipomoea aquatica* leaf extracts

Identification of components was based on comparison of their mass spectra. As the compounds separated, on elution through the column, were detected in electronic signals. As individual compounds eluted from the Gas chromatographic column, they entered the electron ionization detector where they were bombarded with a stream of electrons causing them to break apart into fragments. The fragments were actually charged ions with a certain mass. The m/z ratio obtained was calibrated from the graph obtained which was called as the mass spectrum graph which is the fingerprint of the molecule. The identification of compounds was based on the comparisons of their mass spectra with NIST Library 2008 WILEY, FAME. The chromatogram (Table 5.1) shows more than 75 prominent peaks in the retention time range 5 -57 minute. The GC-MS analysis of hydro alcoholic extract of *Ipomoea Aquatica* Forsk reveals the presence of phytoconstituents belonging to the category of sterols, acids, esters, alcohols and ethers etc.

Table 5.1: Compositions of leaf extract according to their functional group

Compound Name	Element Area%	Functional Group	Area%
2,4-Decadien-1-ol	2.52	Alcohol	20.54
2,4-Pentadien-1-ol, 3-ethyl-, (2Z)	0.21		
1-Hexanol, 2-ethyl	0.49		
Benzyl Alcohol	1.87		
Phenylethyl Alcohol	3.63		
2-Adamantanol, 2-(bromomethyl)-	0.19		
Benzenemethanol, 2-chloro-	0.19		
3-Butene-1,2-diol, 1-(2-furanyl)-	0.18		
pentadecanal	0.85		
Phytol	10.41		
1,3-Benzodioxole, 4-methoxy-6-(2-propenyl)	0.87	Phenol	3.80
Phenol, 2,6-dimethoxy-4-(2-propenyl)-	0.10		
2-(4-Hydroxyphenyl)-2-(4-methoxyphenyl)	0.45		
Phenol, 4,4-(1-methylethylene) bis-	2.16		
2-Phenyl-2-(4-trimethylsilyloxyphenyl) pr	0.22		
1-Ethyl-1-methylcyclohexane	0.94	Elkene	5.95

Spiro [2,4] hepta-4,6-diene	4.07				
Alpha-Caryophyllene	0.40				
Naphthalene, 1,2,3,4,4a,5,6,8a-octahydro-1,1,7-trimethyl-	0.35				
7-Tetradecene	0.19				
2-Cyclohexen-1-one, 4,5-dimethyl-	0.28	Ketone	5.58		
2,6,6-Trimethyl-2-cyclohexene-1, 4-dione	0.49				
3-Buten-2-one, 4-(2,6,6-trimethyl-1-cyclohexen-1-yl)-	2.11				
3-Buten-2-one, 4-(2,2,6-trimethyl-7-oxabicyclo[4.1.0]hept-1-yl)-	1.06				
2(4H)-Benzofuranone, 5,6,7,7a-tetrahydro-4,4,7a-trimethyl-	0.47				
Cyclooctasiloxane, hexadecamethyl-	0.63				
Cyclononasiloxane, octadecamethyl-	0.44				
2-Pentadecanone, 6,10,14-trimethyl-	0.10				
Benzaldehyde, 2,4-dimethyl-	0.26			Aldehyde	1.48
1-Cyclohexene-1-carboxaldehyde, 2,6,6-trimethyl	0.76				
2,6,6-Trimethyl-1-cyclohexene-1-acetaldehyde	0.23				
Vanillin Or 4-Hydroxy-3-methoxybenzaldehyde	0.23				
Benzenamine, 3-methyl-	0.61	Amine	12.27		
Azobenzene	0.42				
Hydroxylamine, O-decyl-	0.37				
Hydroxylamine, O-decyl-	0.22				
3-(Trifluoromethyl) benzylamine 98%	5.03				
3-(Trifluoromethyl) benzylamine	1.40				
3-(Trifluoromethyl) benzylamine	1.82				
3-(Trifluoromethyl) benzylamine	2.40				
2-Hexenoic acid, 3,4,4-trimethyl-5-oxo- OR 3,4,4-trimethyl-5-oxo-2-hexenoic acid	0.27	Carboxylic Acid	11.52		
Tetradecanoic acid	0.19				

8,11,14-Eicosatrienoic acid, (Z, Z, Z)-	0.09		
1,2-Benzenedicarboxylic acid, butyl 2-methyl	1.70		
n-Hexadecanoic acid	9.27		
m-Toluic acid, 4-nitrophenyl ester	0.06	Ester	1.87
9-Octadecen-12-ynoic acid, methyl ester	0.22		
Phthalic acid, isobutyl nonyl ester	0.18		
Pentadecanoic acid, 14-methyl-, methyl ester	0.73		
1,2-Benzenedicarboxylic acid, diisooctyl ester	0.68		

5.2 XRD pattern analysis of Fe₃O₄ NPs

Fe₃O₄ NPs were characterized by XRD for structural determination and estimation of crystallite size. Generally, XRD can be used to characterize the crystallinity of NPs, as well as the average crystallite size. All the peaks of XRD patterns were analyzed and indexed after comparing with magnetite (Fe₃O₄) standards (JCPDS card no. 00-003-0863) [2]. The peaks indexed at $2\theta = 30.30^\circ, 35.40, 43.21, 53.44, 57.03, 62.52$ as planes (220), (311), (400), (422), (511) and (440) are corresponded to a cubic unit cell, characteristic of a cubic inverse spinal structure shown in Fig. 5.2.

Fig. 5.2: XRD pattern of Fe₃O₄ NPs

The characteristic strongest reflection proceeded from the (311) plane was another confirmation of cubic inverse spinel structure. No diffraction peak other than those of Fe₃O₄ was observed, indicating that highly phase-pure Fe₃O₄ particles were obtained. The peaks shown in the XRD patterns of the prepared sample are sharp and intense, indicating good crystallinity of Fe₃O₄ NPs and due to the broad diffraction pattern lines, it can be said that particles have size about of nanometers. Crystallite size measurements were determined from the full-width at half maximum (FWHM) of the strongest reflection of the (311) peak, using the Scherrer approximation, which assumes the small crystallite size to be the cause of line broadening [3].

$$D = \frac{k\lambda}{\beta \cos\theta} \dots\dots\dots (5.1)$$

Here, D is the crystallite size; k is the shape parameter, which is 0.89 for magnetite, λ is the X-ray wavelength (0.15406 nm), β the full width at half maximum (FWHM) in radians in the 2θ scale, and θ is the Bragg angle. Taking the highest intensity peak, namely the (311) plane, at 2θ = 35.40 (0.6178 radian) for which FWHM is 0.6364 (0.0176 radian), the crystal size calculated were 12.8 ± 0.8 nm.

From this XRD analysis the structural parameter such as dislocation density, microstrain are also determined. The dislocation density is a measure of the number of dislocations in a unit volume of a crystalline material [4]. A count of the number of etch pits per unit area on the etched surface gives the dislocation density. The root mean square of the variations in the lattice parameters across the individual crystallites, usually across microscopic distances. By definition, it cannot be negative. In contrast, macrostrain refers to the overall change in the lattice parameters caused by a composition change or temperature change or pressure change [5]. The dislocation density and microstrain of Fe₃O₄ NPs were calculated by using following formula, respectively.

$$\delta = \frac{1}{D^2} \dots\dots\dots (5.2)$$

$$\varepsilon = \frac{\beta \cos\theta}{4} \dots\dots\dots (5.3)$$

where, D is the crystallite size which is calculated using Scherrer approximation and β is the FWHM which is obtained from XRD analysis of Fe₃O₄ NPs. The structural

parameter of Fe₃O₄ NPs obtained from XRD analysis are shown in table 5.2. The calculated average δ and ϵ were $(5.5 \pm 0.9) \times 10^{-3}$ and $(11.1 \pm 2.2) \times 10^{-3}$, respectively.

Table 5.2: Structural parameters of Fe₃O₄ NPs obtained from XRD analysis

Plane (hkl)	FWHM (deg)	Crystallite size D (nm)	Dislocation density (δ) Line/nm ² $\times 10^{-3}$	Macrostrain (ϵ) $\times 10^{-3}$
(200)	0.62	11.9	5.2	13.4
(311)	0.64	13.5	5.5	13.1
(400)	0.69	13.0	6.0	12.6
(422)	0.64	12.6	4.7	9.4
(511)	0.64	13.8	4.6	8.7
(533)	0.81	12.0	6.9	9.2

5.2.1 XRD patterns analysis for variation of NaOH concentration

Fe₃O₄ NPs synthesized with different concentrations of NaOH were performed XRD analysis to determine the crystallinity of the NPs. Fig. 5.3 shows the XRD patterns of the Fe₃O₄ NPs which was synthesized with different concentrations of NaOH. From the XRD patterns it was observed that all of the sample peaks indexed at $2\theta = 30.30^\circ, 35.40,$

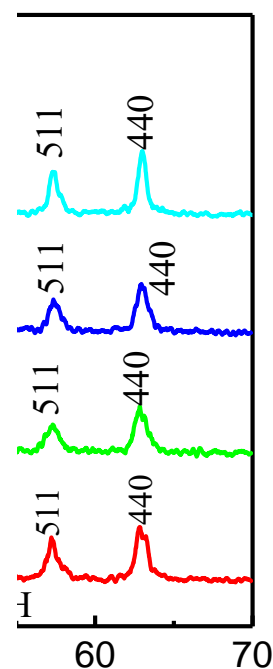


Fig. 5.3: XRD patterns of Fe₃O₄ NPs synthesized with different concentrations of NaOH

43.21, 53.44, 57.03, 62.52 are corresponded to the planes (220), (311), (400), (422), (511) and (440) respectively as shown in Fig. 5.3, which confirmed that all of the sample has cubic inverse spinal crystalline phase, no other impurity phase is observed. The structural parameter such as crystallite size, dislocation density, microstrain were calculated using the equation 5.1, 5.2, and 5.3, respectively. The structural parameters of all of the samples are shown in the table 5.3. The crystallites size of the NPs gets decreased with the decreasing of concentration of NaOH, which is shown in Fig. 5.4. It is well known that green synthesis is basically a chemical process. Here reducing and precipitation are the main chemical reactions involved in the process, as the precipitation rate is get decreased with the decreasing of NaOH concentration so that the particles size also gets decreased.

Table 5.3: Structural parameters of Fe₃O₄ NPs synthesis with different concentrations of NaOH

Concentration of NaOH (M)	Crystallite size D (nm)	Dislocation density (δ) Line/nm ² × 10 ⁻³	Microstrain (ϵ) × 10 ⁻³
1.00	13.7	6.6	2.0
0.50	12.7	7.2	2.1
0.10	12.6	8.8	2.3
0.05	12.1	7.6	2.2

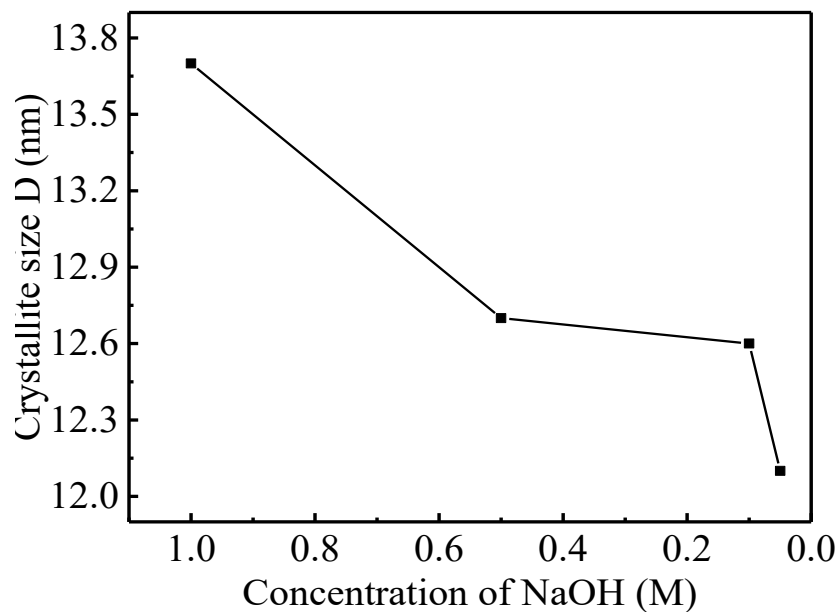


Fig. 5.4: Crystallite size vs concentration of NaOH

5.2.2 XRD patterns analysis for the variation of FeCl_3 and $\text{FeCl}_2 \cdot 4\text{H}_2\text{O}$ concentration

Fe_3O_4 NPs synthesized with different concentrations of FeCl_3 and $\text{FeCl}_2 \cdot 4\text{H}_2\text{O}$ were also performed XRD analysis to determine the crystallinity of the NPs. Fig. 5.4 shows the XRD patterns of the Fe_3O_4 NPs which was synthesized with different concentrations of FeCl_3 and $\text{FeCl}_2 \cdot 4\text{H}_2\text{O}$. From the XRD patterns it was observed that all of the samples peaks indexed at $2\theta = 30.30^\circ, 35.40, 43.21, 53.44, 57.03, 62.52$ are corresponded to the planes (220), (311), (400), (422), (511) and (440), respectively as shown in Fig. 5.5,

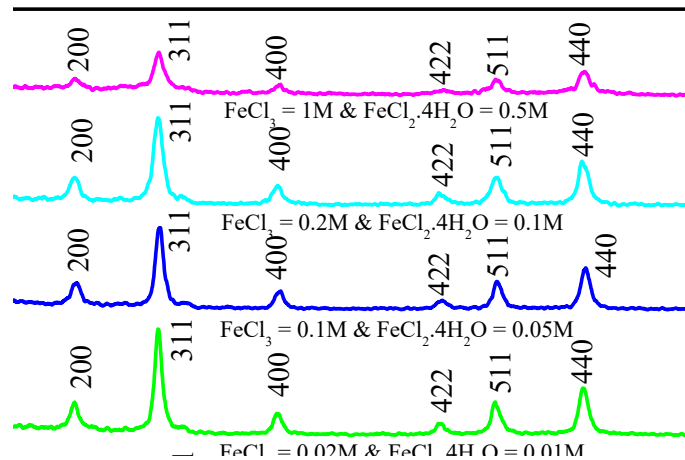


Fig. 5.5: XRD patterns of Fe_3O_4 NPs synthesized with different concentrations of FeCl_3 and $\text{FeCl}_2 \cdot 4\text{H}_2\text{O}$

which is confirmed that all of the samples have cubic inverse spinel crystalline phase, no other impurity phase is observed at all. The structural parameters such as crystallite size, dislocation density, microstrain were calculated using the equation 5.1, 5.2, and 5.3 respectively. The structural parameter of all of the samples are shown in the table 5.4. The change of crystallite size with the change of FeCl_3 and $\text{FeCl}_2 \cdot 4\text{H}_2\text{O}$ concentrations are shown in Fig. 5.6.

Table 5.4: Structural parameters of Fe₃O₄ NPs synthesized with different concentrations of FeCl₃ and FeCl₂.4H₂O

Concentration of FeCl ₃ (M)	Concentration of FeCl ₂ .4H ₂ O (M)	Crystallite size D (nm)	Dislocation density (δ) Line/nm ² $\times 10^{-3}$	Microstrain (ϵ) $\times 10^{-3}$
1.00	0.50	13.7	6.6	2.0
0.20	0.10	12.7	7.2	2.1
0.10	0.05	12.3	8.8	2.3
0.02	0.01	12.1	7.6	2.2
0.01	0.005	12.4	7.2	2.9

Fig. 5.6: Crystallites size vs concentration of FeCl₃

5.3 EDX spectrum analysis

EDX spectroscopy analysis was carried out in order to analyze the elemental constituents of the synthesized Fe₃O₄ NPs. The EDX spectra as shown in Fig. 5.7 indicate the elemental signature of the presence of iron (Fe), oxygen (O), carbon (C)

Fig. 5.7: EDX spectrum of Fe₃O₄ NPs with *Ipomoea acuatika* leaf extracts

and nitrogen (N) in our synthesized NPs. Two intense peaks are found at around 0.3 eV and 3.2 keV in the EDX spectra indicating the presence of O and Fe respectively leads to the binding energy of iron and oxygen corresponds to the Fe₃O₄ NPs and less intense peak of Fe at 450 eV assigns to the surface of Fe₃O₄ NPs. This result confirms the presence of elemental components of the Fe₃O₄ NPs [6]. However, two less intense impurities peaks are found in the EDX spectra indicating the presence of N and C at less than 1keV which may be found due to the presence of bio-organic components in the leaf extract obtained from the synthesizing approach. The EDX spectra are clearly demonstrated that the as-synthesized Fe₃O₄ NPs are highly pure.

Table 5.5: Elemental analysis of Fe₃O₄ NPs from EDX

Element	Mass (%)
Iron (Fe)	65.34
Oxygen (O)	9.42
Carbon (C)	25.18
Nitrogen (N)	0.06

5.4 FT-IR analysis of Fe₃O₄ NPs

FT-IR spectroscopy was performed to determine the functional groups of *Ipomoea acuatika* leaf extract those acted as a stabilizer and capping agent in the synthesized of Fe₃O₄ NPs. The spectra of the Fe₃O₄ NPs synthesized with *Ipomoea acuatika* leaf extract revealed strong absorption bands at 3450, 2922, 2854, 1635, 650 and 569 cm⁻¹ as shown in Fig. 5.8.

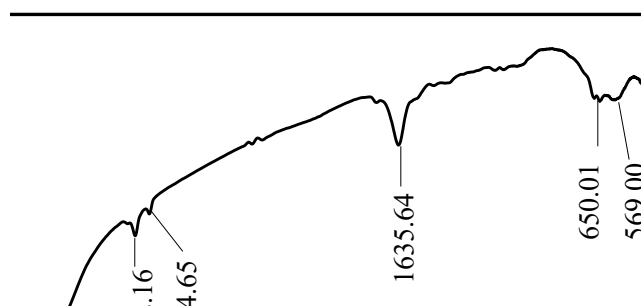


Fig. 5.8: FT-IR spectrum of Fe₃O₄ NPs

The absorption peak of 3450 cm⁻¹ in the Fe₃O₄ NPs indicated the O-H stretching vibration of alcoholic functional group. The absorption peak at 2922 cm⁻¹ contributed to the C-H anti-symmetric stretching vibrations and the absorption peaks at 2854 cm⁻¹ contributed to the C-H symmetric stretching vibrations of the -CH₂ functional group [7]. The absorption peak observed at 1635 cm⁻¹ as indicating the stretching vibration of C=C functional group. Two significant new peaks were found at 650 and 569 cm⁻¹ in the spectra of synthesized Fe₃O₄ NPs, which are associated with the stretching vibration mode of Fe-O. The metal oxygen band at 650 cm⁻¹ corresponded to intrinsic stretching vibrations of metal at the tetrahedral site, while the metal-oxygen band found at 569 cm⁻¹ was assigned to octahedral-metal stretching of Fe-O. The formation of Fe₃O₄ NPs was confirmed with these characteristic peaks as the peaks lying in the region between 400 and 700 cm⁻¹ were corresponding to Fe₃O₄ NPs. Table 5.6 shows the list of functional groups involved in the synthesis of NPs.

Table 5.6: Functional group, peak position and attribution in FT-IR of Fe₃O₄ NPs

Functional Group	Peak Position (cm ⁻¹)	Attribution
-OH	3450.65	Stretching vibration of -OH functional Group
-CH ₂ -	2922.16	Antisymmetric stretching vibration of -CH ₂ in naphthalic or aliphatic
-CH ₂ -	2854.65	Symmetric stretching vibration of -CH ₂ - in naphthalic or aliphatic
C=C	1635.64	Stretching vibration of C=C in aromatic ring or fused ring
Fe-O	569.00	Stretching vibration of Fe-O bond

5.5 FESEM analysis

The surface morphology and homogeneity of synthesized Fe₃O₄ NPs was investigated by virtue of FESEM as shown in Fig. 5.9. The FESEM image shows the high degree of

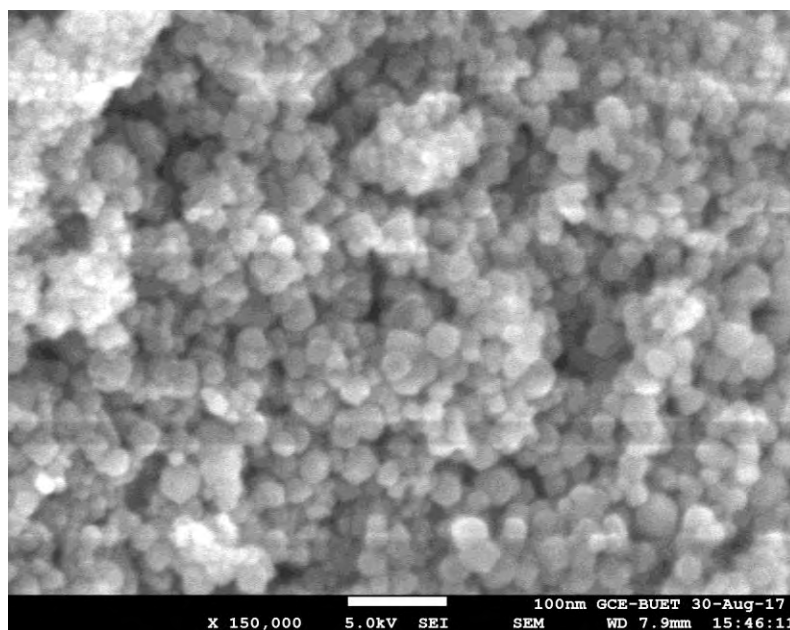


Fig. 5.9: FESEM image of surface morphology of Fe₃O₄ NPs

crystallinity of the Fe₃O₄ NPs in which surface morphology is found homogeneous and spherical in shape. The surface energy is enhanced by the largest number of charges

occupying the surface of NPs. Therefore, the surface tension of particle is higher than the larger particles, which was responsible for the spherical shape of NPs. The FESEM image of the synthesized Fe_3O_4 NPs indicates that the particles are uniformly distributed with nano meter range.

5.6 TEM analysis

TEM analysis has been employed in order to determine the size and shape of the synthesized Fe_3O_4 NPs as shown in Fig. 5.10. The TEM image clearly demonstrates that the synthesized Fe_3O_4 NPs are spherical in shape with smooth edges and uniformly distributed. The particle sizes of the synthesized NPs were found approximately in the range of 15 to 20 nm which agrees with the crystallite size calculated from the XRD patterns of Fe_3O_4 NPs. Moreover, the synthesized Fe_3O_4 NPs are found to be less agglomerated which may be due to the presence of capping agents on the surface of Fe_3O_4 NPs derived from the *Ipomoea acuatica* leaf extract as evidenced from the FT-IR and EDX analyses.

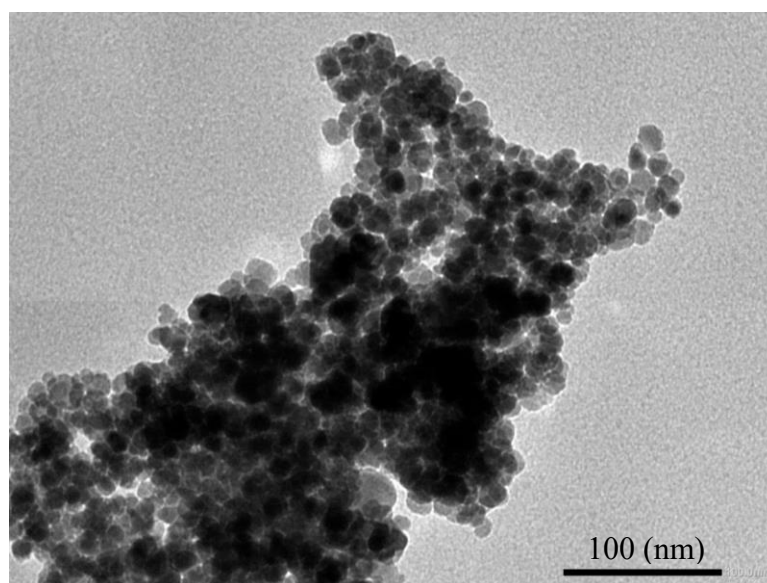


Fig. 5.10: TEM image of Fe_3O_4 NPs

5.7 DSC and TGA analysis of Fe_3O_4 NPs

To study the thermal behavior of the Fe_3O_4 NPs DSC and TGA were performed in nitrogen gas with a flow rate of 10 ml min^{-1} . The sample was heated from 25 to $800 \text{ }^\circ\text{C}$ at a rate of $10 \text{ }^\circ\text{C min}^{-1}$. Fig. 5.11 shows the DSC/TGA graph of Fe_3O_4 NPs.

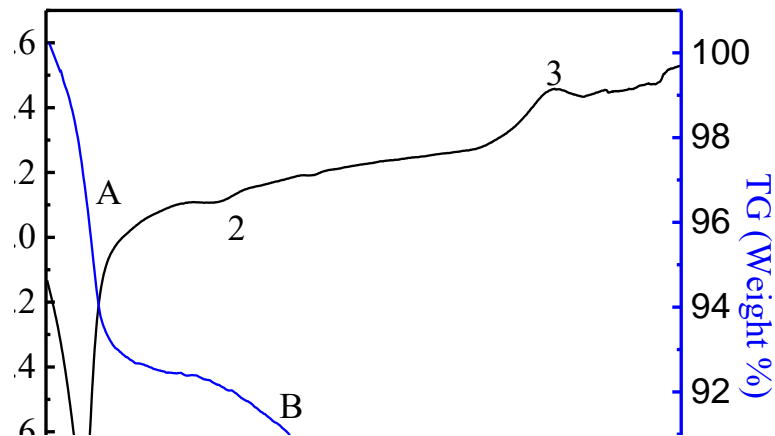


Fig. 5.11: DSC/TGA as a function of temperature of Fe_3O_4 NPs

The first weight loss which was about 7% occurred at around 25-100 °C due to removal of residual water. The second weight loss occurred at around 200 -350 °C due to removal of organic compounds which are acting as stabilizing agent of NPs and the weight loss is about 3%. The result of thermo gravimetric analysis demonstrated that most of the organic layer of the NPs was removed at high temperatures [8]. There was no significant weight change from 350-800 °C. In DSC curve two endothermic and one exothermic peak was observed. The first endothermic peak occurred at 100 °C due to the physical state change of water. The second endothermic peak occurred at 250 °C due to the physical state change of organic compound of the NPs. The exothermic peak observed at 650 °C due to the phase transition of the magnetite to hematite. The result of DSC demonstrated that the magnetite is unstable at high temperature and it gets transferred to hematite at high temperature.

5.8 Magnetization analysis

VSM was used to investigate the magnetic property of synthesized Fe_3O_4 NPs at room temperature. The obtained value of the saturation magnetization of the prepared NPs was about 70 emu/g, smaller than that of its bulk value (92 emu/g) [9]. The surface of the NPs is considered to be composed of some canted or disordered spins that prevent the core spins from aligning along the field direction resulting in decrease of the saturation magnetization of the small sized NPs [10]. The more the decrease in particle

size, the larger the surface spin canting, and consequently, a significant reduction in magnetization value is obtained [11]. From the curve (Fig. 5.12) it is apparent that there is no hysteresis loop, which indicates that both remanence and coercivity are zero, suggesting that the synthesized Fe_3O_4 NPs are superparamagnetic.



Fig. 5.12: Magnetization curve of Fe_3O_4 NPs as a function of applied field

5.8.1 Magnetization analysis for the variation of NaOH concentration

VSM was used to investigate the magnetic property of Fe_3O_4 NPs at room temperature synthesized using different concentrations of NaOH. The saturation magnetization obtained from the Fe_3O_4 NPs using different concentrations of NaOH as shown in Fig. 5.13. There is an increase in saturation magnetization with decrease in particle size. Thus, all of the synthesized Fe_3O_4 NPs are superparamagnetic in nature, so that there is no coercivity and remanence magnetization was observed. Fe_3O_4 is a ferrimagnetic iron oxide having cubic inverse spinel structure with oxygen anions forming an FCC closed packing and iron (cations) located at the interstitial tetrahedral sites and octahedral sites. The electron can hop between Fe^{2+} and Fe^{3+} ions in the octahedral sites at room temperature imparting half metallic property to magnetite. The magnetic moment of the unit cell comes only from Fe^{2+} ions with a magnetic moment of $4\mu_B$ [12]. The results suggest that, as the particle size decreases, there is a relative decrease in oxygen content

of the sample, which consequently, could lead to lowering of the valance state of the cations.

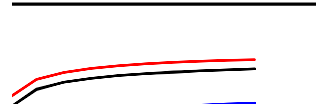


Fig. 5.13: Magnetization curve of Fe_3O_4 NPs synthesized using different concentrations of NaOH

The observed increase in unit cell volume with reduction in particle size of Fe_3O_4 NPs, perhaps implies an increase in Fe^{2+} content in the sample [ionic radius of Fe^{2+} (0.74 Å) is larger than that of Fe^{3+} (0.64 Å)]. Since the resultant magnetic moment in Fe_3O_4 is regarded to be due to the divalent ions (Fe^{2+}), the increase in magnetization with decrease in size could be justified. Though the sample is phase pure, the drop-in magnetization with further reduction in size may be attributed to surface effects [13]. The magnetization near the surface is generally lower than that in the interior. With increasing reduction in size, the surface effects become more predominant. In particles of the order of 4 nm, 50% of the atoms lie on the surface and, therefore, the effects are more prominent. Table 5.7 shows the value of saturation magnetization of Fe_3O_4 NPs for different NaOH. Fig. 5.14 shows the saturation magnetization as a function of NaOH concentrations.

Table 5.7: Saturation magnetization of Fe_3O_4 NPs synthesis with different concentration of NaOH

Concentration of NaOH (M)	Saturation magnetization M_s (emu/g)
1.00	50.1
0.50	55.3
0.10	67.7
0.05	70.5



Fig. 5.14: Saturation magnetization vs concentration of NaOH

5.8.2 Magnetization analysis for the variation of FeCl_3 and $\text{FeCl}_2 \cdot 4\text{H}_2\text{O}$ concentration

VSM was used to investigate the magnetic properties of Fe_3O_4 NPs at room temperature synthesized with different concentrations of FeCl_3 and $\text{FeCl}_2 \cdot 4\text{H}_2\text{O}$. The saturation magnetization values obtained by using the magnetometer (Table 5.5) show some interesting trends. Initially, there is an increase in saturation magnetization with decrease in particle size. However, there is a sudden drop in saturation magnetization

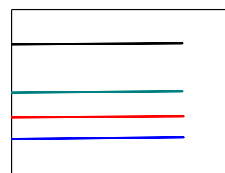


Fig. 5.15: Magnetization curve of Fe_3O_4 NPs as a function of applied field synthesized using different concentrations of FeCl_3 and $\text{FeCl}_2 \cdot 4\text{H}_2\text{O}$

value for the particles synthesis with lower concentration of FeCl_3 and $\text{FeCl}_2 \cdot 4\text{H}_2\text{O}$. Initial increase in magnetization value may be understood on the basis of crystal structure of Fe_3O_4 NPs which was analyzed from the XRD pattern of the particles shown in Fig. 5.15. From the XRD pattern it is clear that the particles synthesis with lower concentration contained some impurity phases, which is indicated the presence of hematite phase in the sample. The saturation magnetization (25.3 emu/g) of hematite (Fe_2O_3) is lower than, that of the saturation magnetization (70 emu/g) of Fe_3O_4 [14]. The presence of Fe_2O_3 phase in the particles synthesis with lower concentration of FeCl_3 and $\text{FeCl}_2 \cdot 4\text{H}_2\text{O}$ was caused to lower the saturation magnetization. Table 5.8 shows the saturation magnetization of Fe_3O_4 NPs synthesis with different concentrations of FeCl_3 and $\text{FeCl}_2 \cdot 4\text{H}_2\text{O}$. Fig. 5.16 shows the saturation magnetization as a function of FeCl_3 concentrations.

Table 5.8: Saturation magnetization of Fe_3O_4 NPs synthesis with different concentrations of FeCl_3 and $\text{FeCl}_2 \cdot 4\text{H}_2\text{O}$

Concentration of $\text{FeCl}_2 \cdot 4\text{H}_2\text{O}$ (M)	Concentration of FeCl_3 (M)	Saturation magnetization M_s (emu/g)
0.50	1.00	70.1
0.10	0.20	68.0
0.05	0.10	67.7
0.01	0.02	68.8
0.005	0.01	42.6

Fig. 5.16: Saturation magnetization vs concentration of FeCl_3

5.9 Particle size distribution measurement of Fe₃O₄ NPs

DLS is widely used as an effective technique for determining the average secondary particle size of Brownian NPs in colloidal suspensions [12]. In that method, the diffusion coefficients of NPs are first determined, and the average diameters of the particles are then calculated from these coefficients by using the Stokes–Einstein relationship [15].



Fig. 5.17: Size distribution of NPs for different concentrations of NaOH (a) 1.0 (b) 0.5 (c) 0.1 and (d) 0.05 M

The DLS apparatus used in this study has goniometer equipped with a 35 mW He-Ne laser of 632.8 nm wavelength. A multiple tau digital correlation scheme was used with a minimum sampling time of 0.1 μ s. The measurements were performed at a scattering angle of 90°. A quartz sample cell was set in a silicon oil bath such that the refractive indices of the oil and the cell were nearly equal. Light scattering was measured at a regulated temperature of 25.0 ± 0.1 °C. Fig. 5.17 showed the particles size distribution of the Fe₃O₄ NPs synthesized with different concentrations of NaOH. The average particles size (d) of the NPs synthesized with different concentrations of NaOH are

shown in table 5.9. The average particles size of NPs was decreasing with decreasing of NaOH concentration which is shown in Fig. 5.18. Fig. 5.19 showed the particles size distribution of the Fe_3O_4 NPs synthesized with different concentration of FeCl_3 and $\text{FeCl}_2 \cdot 4\text{H}_2\text{O}$. NPs synthesized with different concentrations of FeCl_3 and $\text{FeCl}_2 \cdot 4\text{H}_2\text{O}$ are shown in table 5.10. The average particle size of the NPs with different concentrations of FeCl_3 and $\text{FeCl}_2 \cdot 4\text{H}_2\text{O}$ are shown in Fig. 5.20, that is also supported the result of XRD and VSM.

Table 5.9: Average particle size of Fe_3O_4 NPs synthesized with different concentrations of NaOH

No.	Concentration of NaOH (M)	Average particle size d (nm)
(a)	1.00	22.9
(b)	0.50	19.4
(c)	0.10	18.0
(d)	0.05	17.0

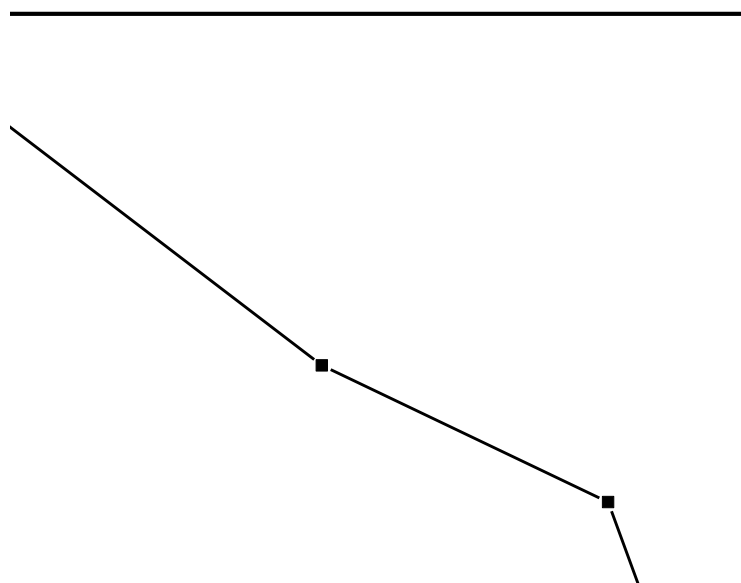


Fig. 5.18: Average particle size vs concentration of NaOH

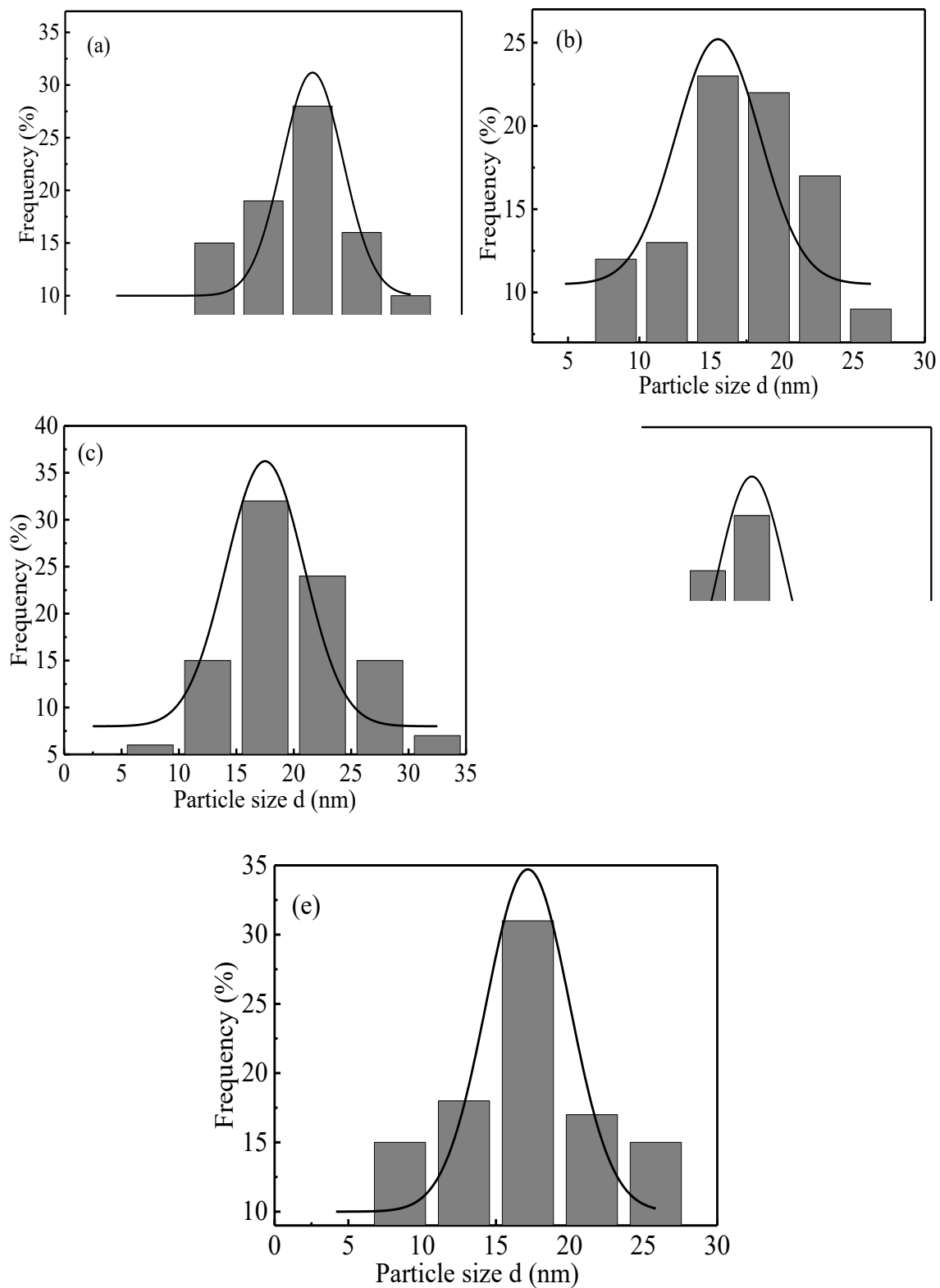
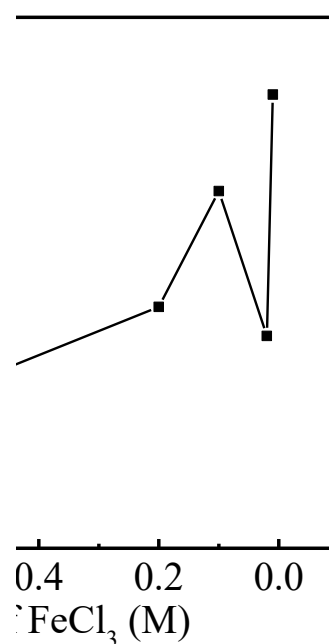


Fig. 5.19: Size distribution of Fe_3O_4 NPs synthesized with different concentrations of FeCl_3 and $\text{FeCl}_2 \cdot 4\text{H}_2\text{O}$. $\text{FeCl}_2 \cdot 4\text{H}_2\text{O}$ (a) 1.00 (b) 0.20 (c) 0.10 (d) 0.02 (e) 0.01 M

Table 5.10: Average particle size of Fe₃O₄ NPs synthesis with different concentrations of FeCl₃ and FeCl₂.4H₂O

No.	Concentration of FeCl ₂ .4H ₂ O (M)	Concentration of FeCl ₃ (M)	Average particle size d (nm)
(a)	0.50	1.00	15.5
(b)	0.10	0.20	17.5
(c)	0.05	0.10	18.7
(d)	0.01	0.02	17.2
(e)	0.005	0.01	19.7

Fig. 5.20: Average particle size vs concentration of FeCl₃

5.10 Correlation among crystallite size, average particle size and saturation magnetization of the NPs synthesized for different concentrations of NaOH

The correlation among crystallite size, average particle size and saturation magnetization for different concentrations of NaOH shown in Fig. 3.21.

All of these characterization support each other's, the crystallites size of the NPs decreased with the decreasing of concentration of NaOH, which is shown in Fig. 5.21 (a). It is well known that green synthesis is basically a chemical process. Here reducing

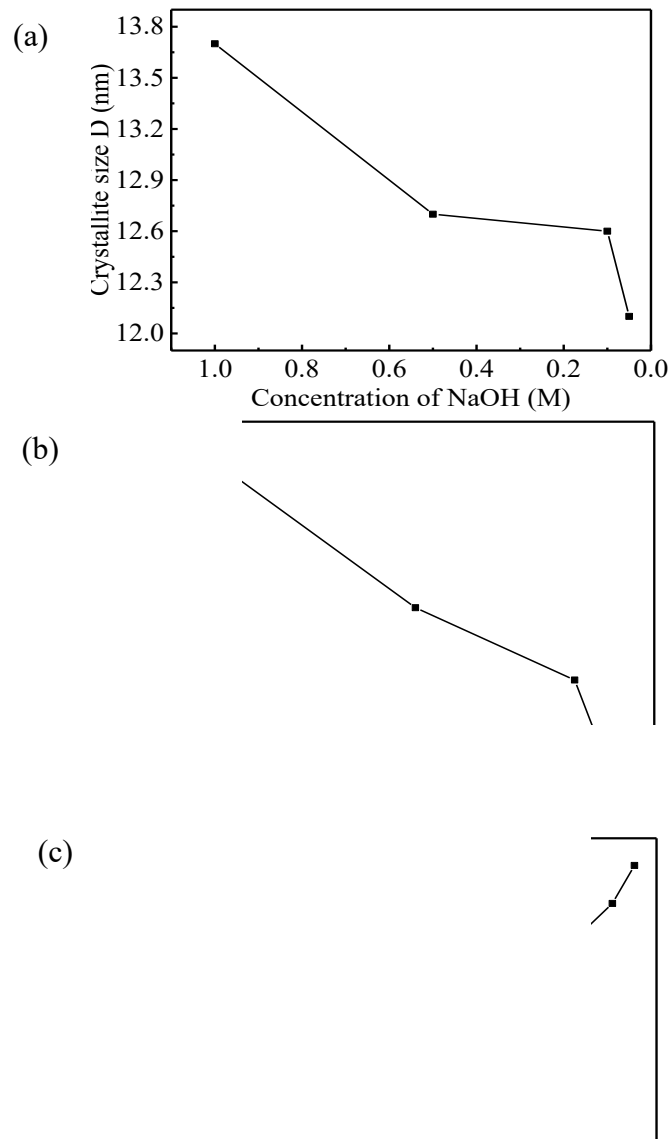


Fig. 5.21: NPs synthesized with different concentrations of NaOH (a) crystallite size vs concentration (b) particle size vs concentration and (c) saturation magnetization vs concentration

and precipitation are the main chemical reactions involved in the process, as the precipitation rate is get decreased with the decreasing of NaOH concentration so that the crystallites size also gets decreased. In case of particles size (Fig. 5.21 (b)) similar mechanisms occurred and the particles size get decreased with decreasing of NaOH concentrations, it can be said that the DLS result supports XRD analysis. It is known that saturation magnetization is increased with decreasing of particles size, by XRD and DLS analysis it was found that particles size gets decreased with decreasing of NaOH concentration. Fig. 5.21 (c) shows that saturation magnetization is increases

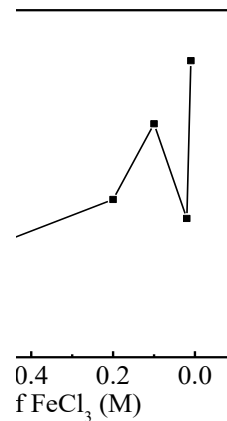
with increasing of NaOH concentration, hence it is clear that all of the characterization support each other's.

5.11 Correlation among crystallite size, average particle size and saturation magnetization of the NPs synthesized for different concentrations iron salt

NPs synthesized with different concentrations of FeCl_3 and $\text{FeCl}_2 \cdot 4\text{H}_2\text{O}$ also characterized with XRD to know its crystal phase and average crystallites size,

(a)

(b)



(c)

Fig. 5.22: NPs synthesized with different concentrations of FeCl_3 (a) crystallite size vs concentration (b) particle size vs concentration and (c) saturation magnetization vs concentration

investigated VSM measurements to know the saturation magnetization and performed DLS to determine the average particles size, Fig. 5.22 shows all these characterizations of the NPs. All of these characterizations also support each other's and get changed according to the mechanisms described in case of NPs synthesized with different concentration of NaOH. The crystallites size and the average particles size obtained from XRD and DLS, respectively showing the same trends as the particles size is increasing with the decreasing of concentrations. It is reported that the saturation magnetization is decreased with the increasing of particles size, the VSM analysis also support the result that the saturation magnetization is changing according to particles size. But the particles synthesis with lower concentration has shown reverse trend due to presence of maghemite phase. Which is observed at XRD pattern of the sample.

5.12 Antibacterial application of Fe₃O₄ NPs

The capacity of certain bacterial strains to develop resistance to antibiotics has aroused an increscent interest for the search of newer strategies to combat infections. Owing to this scenario, assessment of NPs for their antibacterial properties has evolved as an alternative to conventional antimicrobial agent. A simple and low-cost method to obtain Fe₃O₄ NPs stabilized by *Ipomoea aquatica* leaf extract has found to be a better solution over this problem. Antibacterial activity of *Ipomoea acuatica* leaf extract mediated green synthesized Fe₃O₄ NPs was studied against two human pathogenic bacteria using Agar well diffusion method and measurement of zone of inhibition are depicted in Fig. 5.23. gram-negative bacterium (*E. coli*) and gram-positive bacterium (*B. subtilis*) were

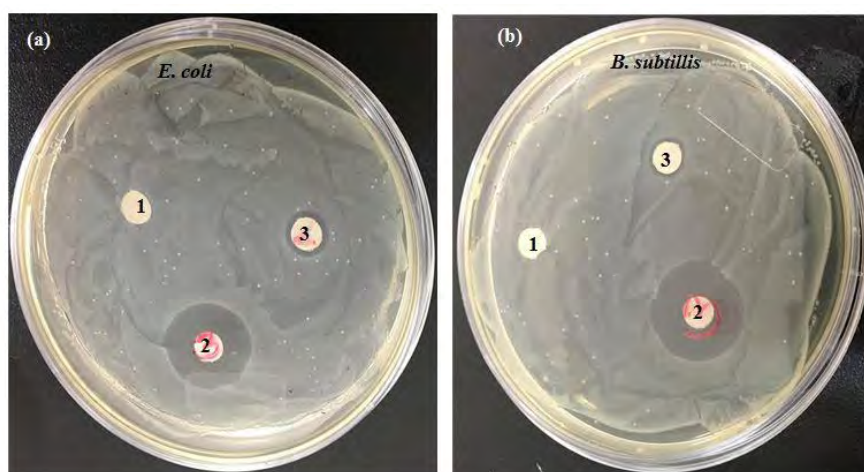


Fig. 5.23: Antibacterial activity of (1) DI water, (2) ampicillin and (3) Fe₃O₄ NPs against gram-negative *E. coli* (a) and gram-positive *B. subtilis* (b) pathogenic bacteria

taken in order to investigate their antibacterial activity against the pathogens. *E. coli* and *B. subtilis* were well known that cause food borne illness. In Fig. 5.23 there are three wells which were loaded with DI water, ampicillin and Fe_3O_4 NPs at the concentration of 100 mg/L which are denoted by 1, 2 and 3, respectively. The higher zone of inhibition 19 mm was observed against gram-negative bacteria *E. coli* and lower zone of inhibition 14 mm was observed against the gram-positive bacteria *B. subtilis*.

Several studies suggested two possible mechanisms involved in the interaction between NPs and bacteria: (1) the production of increased levels of reactive oxygen species (ROS), mostly hydroxyl radicals and singlet oxygen and (2) deposition of the NPs on the surface of bacteria or accumulation of NPs either in the cytoplasm or in the periplasmic region causing disruption of cellular function or disruption and disorganization of membranes. The mechanism of action is that the metal NPs are carrying the positive charges and the microbes are having the negative charges which create the electromagnetic attraction between the NPs and the microbes. When the attraction is made, the microbes get oxidized and die instantly. Generally, the NPs release ions, which react with the thiol groups ($-\text{SH}$) of the proteins present on the bacterial cell surface that leads to cell lysis. The central mechanism that caused the antibacterial activity by the NPs might be through oxidative stress caused by ROS. ROS includes radicals like superoxide radicals (O_2^-), hydroxyl radicals ($-\text{OH}$) and hydrogen peroxide (H_2O_2); and singlet oxygen ($^1\text{O}_2$) could be the reason damaging the proteins and DNA in the bacteria.

The antibacterial activity of Fe_3O_4 NPs was found due to the fact that the NPs were penetrating bacterial cells and act as a catalyst to inactive enzymes that microorganisms

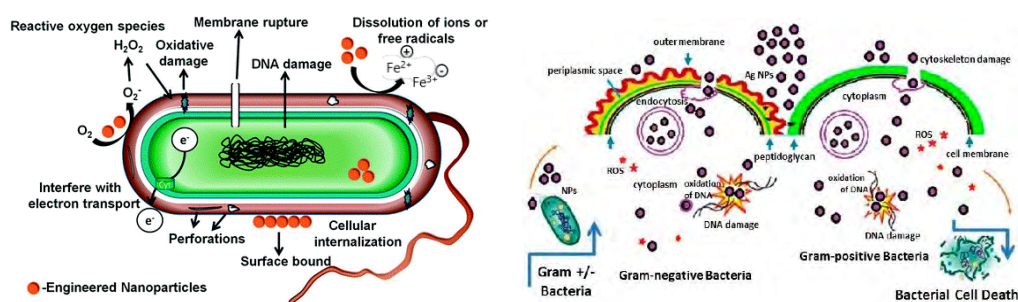


Fig. 5.24: Bacterial membrane rupturing mechanism of Fe_3O_4 NPs [19, 20]

need for their metabolism by interacting with thiol groups of proteins, disrupting bacterial membranes and also affecting DNA replication [16]. The graphical representation of bacterial membrane rupturing mechanism of Fe_3O_4 NPs shown in Fig. 5.24.

Different study suggested that the minimum critical size of NPs for rupturing bacterial membranes is 3.5 nm and maximum critical size is 22 nm [17]. The size of NPs synthesized with *Ipomoea aquatica* leaf extract was 15 nm which was found from TEM image analysis. As the size of NPs was smaller than maximum critical size and bigger than minimum critical size, so the NPs is able to ruptured the bacterial membrane. The Fe_3O_4 NPs are found to be more effective against gram-negative bacteria compared to gram-positive bacteria. This might be due to the cell wall of gram-positive bacteria composed of a rigid thicker multiple layer of peptidoglycan as it prevented the NPs from entering into cell wall [18]. Fig. 5.25 shows the cell wall of gram-positive and gram-negative bacteria.

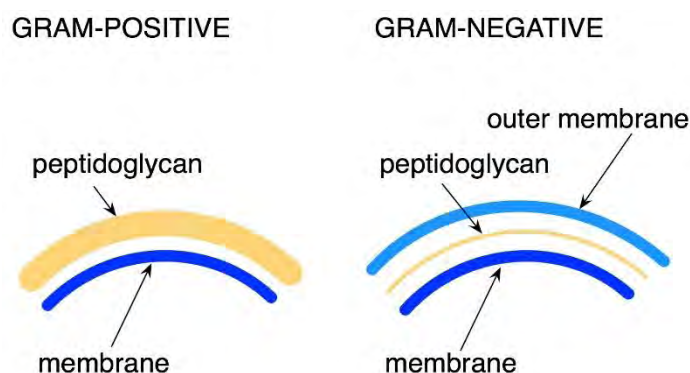


Fig. 5.25: Peptidoglycan (cell wall) of gram-positive and gram-negative bacteria [21].

References

- [1] Ausloos, P., Clifton, C. L., Lias, S. G., Mikaya, A. I., Stein, S. E., Tchekhovskoi, D. V., "The critical evaluation of a comprehensive mass spectral library," *J. Am. Soc. Mass Spectrom*, vol. 10, p. 287–299, 1998.
- [2] Marlene, C. M., Howard, F. M., Eloise, H. E., "Standard x-ray diffraction powder patterns," *J. Res. Natl. Bur. Stand.*, vol. 18, pp. 36-40, 1981.
- [3] Davor, B., "X-ray diffraction line broadening: modeling and applications to high-*T_c* superconductors," *J. Res. Natl. Inst. Stand. Technol.*, vol. 98, p. 321–353, 1993.
- [4] William, H. C., Martin J. C., Robert, A. G., "Crystal defects and the dissolution kinetics of rutile," *Geochim. Cosmochim. Acta*, vol. 52, pp. 1545-1556, 1988.
- [5] Nicolae, C. P., Davor, B., Sven, C. V., "Elastic macro strain and stress determination by powder diffraction: spherical harmonics analysis starting from the Voigt model," *J. Appl. Cryst.*, vol. 47, p. 154 –159, 2014.
- [6] Sole, V.A., Papillon, E., Cotte, M., Walter, P., Susini, J., "A multiplatform code for the analysis of energy-dispersive X-ray fluorescence spectra," *Spectrochim. Acta, Part B*, vol. 62, p. 63–68, 2007.
- [7] Di, Z., Amar B. K., Dan, R., David, P. Y., Andrew, W., David, C., Thomas, H. H., Zhanhu, G., "Electrospun polyacrylonitrile nanocomposite fibers reinforced with Fe₃O₄ nanoparticles: Fabrication and property analysis," *Polym. J.*, vol. 50, p. 4189–4198, 2009.
- [8] Payman, R., Allan, H., "A Fourier transform infrared (FTIR) and thermogravimetric analysis (TGA) study of oleate adsorbed on magnetite nanoparticle surface," *Appl. Surf. Sci.*, vol. 255, p. 5891–5895, 2009.
- [9] Caruntu, D., Gabriel, C., Charles, J. O., "Magnetic properties of variable-sized Fe₃O₄ nanoparticles synthesized from non-aqueous homogeneous solutions of polyols," *J. Phys. D: Appl. Phys.*, vol. 40, p. 5801–5809, 2007.
- [10] Bashar, I., Ihab, M. O., Borhan, A. A., Yousef, H. , "Magnetic nanoparticles: surface effects and properties related to biomedicine applications," *Int. J. Mol. Sci.*, vol. 14, pp. 266-305, 2013.

- [11] Parker, F. T., Foster, M. W., Margulies, D. T., Berkowitz, A. E., "Spin canting, surface magnetization, and finite-size effects in γ -Fe₂O₃ particles," *Phys. Rev. B*, vol. 47, pp. 7885-7891, 1993.
- [12] Jon, P. W., Paul, J. A., Paolo, G. R., "Charge ordered structure of magnetite Fe₃O₄ below the Verwey transition," *Phys. Rev. B*, vol. 66, pp. 1-15, 2002.
- [13] Ortega, D., Vélez, F. E., García, D. A., García, R., Litrán, R., Barrera, S. C., Ramírez-del-Solar, M., Domínguez, M., "Size and surface effects in the magnetic properties of maghemite and magnetite coated nanoparticles," *Phil. Trans. R. Soc.*, vol. 368, pp. 4407-4418, 1927.
- [14] Peter, D., "Relationship between median destructive field and remanent coercive forces for dispersed natural magnetite, titanomagnetite and hematite," *Geophys. J. R. astr. SOC.*, vol. 64, pp. 447-461, 1981.
- [15] Fanny, O., Anne, V., Pierre, G., "Determination of nanoparticle diffusion coefficients by Taylor dispersion analysis using a capillary electrophoresis instrument," *J. Chromatogr. A*, vol. 1204, p. 226-232, 2008.
- [16] Fred, C. T., "Mechanisms of antimicrobial resistance in bacteria," *Am J Infect Control.*, vol. 34, pp. 3-10, 2006.
- [17] Yuri, R., Maryna, O., Aravind, R. R., Jitendra, B., David, R. H., Sergiy, M., "Interaction of nanoparticles with lipid membrane," *Nano. Lett.*, vol. 8, pp. 941-944, 2008.
- [18] Murugan, V., Kyusik, Y., "Functionalization of biomolecules on nanoparticles: specialized for antibacterial applications," *Appl. Microbiol. Biotechnol.*, vol. 90, p. 1655-166, 2011.
- [19] Krishna, R. R., Ranjit, T. K., Adhar, C. M., "Size-dependent bacterial growth inhibition and mechanism of antibacterial activity of zinc oxide nanoparticles," *Langmuir*, vol. 27, p. 4020-4028, 2011.
- [20] Anil, K. S., Dale, A. P., Mitchel, J. D., "Relating nanomaterial properties and microbial toxicity," *Nanoscale*, vol. 12, pp. 1-28, 2012.
- [21] "<https://biology.stackexchange.com>".

CHAPTER 6

CONCLUSION

6.1 Conclusion

In this present study, the inverse spinel cubic crystalline structure of Fe₃O₄ NPs were successfully synthesized through leaf extract mediated green synthesis process using FeCl₂ and FeCl₃ as a precursor and *Ipomoea aquatica* leaf extract as a reducing, capping and stabilizing agents' provider. The attention focused on understanding the biological mechanisms and enzymatic processes of NPs biosynthesis as well as detection and characterization of biomolecules in evolved in the synthesis of Fe₃O₄ NPs. Many biomolecules in leaf extract such as proteins/enzymes, amino acids, polysaccharides, alkaloids, alcoholic compounds, and vitamins could be involved in bioreduction, formation and stabilization of Fe₃O₄ NPs. The reduction potential of ions and reducing capacity of leaf extract which depend on the presence of polyphenols, enzymes, and other chelating agents present in the leaf extract have critical effects on the amounts of NPs production. The elemental analysis of leaf extracts was performed by GC-MS analysis, which revealed more than 75 elements from *Ipomoea aquatica* leaf extract within the retention time range 5-75 min and the synthesized Fe₃O₄ NPs. From the XRD pattern the average crystallite size was estimated for the synthesized inverse spinel cubic crystalline typed Fe₃O₄ NPs as 12.8 ± 0.8 nm. NPs synthesized with various concentrations of NaOH and iron salts also confirmed their crystallinity by XRD analysis and it was found that all of them have pure crystal phase with invers spinel cubic crystalline structure, where the crystallites size of the NPs decreased with the decreasing of NaOH concentration and in case of iron salt concentrations decreased the size of the particles get increases. EDX spectra confirmed the presence of elemental components of the Fe₃O₄ NPs. FT-IR spectroscopy showed the involvement of biomolecules present in the extract of *Ipomoea aquatica*, which were verified in the synthesizing process of Fe₃O₄ NPs. The

formation of Fe₃O₄ NPs was confirmed due to the noticeable absorption peaks at 650 and 569 cm⁻¹. The FESEM image showed the high degree of crystallinity of the synthesized Fe₃O₄ NPs in which surface morphology was found to be homogeneous and almost spherical in shape with minimum agglomeration due to the presence of capping agents that stabilize the Fe₃O₄ NPs. The synthesized Fe₃O₄ NPs were well-dispersed and almost spherical in shape with particle size in the range of 15 to 20 nm as confirmed by TEM image also. The thermal analyses were carried out using DSC and TGA techniques in which the synthesized Fe₃O₄ NPs were responded with temperature. The magnetic properties of prepared Fe₃O₄ NPs are examined by VSM which demonstrates that the synthesized Fe₃O₄ NPs showed superparamagnetic characteristic with zero coercivity and remanent magnetization property. The NPs synthesized with various concentrations of NaOH and iron salts also showed superparamagnetic characteristic with zero coercivity and remanent magnetization. The saturation magnetization of the NPs increased with decreasing of particles size. The DLS investigation showed that the average particles size was decreased with decreasing the concentration of the precursors, which was also confirmed by the XRD analysis of the NPs.

The green synthesized Fe₃O₄ NPs were found to have the pronounced antibacterial activity against *E. coli* and *B. subtilis* that cause food borne illness. The one higher zone of inhibition was observed 19 mm against gram negative bacteria *E. coli* and lower zone of inhibition was observed 14 mm against gram positive bacteria *B. subtilis* respectively. The antibacterial activity of Fe₃O₄ NPs was found probably due to the fact that the NPs were penetrating bacterial cells and act as a catalyst to inactive enzymes that microorganisms need for their metabolism by interacting with thiol groups of proteins, disrupting bacterial membranes and also affecting DNA replication. From the antibacterial activity it is evidenced that *Ipomoea aquatica* mediated synthesized Fe₃O₄ NPs exhibited high antibacterial activity with both gram-negative and gram-positive bacteria.

6.2 Recommendations

The following scopes are recommended for future work-

- This study will help in synthesis of other metal oxide NPs by the said procedure in future.
- With the huge plant diversity much more plant species will be exploited in way to future era towards this non-toxic, easy, simple low cost and environmental friendly process.
- The possibility to increase the dispersibility of Fe_3O_4 NPs in the solvent should be explored and concentrated in future study which is highly beneficial for biomedical applications.

Conference Presentation

- 1) Plant Extract Mediate Synthesis of Magnetite (Fe_3O_4) Nanoparticles and Its Antibacterial Application. (Poster presentation) International Conference on Nanotechnology and Condensed Matter Physics, BUET, 11-12 January 2018
- 2) A Facile Synthesis of Magnetite Nanoparticles Using *Ipomoea aquatica* Aqueous Extract and Its Anti-Bacterial Activity. (Oral Presentation) International Conference on Physics - 2018, Dhaka, 08-10 March, 2018
- 3) Eco-friendly Green Synthesis of Magnetite (Fe_3O_4) Nanoparticles Using *Ipomoea aquatica* leaf extract and its Antibacterial Activity. (Oral Presentation) Conference on Weather Forecasting and Advances in Physics, KUET, 11-12 May 2018